Electrodes and Membranes for Alkaline Energy Storage and Conversion Devices

A Dissertation Presented for the
Doctor of Philosophy
Degree
The University of Tennessee, Knoxville

Asa Logan Roy
December 2018

Dedication

To my wife,
Hannah

And to my Parents,
Will and Daneen

Acknowledgements

I would first like to thank my advisor Dr. Thomas Zawodzinski. For providing me with the opportunity to work on such a wide range of projects, for providing the resources and guidance to complete this work, and for the ability to satisfy my intellectual curiosity, I owe him a great debt of gratitude. I would also like to give deep thanks to Dr. Gabriel Goenaga for training me in numerous experimental techniques, the opportunity to collaborate on various projects, and always being available to lend a helping hand, personally or professionally. I would like to thank my committee members, Dr. Jagjit Nanda, Dr. David Wood, and Dr. Dibyendu Mukherjee.

I must also thank the members of the Z group, past and present, for their help in completing this work. Whether this entailed training in new techniques, assistance with experiments, or discussions about research methods or data it has always been a friendly and helpful environment. There are several members of the Z group who I would like to thank in particular. I would like to thank Dr. Shane Foister for his willingness to collaborate on projects and share knowledge. I would like to thank Dr. Sam St. John for his help with various experimental techniques which proved instrumental in this work and his example as a driven researcher. And I would like to thank Dr. Alex Papandrew for his expertise, advice, and example.

Finally, I would like to thank my wife, Hannah, for her unwavering support and encouragement throughout my doctoral study. I would not be where I am today without the love and support from my family, my parents, Will and Daneen, my brother, Adam, and my sisters, Randi and Tessa.

Abstract

The high cost of platinum catalysts remains a major limitation to the development of proton exchange membrane fuel cells (PEMFCs). Despite a monumental research effort for platinum group metal free (PGM-free) catalysts, no viable alternative has been found that matches platinum in activity and stability. Further efforts to reduce cost have increased focus on anion exchange membrane fuel cells (AEMFCs) in recent years. Changing the conducting ion from protons in PEMs to hydroxide in AEMs changes the fuel cell environment from acidic to basic. Many PGM-free catalysts show increased activity and stability in basic environments.

Considering the promise of AEMFCs a series of systematic studies was conducted on several cell components. The physical and catalytic properties of a family of PGM-free oxygen reduction catalysts was studied through various spectrographic and voltammetric techniques. A thorough study of the catalyst performance in a single cell fuel cell test was conducted, leading to the development of a PGM-free catalyst which matched the performance of platinum. The anode performance was found to be significantly lower than expected. A systematic investigation of AEMFC anodes attributed the poor performance to electrode flooding. Modification of the anode catalyst layer led to improved anode performance to the detriment of the whole-cell performance. These results highlighted the need for a greater level of understanding of water transport in AEMs. To this end, several anion exchange membranes were synthesized and the effect of cation structure on water uptake, conductivity, stability was measured. Additionally, water uptake, conductivity, and the electro-osmotic drag of water were studied in a commercial AEM.

The knowledge of oxygen electrodes for AEMFCs was leveraged for the development of rechargeable zinc-air batteries (ZABs). ZABs utilize oxygen from the air as half the battery chemistry to dramatically reduce the size and weight of the cell. Rechargeable ZABs are expected to half energy densities 4-5x higher than lithium ion batteries. However, their development is hindered by zinc dendrite and passivation issues, poor oxygen catalysis, and electrolyte management. In this work, bifunctional oxygen reduction and evolution catalysts and novel anion exchange membrane are studied through ex-situ and in-situ methods.

Table of Contents

List of Tables

List of Figures

List of Abbreviations

AEM	Anion Exchange Membrane
AEMFC	Anion Exchange Membrane Fuel Cell
CV	Cyclic Voltammetry
EOD	Electro-Osmotic Drag
GC	Glassy Carbon
HOR	Hydrogen Oxidation Reaction
MEA	Membrane Electrode Assembly
NHE	Normal Hydrogen Electrode
OCV	Open Circuit Voltage
OER	Oxygen Evolution Reaction
ORR	Oxygen Reduction Reaction
PEM	Proton Exchange Membrane
PEMFC	Proton Exchange Membrane Fuel Cell
PGM	Platinum Group Metal
RDE	Rotating Disk Electrode
RHE	Reversible Hydrogen Electrode
RRDE	Rotating Ring Disk Electrode
ZAB	Zinc-air battery

Introduction

In recent years there has been an increased acceptance and focus on climate change stemming from human activities. As such there has been a monumental effort to shift away from fossil fuels for both transportation and electricity generation with new targets to reduce CO_2 emissions to 25% below 2005 levels within the next decade. This combined with a continuous demand for higher energy density batteries for portable electronics has increased focus on the next generation of energy storage and conversion technologies.

The goal of this work is to develop components for breakthrough new devices including zinc-air batteries and anion exchange membrane fuel cells. Both of these devices operate in an alkaline environment with atmospheric oxygen serving as the oxidant. Consequently, there are many similarities between these devices.

As part of this work, oxygen reduction catalysts, originally prepared for use in acidic environments, have been systematically studied in alkaline environments and successfully incorporated into anion exchange membrane fuel cells. The limitations of the anodes in these fuel cells have been widely observed in the literature. In this work, for the first time, the anode is diagnosed and studied though the use of a reference electrode in an operating fuel cell. A systematic approach is used to study the effect of anion exchange membrane cation structure on the water uptake, conductivity, and stability properties. And for the first time, the electro-osmotic transport of water in anion exchange membrane fuel cells has been studied in pure hydroxide and bicarbonate form, which will aid other researchers in the development of models of anion exchange membrane fuel cells.

A novel group of bifunctional oxygen catalysts for zinc-air batteries has been developed by leveraging work previous work on oxygen reduction catalysts. These catalysts were thoroughly studied ex-situ and tested in single cell experiments, but found to be subject to the same limitations as other non-biological oxygen evolution catalysts. In the interest of increasing battery efficiency, the work of a previous graduate student on a reversible 2 electron oxygen catalyst was continued scaled down to develop a nano-scale catalyst which was incorporated into a zinc-peroxide battery. Finally, knowledge gained from studying anion exchange membrane for fuel cell purposes was leveraged to develop separators for zinc-air batteries

Part 1: Catalysts and Electrodes for Alkaline Fuel Cells and Batteries

Introduction and Background

Electrochemical Reactions

Catalytic Reactions

Fuel cells and batteries operate by extracting the energy of exothermic reactions in a controlled manner. For example in hydrogen proton exchange membrane fuel cells, these electrode reactions are:

$$H_2 \leftrightharpoons 2H^+ + 2e^- \quad [1.1]$$

$$½O_2 + 2H^+ + 2e^- \leftrightharpoons H_2O \quad [1.2]$$

And the overall cell reaction is:

$$½O_2 + H_2 \leftrightharpoons H_2O \quad [1.3]$$

The maximum (theoretical) amount of energy which can be extracted from fuel cells can be calculated by the change in enthalpies of formation for the reactants and products. The enthalpy of formation of oxygen and hydrogen are zero since they are in their elemental form and the enthalpy of formation for water is -285.8 kJ/mol. From this the potential can be calculated from the equation:

$$E_H = \frac{\Delta H_f^\circ}{nF} \quad [1.4]$$

Where E_H is the theoretical reaction potential, $\Delta H_f°$ is the enthalpy change for the reaction, n is the number of electrons transferred (2 for the above reaction), and F is Faraday's constant. The overall reaction potential is therefore 1.48 V vs. RHE.

However, not all energy released from the above reaction can be captured as electrical work; the losses due to entropy must be accounted for. The electrical work which can be extracted from the cell is determined by from the change in the Gibbs free energy which is a measure of the change in enthalpy less the losses due to entropy as shown in Figure 0.1. The theoretical cell open circuit potential can be calculated using the equation:

$$E^\circ = \frac{\Delta G_f^\circ}{nF} \quad [1.5]$$

Where E° is the theoretical cell potential, $\Delta G_f°$ is the change in Gibbs free energy for the reaction, n and F are the same as equation 1. The Gibbs free energy of formation oxygen and hydrogen are zero and water is -237 kJ/mol. The theoretical cell potential is 1.23 V vs. RHE at standard conditions.

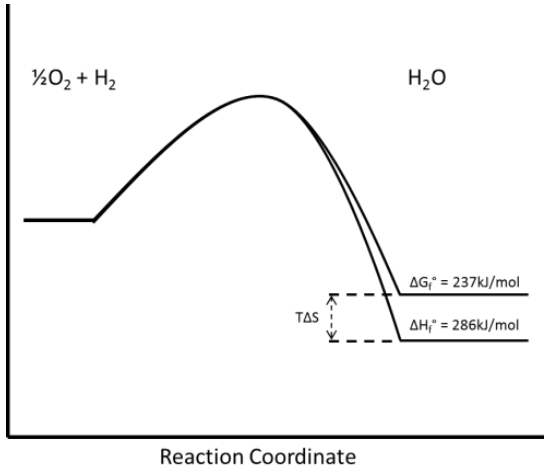

Figure 0.1: Free energy diagram for hydrogen fuel cell reactions

Enthalpy, entropy, and Gibbs free energy will vary with temperature. Enthalpy and entropy vary according to the heat capacity of the compounds; this effect is generally assumed to be small and is typically neglected. The Gibbs free energy changes according to the equation:

$$\Delta G_f^\circ = \Delta H_f^\circ - T\Delta S_f^\circ \quad [1.6]$$

Where $\Delta G_f°$ and $\Delta H_f°$ are as before, T is the temperature in kelvin and $\Delta S_f°$ is the change in entropy. There is therefore a linear decay in the cell potential with increasing temperature. At the operating temperature of 80°C the theoretical cell potential is 1.18 V.

The electrode reactions are not as simple as those represented above, especially for oxygen. In reality the reduction of oxygen and oxidation of hydrogen take place through complex multi-step mechanisms such as the one shown in Figure 0.2, or the one suggested by Wroblowa et al[4].

For example a proposed reaction mechanism for oxygen reduction on perovskite oxides is[5]:

$$O_2 + ° + e^- \rightarrow °O_2^- \quad [1.9]$$

$$°O_2^- + H_2O + e^- \rightarrow °OOH + OH^- \quad [1.10]$$

$$°OOH + e^- \rightarrow °O + OH^- \quad [1.11]$$

$$°O + H_2O + e^- \rightarrow °OH + OH^- \quad [1.12]$$

$$°OH + e^- \rightarrow ° + OH^- \quad [1.13]$$

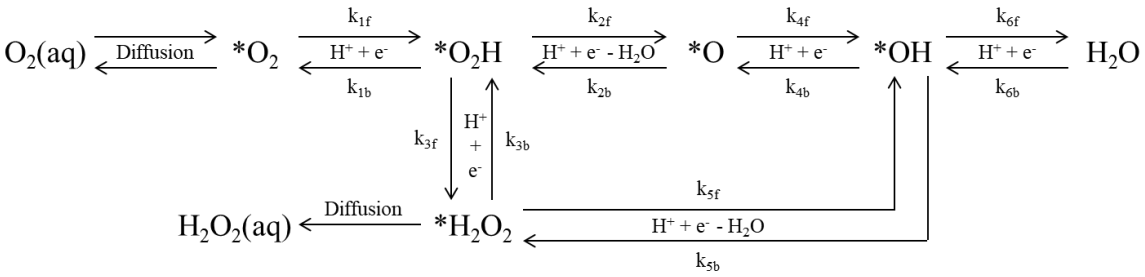

Figure 0.2: Representative Oxygen reduction scheme

For an ideal catalyst the Gibbs free energy difference between each reaction step would be equal as shown in the free energy diagram in Figure 0.3. Ideal catalysts would be expected to function close to the reversible potentials. Deviations in the adsorption energy of reactants and products lead to overpotentials.

Open Circuit Losses

In reality, a cell potential of determined from $\Delta G_f°$ will never be observed due to non-ideal experimental conditions and the effects of reactions that are not under pure thermodynamic control. The Nernst equation corrects the cell potential for operating temperature and reactant concentration.

$$E_n = E^\circ - 2.3\frac{RT}{nF}\log(Q_R) = E^\circ - 2.3\frac{RT}{nF}\log\left(\frac{P_{H_2O}}{P_{H_2}\cdot P_{O_2}^{0.5}}\right) \quad [1.7]$$

Where E_n is the Nernstian potential, E° is the theoretical cell potential, R is the universal gas constant, T is the temperature, Q_R is the reaction quotient, and P_{H2O}, P_{H2}, & P_{O2} are the partial pressures of water, hydrogen, and oxygen, respectively. The effect of non-standard conditions is typically minimal; for instance, for a fuel cell operating on H_2 and air, and with 100% RH at 80°C the Nernstian potential is 1.165 V. Cell conditions such as poor catalyst activity and hydrogen crossover have a much more pronounced effect on the observed open circuit voltages.

In full cells, hydrogen gas which crosses the membrane and reacts with oxygen at the cathode reduces the cell open circuit voltage (OCV) by bypassing the external circuit. This is referred to as an internal current. The current is related to the permeability of the electrolyte. Higher temperatures tend to lead to higher permeability and greater effects on the OCV. Zhang et al. calculated the change in OCV due to hydrogen crossover to be 24 mV for an MEA with Nafion 117 at 80°C.

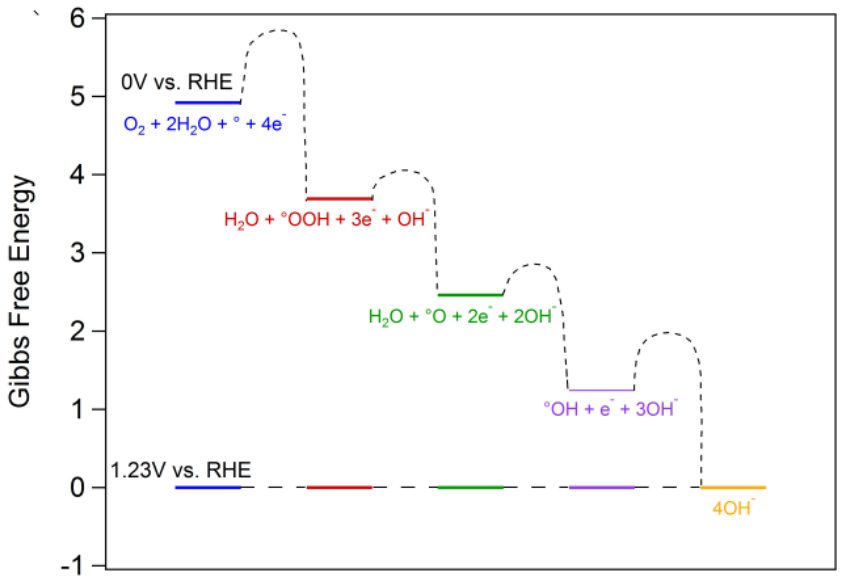

Figure 0.3: Representative free energy map for the oxygen reduction reaction on an ideal catalyst.

Inefficient catalysts are often the largest cause of low OCVs. Even with Pt, OCVs above 1.1 V are not commonly observed. Bockris and Huq[1], Watanabe and Devanathan[2], and Thacker and Hoare[3] were able to achieve the reversible potential on platinum electrodes through careful pretreatment of the solutions and electrodes. The low rest potential of platinum electrodes is likely due to a competing anode process such as the oxidation of platinum:

$$PtO + 2H^+ + 2e^- \leftrightharpoons Pt + H_2O \qquad \text{E=0.88 V vs. NHE} \qquad [1.8]$$

Platinum electrodes which have not been pretreated have been shown to have a PtO surface coverage of 30% above 0.8 V. The electrodes used to obtain the reversible potential were oxidized to form a passivating layer of PtO.

Closed Circuit Losses

The various fuel cell loses are shown in Figure 0.4. Activation losses are associated with the low current density region; they are characterized by a large initial decrease in cell potential with increasing current. In PEMFCs, the hydrogen oxidation reaction facile, so typically all activation losses are typically attributed to the poor kinetics of the oxygen reduction reaction. Better catalysts result in lower activation losses. The current in this region is described by the Butler-Volmer equation:

$$i = i_o * (e^{\frac{\alpha_a nF}{RT}\eta} - e^{\frac{-\alpha_c nF}{RT}\eta}) \qquad [1.14]$$

Where i_o is the exchange current density α_a and α_c are the anodic and cathodic charge transfer coefficients, and η is the overpotential. At high overpotentials where either the anodic or cathodic is negligible, the Butler-Volmer equation simplifies to the Tafel equation:

$$\eta = i_o + b * \ln(i) \qquad [1.15]$$

The Tafel equation provides important information about the kinetics of the electrode reactions. The constant b, referred to as the Tafel slope can indicate the reaction mechanism.

In the mid-high current region of the pol-curve the losses are associated the ionic conductivity of the electrolyte. This region of the polarization curve is characterized by a linear decay in potential with increasing current. The higher the conductivity of the electrolyte the lower the ohmic losses are.

At very high overpotentials the electrode kinetics become so fast that the cell is limited by the amount of fuel and/or oxygen that can be supplied to the electrodes. Higher flow rates, introduction of back-pressure, and advanced flow field designs are methods of reducing transport losses in fuel cells. In real-world applications the cells will not likely operate within this region.

The aim of electrocatalysts research is to develop stable materials which show greater activity towards the relevant reactions so that the kinetic losses in cells can be limited. The above discussion focused primarily on reactions relevant to hydrogen-air fuel cells, but can be more broadly applied to other electrochemical storage and conversion devices.

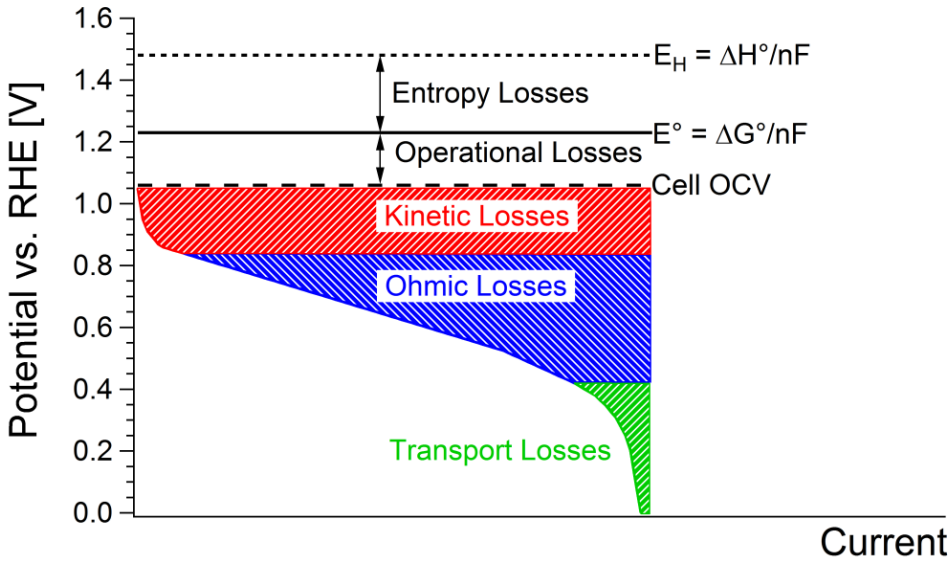

Figure 0.4: Representation of losses in fuel cells

Chapter 1: Platinum-Group Metal Free Oxygen Reduction Catalysts

Part of this work was previously published in the Journal of Power Sources:

A family of platinum group metal-free catalysts for oxygen reduction in alkaline media.
Gabriel A. Goenaga, Asa L. Roy, Nelly M. Cantillo, Shane Foister, Thomas A. Zawodzinski Jr.
Journal of Power Sources (2018), 395, 148-157
My contribution to this work involved; carrying out a significant portion of the RDE experiments and analysis of catalyst activity, oxygen reaction order, Tafel slope, number of electrons transferred from these experiments; collecting a portion of the XRD experiments and all analysis of results; and all of the single cell testing and analysis.

Introduction

Electrochemistry of Oxygen

The electrochemical reduction of oxygen or oxidation of water is a complex multi-step reaction which can proceed through multiple different pathways. The relevant reactions are listed in Table 1.1. Oxygen reduction can proceed through a 4 electron process to directly form water (or hydroxide under alkaline conditions), a 2x2 electron process to form hydrogen peroxide which is further reduced to water/hydroxide, or a 2 electron process to form hydrogen peroxide. In fuel cells there is a strong preference for the four electron pathway due to the potential for degradation the hydrogen peroxide may have on the membrane and electrode.

The exact reaction pathway is still unclear even well studied relatively simple single crystal catalysts. However a commonly proposed reaction on platinum catalysts in acidic conditions:

$$O_2 + ^\circ + e^- + H^+ \rightarrow {}^\circ HO_2 \quad [1.16]$$
$$^\circ HO_2 + H^+ + e^- \rightarrow {}^\circ O + H_2O \quad [1.17]$$
$$^\circ O + H^+ + e^- \rightarrow {}^\circ OH \quad [1.18]$$
$$^\circ OH + H^+ + e^- \rightarrow {}^\circ + H_2O \quad [1.19]$$

Where ° denotes an adsorbed species or free catalytic site. Using density functional theory, researchers have calculated the Gibbs free energies of the different steps at various electrode potentials[6,7].

Table 1.1: Oxygen electrochemical reactions in acidic and basic environments

Conditions	***Reaction***	***Number of Electrons***	***E Vs. RHE (V)***	***E vs. NHE (V)***
Acidic	$O_2 + 4\ H^+ + 4\ e^- \leftrightarrow\ 2\ H_2O$	*4*	*1.23*	*1.23*
	$O_2 + 2\ H^+ + 2\ e^- \leftrightarrow H_2O_2$	*2*	*0.68*	*0.68*
	$H_2O_2 + 2\ H^+ + 2\ e^-\ \leftrightarrow\ H_2O$	*2*	*1.77*	*1.77*
Basic	$O_2 + 4\ H^+ + 4\ e^-\ \leftrightarrow\ 2\ H_2O$	*4*	*1.23*	*0.401*
	$O_2 + H_2O + 2\ e^-\ \leftrightarrow\ HO_2^- + OH^-$	*2*	*0.76*	*-0.65*
	$HO_2^- + H_2O + 2\ e^-\ \leftrightarrow\ 3\ OH^-$	*2*	*1.7*	*0.88*

Rossmeisl et al. plotted this information as a reaction pathway map[6]. Figure 1.1a gives an example of this type of plot for oxygen reduction and evolution in an alkaline environment for idealized and realistic catalysts. When the electrode is held at the theoretical open circuit potential (1.23 V) step [1.16] is not spontaneous; therefore the electrode potential must be lowered to drive the reaction. In this example, oxygen reduction on would be predicted at potentials below 0.8 V where each step has a lower or equal Gibbs free energy to the preceding step. The study by Rossmeisl et al. did not deal with the oxides that are known to form on platinum surfaces which could account for the discrepancy between their theorized 0.78 V onset potential and the ~1.0 V observed in experiments. However, this study provides insight into the origins of the large overpotentials required for the oxygen reduction reaction on nearly all materials. The complex, multi-step nature of the reaction makes the search for a catalyst which shows optimum interaction with each of the intermediates extremely difficult.

A perfect catalyst would be flat across the entire free energy diagram and each step would have equal free energies, as described by Dau et al.[7]. In this case, any decrease in cell potential would force the reaction to proceed. In principal, the approach toward the development of more active catalysts would be to develop materials which interact with the intermediate adsorbed species to produce a reaction pathway as close to ideal as possible. However, it has been demonstrated that many materials have scaling factors for the different intermediates[8]. As can be seen in Figure 1.2, from the work of Stephens et al., the slope of the *OOH and the *OH intermediates are the same with a constant difference of ~3.2 eV, which is 0.8 eV higher than the theoretical optimum of 2.46 for an ideal catalyst[8]. Therefore, by tailoring a catalyst to improve the adsorption energy of one intermediate, it will negatively affect the adsorption energy of at least one of the other intermediates.

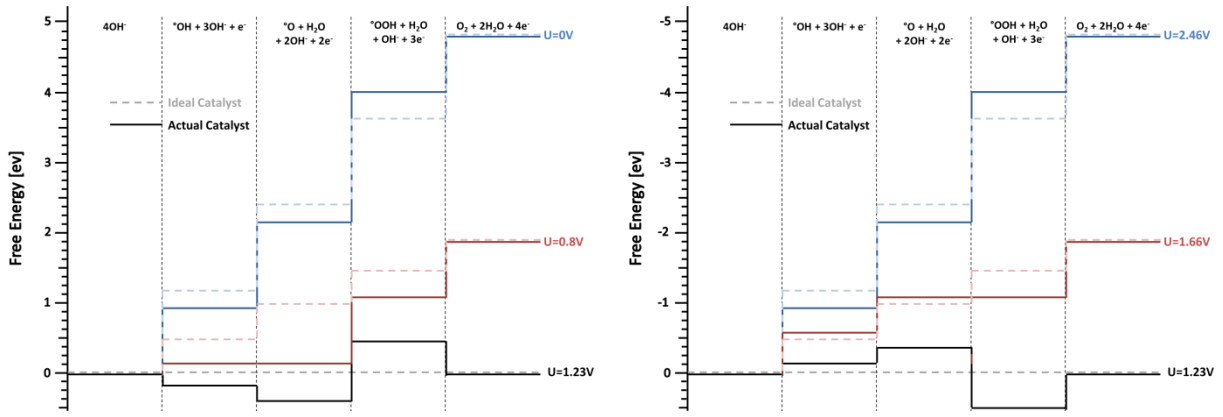

Figure 1.1: Representative Gibbs Free Energy diagrams for a) oxygen reduction and b) oxygen evolution on real and ideal catalysts.

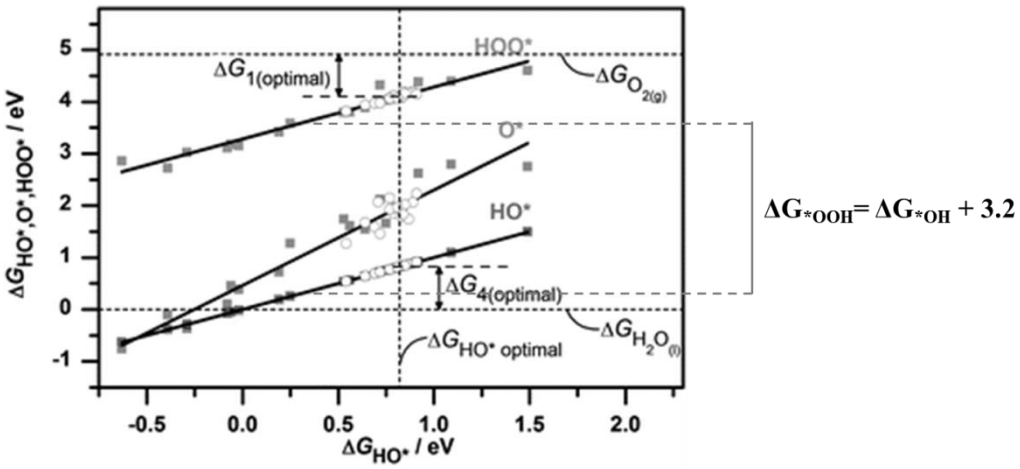

Figure 1.2: Scaling relationship between different ORR intermediates for Pt & Pt-alloy catalysts. Figure reproduced and modified from reference[8].

These relationships have been observed with both non-precious metals and precious metal catalysts for both oxygen reduction and water oxidation[8–10]. This suggests that there is a fundamental limit to the overpotential of at least 0.2 V for all standard catalysis. Natural systems are not limited by a scaling factor and are known to evolve and reduce oxygen very close to the theoretical potential, albeit in a mild environment. This is thought to be achieved by the coordination of transition metals in a 3-D structure that Man et al. suggest stabilizes one intermediate over the other and disrupts the scaling factor[10].

ORR on Precious Metals

Platinum is considered the benchmark catalyst for oxygen reduction in proton exchange membrane fuel cells. Decades of research have been conducted in the search for stable, active, low cost catalysts to replace platinum and dramatically reduce the cost of fuel cells. Materials such as metal oxides, organometallic complexes, doped carbon catalysts, and platinum alloyed with common transition metals. Despite this effort, there are relatively few materials which can match the stability and activity of platinum in the harshly acidic PEMFC environment.

An approach to reducing the cost of low temperature fuel cell systems which has garnered significant attention over the past 10 years has been to change the proton exchange membrane for a hydroxide exchange membrane to impart a basic environment within the cell. Many materials show better stability in basic environments due to the formation of passivating layers. Significantly, non-precious metal catalysts have been demonstrated to be more active in alkaline environments as well. Despite the higher activity in alkaline environments, no catalyst can compete with the activity of platinum on a mass-normalized basis. Therefore it is still used as a benchmark to compare the activity of other ORR catalysts.

In alkaline conditions, like acid, oxygen reduction on platinum proceeds mostly through a 4-electron process. There are two recognized Tafel slopes for oxygen reduction in both environments; at low overpotentials a slope of 60 mV/decade is observed and at high overpotentials a slope of 120 mV/decade is observed. The change in Tafel slope has attributed to the presence of surface oxide species. Only the 120 mV/decade slope is observed for platinum in concentrated phosphoric acid in which the potential of oxide formation is shifted to potentials above the relevant ORR window[11]. The surface oxide species causes a change in Tafel slope because the free energy, and therefore potential, is affected by the availability of reactive sites[12,13]. In the oxide-free potential region, ORR on platinum is characterized by a Tafel slope of

120mV/decade, oxygen reaction order of 1, and hydroxide reaction order of 0. This corresponds with a first electron transfer rate determining step such as:

$$* + O_2 \rightarrow * - O_2 \quad [1.20]$$
$$* O_2 + e^- + H_2O \rightarrow * OOH + OH^- \quad [1.21]$$
$$*OOH + e^- \rightarrow * O + OH^- \quad [1.22]$$
$$* O + e^- + H_2O \rightarrow * OH + OH^- \quad [1.23]$$
$$* OH + e^- \rightarrow * + OH^- \quad [1.24]$$

Where step 2 is rate limiting. This mechanism is consistent with experimental observations in the high current density region. Following the analysis of Holewinski and Linic, this mechanism also explains deviations in the reaction orders with respect to hydroxide and oxygen observed at low current densities[12–14].

The oxygen reduction activity of platinum and other transition metals has long been known to have a "volcano" relationship with regard to oxygen binding energy on the surface of the metal. Noble metals such as gold and silver, bind oxygen too weekly to facilitate the breaking of the oxygen double bond; the non-noble metals on the other hand bind oxygen too strongly, causing low turnover rates at the catalytic sites. Figure 1.3 shows this volcano-like relationship of catalytic activity verses oxygen binding energies as described by Norskov et al[15].

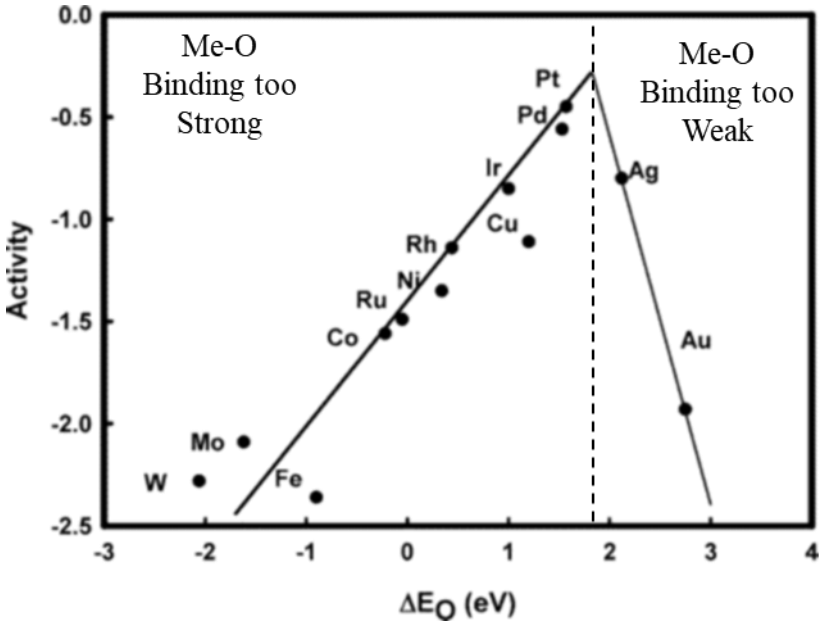

Figure 1.3: Volcano plot for oxygen reduction on metal electrodes. Reproduced and modified from reference[15].

Platinum is the most active ORR catalyst. Although silver is not as active as platinum it is considerably cheaper demonstrates sufficient stability in alkaline solutions[16]; it is therefore been commonly suggested as a potential ORR catalysts for AEMFCs. Damjanovic et al found similar relations between the Tafel slope, oxygen and hydroxide dependencies on silver and platinum[17]; differences were noted in the low current density region, presumably as a result of differences in the formation of oxides between the two metals.

In order to limit the cost of precious metal catalysts, a common approach is to alloy them with less expensive transition metals catalysts[18–20]. Nickel has been found to be the most active alloying metal for platinum[8]. Adzic and coworkers have shown the formation of core/shell structures introduce strain thereby modifying the surface electrical properties of platinum and dramatically increase the activity[21]. During testing in PEMFCs, the catalysts have been shown to de-ally with the non-precious metal dissolving into solution, leaving behind skeleton structures[18,20,22]. These materials may show promise in AEMFCs due to the improved stability of nickel in alkaline environments. Similarly silver alloys have been synthesized in an attempt to increase its activity[23–26]. Lima et al. found that alloying silver with cobalt increased the oxygen affinity and lead to higher catalytic activity[25].

ORR on Transition Metal Macrocycles

In the 1964 Jasinski reported the oxygen reduction activity of cobalt phthalocyanine[27]. Following this discovery, a significant research effort developed around the activity of various transition-metal-containing macrocycles, mainly phthalocyanines and porphyrins.

The activity of these materials is thought to arise due to their similarity to biological oxygen binding or reduction/evolution catalysts such as heme and chlorophyll. In biological systems ORR occurs through the 4 electron process at Co-facial di-metallic centers such as Cu/Fe system in heme[28]. Synthetic systems were developed based on co-facial cobalt macrocycles which were shown to reduce oxygen to water through the direct four electron process; however, changing the metal center and ligands was shown to result in the 2 electron process or parallel mechanisms involving both processes[28]. These materials were only active when adsorbed on edge plane of graphite; other substrates resulted in deactivation or a change to the 2 electron process. These materials were also only active within a narrow pH region and became deactivated outside of it. For these reasons these materials were not practical for use in fuel cell systems.

Macrocycles with Cr, Mn, Fe, Co, Ni, Cu, Ru, Pt, & Ir centers, among others, have been studied. The precious metals macrocycles are not practical for wide scale use due to issues with rarity and price. Among the first row transition metal centers several, Cr, Mn, Fe, & Co, have been reported to have reversible M(III)/M(II) and M(II)/M(I) redox couples[29]. Randin postulated the ORR on these macrocycles took place through a redox mechanism[30]; suggesting that a pre-catalysis surface reaction must occur before the metal center will catalyze the oxygen reduction reaction[29]:

$$Fe(III) \overset{\eta}{\rightarrow} Fe(II) \qquad [1.25]$$

For Cr, Mn, and Fe the onset potential has been reported to be close to this redox potential; however, for Co the potential of the M(III)/M(II) couple is well above the onset potential. Figure 1.4 shows that for both groups (Cr, Mn, Fe) and (Co) there is a linear correlation between the M(III)/M(II) redox couple potential for the specific macrocycle and the oxygen reduction activity[31]. In several papers the potential for the potentials of the Co(III)/Co(II) and Co(II)/Co(I) redox potentials are reported[29,32–34]. Interestingly, it seems that if the Co redox couple in Figure 1.4 were changed from Co(III)/Co(II) to Co(II)/Co(I), it lies close to or on top of the trend line established for Cr, Mn, and Fe, as indicated by the blue circles. This suggests that ORR involves the M(III)/M(II) couple for Cr, Mn, and Fe and the M(II)/M(I) couple for Co.

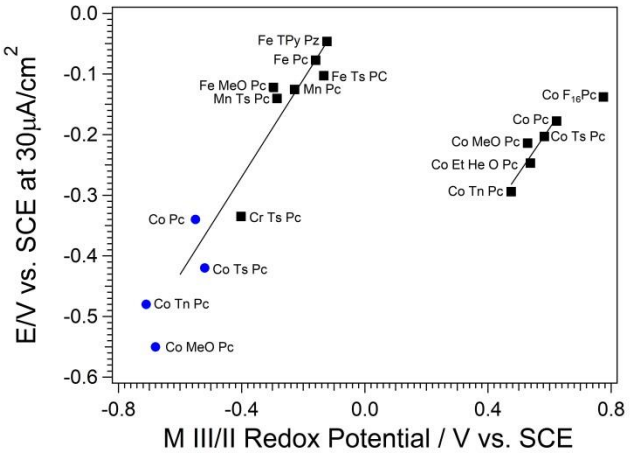

Figure 1.4: Plot of E at constant current (I=30 μA/cm^2) verses redox potential of the metal for oxygen reduction in 0.1 M NaOH on different metal macrocycles adsorbed on ordinary pyrolytic graphite. Reproduced and modified from references[29,34]

It has been observed that ORR proceeds through a 4 electron process for Mn and Fe, and though a 2 electron process for Co under alkaline conditions[28]. Wang et al, conducted DFT calculations for Fe and Co phthalocyanines and found that Co preferentially adsorbed oxygen in an end-on manner, while Fe adsorbed oxygen both end-on and side-on[35]. The side-on adsorption leads to increased oxygen-oxygen bond length compared to end-on adsorption and is more likely to result in the 4 electron process. Considering the molecular orbital interaction of oxygen with the transition metal may help to explain these observations[31].

Figure 1.5 shows a representative molecular orbital diagram for oxygen adsorbed in the side-on manner. It can be seen that for a metal center with six or more valance electrons, such as Co(III), the antibonding orbitals with oxygen will be filled, causing a bond order of zero. In contrast for lower valance metals Fe(III) and Mn(III) the bond order with oxygen is ½ and 1 respectively. Since the side-on adsorption is expected to be responsible for the four electron pathway, this offers an explanation as to why Mn and Fe proceed through 4 electrons processes while Co does not. The donation an electron to the oxygen molecule, shown as a dashed arrow in Figure 1.5, causes filling of the dioxygen anti-bonding orbitals which results in a less stable molecule. The higher number of valance electrons in Fe may be expected to increase back-bonding with oxygen lower its stability further than Mn and Cr would; this may explain the observed trend in increasing ORR activity from Cr to Mn to Fe[34].

End on adsorption of dioxygen involves an interaction between only one of the oxygen atoms. End on adsorption could be expected to occur with the metal center and oxygens lined up, direct end-on, or at some angle, kilter end-on. In either case, because of the relatively high strength of the O-O bond and since this adsorption mechanism involves the interaction of only one of the oxygen atoms, this mechanism is more likely to result in the 2 electron pathway. For the direct end-on adsorption of oxygen, shown in Figure 1.6, any more than three valance electrons will result in an overall bond order of zero; explaining why this was not observed in the simulations of Wang et al[35]. Instead oxygen end-on adsorption occurs at an angle as shown in Figure 1.7[35,36]. This system would be expected to be stable for less than 8 d electrons, both Fe(III) and Co(III). In this mechanism donation of an electron to oxygen would only be expected to occur with at least seven valence electrons; this would be the case for the Co(II)/Co(I) couple, but not for Fe(III)/Fe(II).

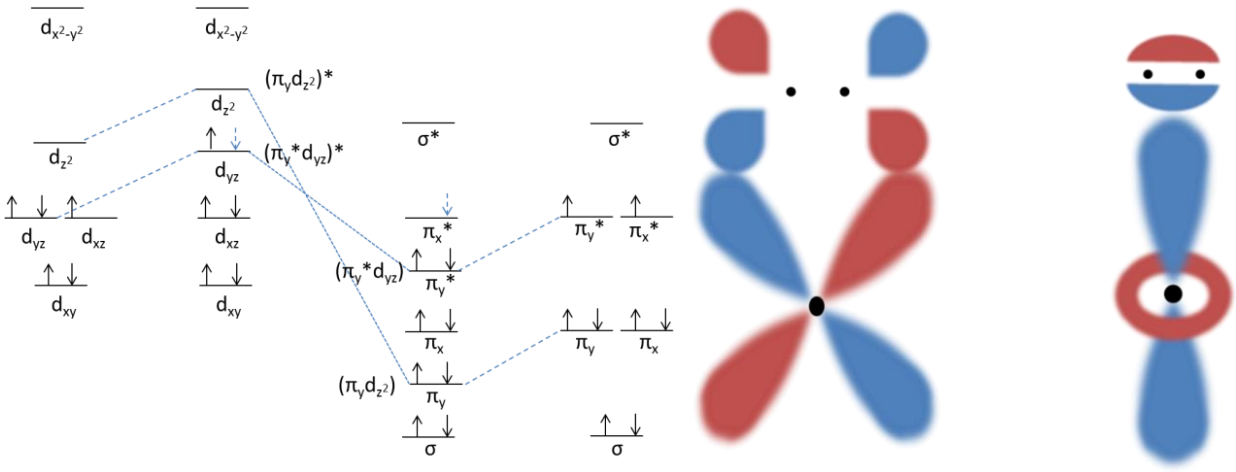

Figure 1.5: Side-on molecular orbital interactions between macrocycles and oxygen (shown for the Fe(III)/Fe(II) couple). A) Qualitative MO diagram B) M-d_{yz} & O_2-π* interaction C) M-D_{z2} & O_2-π interaction

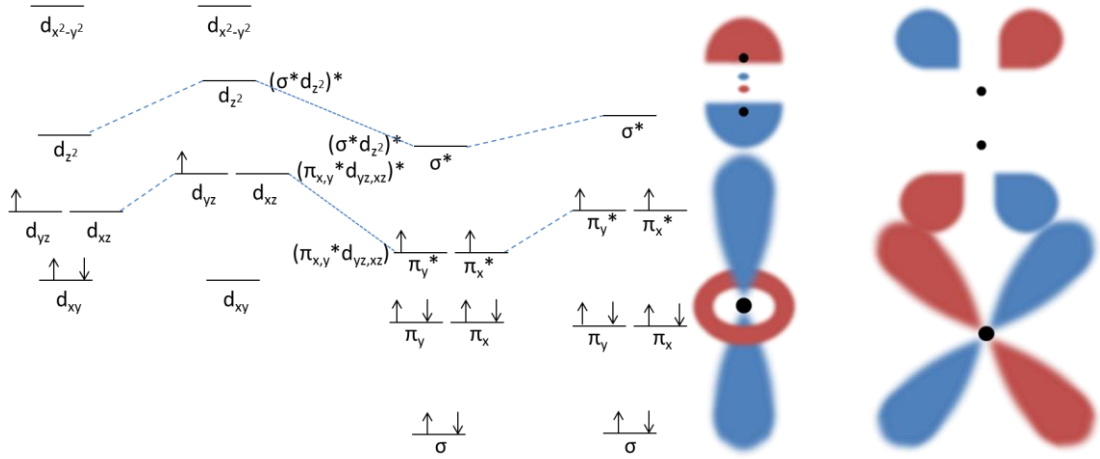

Figure 1.6: Direct edge-on molecular orbital interactions between macrocycles and oxygen. A) Qualitative MO diagram B) M-$D_{yz,xz}$ & O_2-π* interaction C) D_{z2} & O_2-σ* interaction

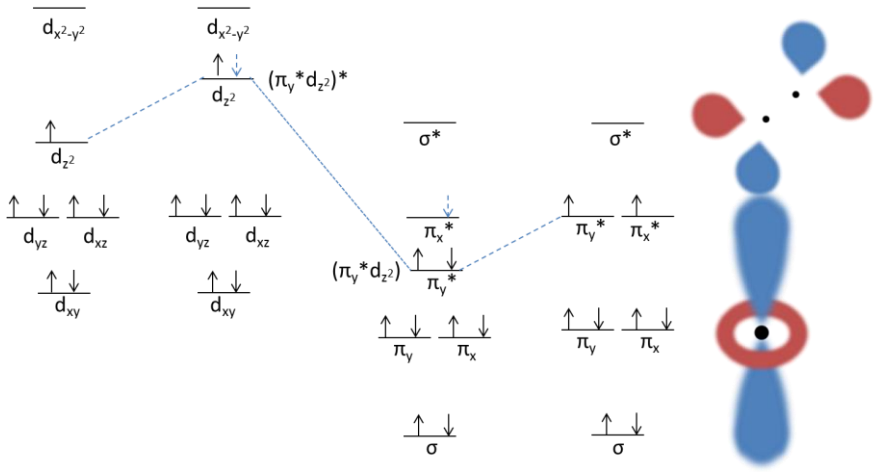

Figure 1.7: Kilter edge-on molecular orbital interactions between macrocycles and oxygen (Shown for the Co(II)/Co(I) couple). A) Qualitative MO diagram B) M-D_{z2} & O_2-π* interaction

The molecular orbital considerations help to explain the observed behavior of some macrocycle catalysts, for example the 4 electron reduction for Fe and Mn based catalysts and 2 electron pathways for Co, the increase in activity from Cr to Mn to Fe, and the correlation of catalysts activity with redox potentials.

Tafel slopes of ~30-40 mV/decade are observed in the low polarization regions on Fe and Mn macrocycles[29,36,37]; at larger overpotentials the Tafel slope changes to 120 mV/decade[29,34,36]. Zagal et al. suggested that since the low Tafel slopes are observed at potentials close to onset they are a reflection of the potential dependent generation of the M(II) catalytic site[29]. Yeager et al proposed the following mechanism for Fe and Mn[37]:

$$Fe(III) \overset{\eta}{\rightarrow} Fe(II)$$

$$Fe(II) + O_2 + e^- \rightarrow Fe(II)-O_2^- \quad [1.26]$$

$$Fe(II)-O_2^- + e^- + H_2O \rightarrow Fe(II) + OOH^- + OH^- \quad [1.27]$$

The four electron reduction on Fe and Mn macrocycles could be envisioned as:

$$Fe(II) + O_2 + e^- \rightarrow Fe(II)-O_2^- \quad [1.28]$$

$$Fe(II)-O_2^- + e^- + H_2O \rightarrow Fe(II) - OOH^- + OH^- \quad [1.29]$$

$$Fe(II) - OOH^- + e^- \rightarrow Fe(II) - O^- + OH^- \quad [1.30]$$

$$Fe(II) - O^- + H_2O \rightarrow Fe(II) - OH + OH^- \quad [1.31]$$

$$Fe(II) - OH + e^- \rightarrow Fe(II) + OH^- \quad [1.32]$$

Where the electrochemical adsorption of oxygen, step 1, is rate limiting in both cases. For Co catalysts the Tafel slope is reported to be close to 120 mV/decade through the entire region[29,34,36]. The two electron process on cobalt may be:

$$Co(II) \overset{\eta}{\rightarrow} Co(I)$$

$$Co(I) + O_2 + e^- \rightarrow Co(I){-}O_2^- \quad [1.33]$$

$$Co(I){-}O_2^- + e^- + H_2O \rightarrow Co(I) + OOH^- + OH^- \quad [1.34]$$

Here, the first step will be rate limiting to correspond with a Tafel slope of 120 mV/decade.

ORR on Heat Treated Transition Metal Macrocycles

One of the largest issues with transition metal macrocycles is poor stability in concentrated acids and bases. Heat treatment of transition metal macrocycles adsorbed on carbon materials was found to increase the stability and performance decades ago[38]. The reason for the increased performance is not well understood; additionally, the nature of the active site in the pyrolyzed catalysts is a matter of great contention. The macrocycles are known to fully or partially decay depending on pyrolyzation time and temperatures. In the 1980s it was discovered that the pyrolyzation of carbon, transition metal, and nitrogen precursors together result in very similar catalysts[39]. There are various moieties on these pyrolyzed catalysts which could contribute to the catalytic activity including metals (carbides, oxides, and nitrides), CNx groups, and Me-Nx/C groups[40–44]. Metallic sites such as pure metal, oxides, nitrides, and carbides are likely not very active; it has been shown that acid treatments to remove excess metal typically result in increased performance[45,46], which may be attributed to the removal of the mass of the non-participating particles. Much of the contention with these types of catalysts is the function of the metal atoms. Some researchers believe the metal is the catalyst center, while others argue that the function of the metal is to aid in the creation of the active sites.

Wiesener, Popov, and Ozkan view the role of the metal during pyrolyzation is to catalyze the creation of CNx sites resulting in higher site density than in nitrogen doped carbons formed in the absence of metals[38]. In their view, the metal does not participate in the oxygen reduction reaction. These researches point to the high activity of CNx style catalysts as evidence of this theory. Other researchers believe that the transition metal is coordinated with several CNx sites to form active sites that are similar to macrocycles.

There is now strong evidence to support the theory that the active sites are M-Nx/C sites which are similar to macrocycles. Firstly, Mossbauer spectroscopy, XANES, and XPS

measurements have confirmed the presence of M-Nx/C groups[40–45]. The onset potential for pyrolyzed catalysts have been reported to be in the range of observed metal redox peaks[42,44,46,47]; as with the pristine catalysts this indicates that the metal center participates in the reaction. Selective poisoning experiments on several pyrolyzed Fe-based catalysts also provide support for this perspective. Yeager and coworkers showed that oxygen reduction on both Fe and Co based macrocycles was inhibited by the addition of cyanide anions[48]. Recently, several authors have reported similar dramatic reductions in ORR activity for pyrolyzed Fe catalysts after the addition of KCN[40,42,44].

Given these results it seems that macrocycles are restructured during pyrolysis to form new M-Nx/C sites on or between graphene sheets. These sites are primarily responsible for the oxygen reduction activity. The onset potential is tied to the redox potential of the metal center. The increase in ORR activity is likely achieved through an increase in the potential of the metal redox couple[46].

Typically Tafel slopes between 60-70 mV/decade are reported for pyrolyzed M-Nx/C catalysts in alkaline environments[49–51]. This is typically attributed to an electrochemical step following the first electron transfer. However, if the dioxygen molecule adsorbs on the electrode before the first electron transfer as suggested by Chlistunoff[47] than the second electron transfer would be responsible for a slope close to 60. The second electron transfer could involve the cleavage of the O-O bond as suggested by Dodelet and Jaouen[52] and Chlistunoff[47]. Due to the strength of the O-O bond, one may expect that its breaking would be rate limiting. A conceivable mechanism for this reaction may be:

$$Fe(II) + O_2 \rightarrow Fe(II) - O_2 \quad [1.35]$$

$$Fe(II) - O_2 + e^- \rightarrow Fe(II) - OO^- \quad [1.36]$$

$$Fe(II) - OO^- + H_2O \rightarrow Fe(II) - OOH + OH^- \quad [1.37]$$

$$Fe(II) - OOH + e^- \rightarrow Fe(II) - O + OH^- \quad [1.38]$$

$$Fe(II) - O + e^- + H_2O \rightarrow Fe(II) - OH \quad [1.39]$$

$$Fe(II) - OH + e^- \rightarrow Fe(II) + OH^- \quad [1.40]$$

Because the oxygen adsorbs before the first electron transfer, it only experiences a fraction of the potential drop, η, across the Helmholtz layer. Therefore for a second electron transfer rate limiting reaction the Tafel slope would be expected to be given by the equation:

$$b = \left(\frac{RT}{\alpha F}\right) \; where \; \alpha = \left(\frac{\eta n}{\nu} + r\beta\right) \quad [1.41]$$

The number of electrons transferred before, n, and during, r, the rate determining step would be one. With a stoichiometric number of 1, a symmetry factor and fractional potential drop of roughly ½, the apparent transfer coefficient, α, should be close to 1 giving Tafel slopes close to 60 mV/decade.

In this work, a variety of heat treated metal macrocycle catalysts were synthesized, characterized, and tested for use in AEMFCs.

Experimental

Synthesis

Heat treated metal macrocycle catalysts were prepared by collaborating researchers. The metals used for this work were Ag, Co, Cu, Fe, Ni, and their bi-metallic combinations, outlined in Table 1.2. A catalyst containing no metal was also synthesized as a control.

The catalysts were prepared in a 2-step method. In the first step, 1,2-benzenedinitrile was covalently anchored to the carbon support Black Pearls 2000 (BP2000) from Cabot Corp using diazonium-coupling chemistry. In the second step, the dried modified carbon was suspended in water and aqueous solutions of 3,5-diaminotriazole and metal acetates were added, resulting in the Metal-TriazoloPthalocyanine (TrPc) materials.

The as-synthesized samples were heat treated at temperatures ranging from 600°C to 1000°C under inert atmosphere to afford the Me-TrPc catalysts, as described elsewhere[53]. Several methods of removing the metal formed during pyrolysis were investigated. After the initial pyrolysis, catalysts were subjected to treatments in diluted solutions of sulfuric acid (H_2SO_4) or ethylenediaminetetracetic acid (EDTA) at 80°C overnight. Catalysts were rinsed several times with DI water until neutral pH was reached and dried in a convection oven at 85 °C. This procedure is followed by a second heat treatment at the initial pyrolysis temperature.

Table 1.2: Catalysts prepared and tested in this work. Mono-metallic catalysts are shown in blue and bi-metallic catalysts are shown in red.

M	**Ag**	**Co**	**Cu**	**Fe**	**Ni**
Ag	Ag	Ag/Co	Ag/Cu	Ag/Fe	Ag/Ni
Co		Co	Co/Cu	Co/Fe	Co/Ni
Cu			Cu	Cu/Fe	Cu/Ni
Fe				Fe	Fe/Ni
Ni					Ni

Rotating Ring Disk Electrode Experiments

Some RDE experiments were conducted by a collaborating researcher.

Rotating ring disk electrode experiments were carried out using a multi-channel VMP3 potentiostat from Bio-Logic, a Pine instruments MSR rotator and rotating ring disk electrode (RRDE) with a 0.2472cm^2 glassy carbon disk and Pt ring (320 μm ring-disk gap, 6.25 mm and 7.92 mm ring inner and outer diameter, respectively). The RRDE collection efficiency *N* was measured experimentally and determined to be 38%. A gold counter electrode mounted in a glass tube with a frit at one end was used. A Radiometer Analytical XR400 Hg/HgO reference electrode with 1M KOH fill solution was used.

The potential of the reference electrode versus the reversible hydrogen electrode (RHE) was determined by saturating 0.1 M KOH with hydrogen and measuring the OCV with a multi-crystalline Pt working electrode. Ultra-high purity gasses from Airgas Co. were used for each experiment.

Inks were prepared using a 30 wt% Nafion® to 70 wt% catalyst ratio and methanol as solvent. Aliquots of the inks were solution-casted onto the GC disk electrode to reach loadings of 200, 400, or 600 μg/cm^2 for NPMCs or 25 $\mu g_{Pt}/cm^2$ for Pt/C. Catalysts were tested in aqueous 0.1 M KOH electrolyte. For each experiment, the electrolyte was de-aerated for at least 30 min with nitrogen; voltammograms were collected between 1.1 and 0.1 V vs. RHE with a 10 mV/s scan rate with the electrode static and rotating at 1600 rpm for background correction. This procedure was repeated in O_2-saturated electrolyte, using 625, 900, 1225, 1600 and 2500 rpm rotation speeds. RRDE onset potentials were defined as the potential (vs. RHE) at which the ORR current density reaches a value of 50 μA/cm^2. The ring electrode was held at 1.3 V vs. RHE to scavenge any peroxide generated at the disk electrode.

Oxygen reduction reaction activity in different partial pressures of oxygen (P_{O_2}) was studied to determine the reaction order with respect to oxygen. Following a previously reported procedure,[54] oxygen and nitrogen gas were mixed using two Cole-Parmer multi gas MC series mass flow controllers to obtain P_{O_2} of 10, 20, 30, 40, 60, 80 and 100% (with the remainder nitrogen). The voltammograms were collected at 1600rpm.

Rotating ring disk electrode stability experiments were carried out by measuring ORR activity of the catalyst before and after cycling the catalyst in the kinetic region at 50 mV/s, 5000 times. The ORR activity was measured in the same manner described above. Cycling was

conducted in electrolyte saturated with a mixture for 80% nitrogen and 20% oxygen (air composition).

Anion Exchange Membrane Fuel Cell Electrode Preparation

Electrodes were prepared by a collaborating researcher.

The AEMFC tests were conducted using Tokuyama's A201 membrane and AS4 ionomer. NPMCs inks were prepared by combining catalyst powders (70%) with AS4 ionomer (30%) and diluting 0.1 wt% with IPA. Platinum inks were prepared by mixing Tanaka 30% Pt/C with AS4 ionomer to achieve an equal Pt to AS4 weight ratio and diluting to 0.1 wt% with IPA. The catalyst inks were sonicated for at least 30min prior to spraying. The catalyst layers were spray painted onto Sigracet 25BC gas diffusion layers to achieve the desired loading (0.4 mg_{Pt}/cm^2 or 1, 2 or 3 mg_{NPMC}/cm^2).

Membrane Electrode Assembly

Membrane Electrode Assemblies were prepared by either hot-pressing the electrodes to a carbonate-form membrane or stacking the electrodes with a hydroxide form membrane in the cell. The carbonate-form membrane was prepared by ion exchanging as received A201 in 0.5 M Na_2CO_3 for 2 hr at 80°C and repeating twice, then removing excess ions by soaking in DI H_2O for 2hr at 80°C and repeating twice. Hot-pressing was carried out at 120°C for 10min under 1000 kg. Hydroxide form A201 was prepared by soaking in 1M KOH overnight, then removing excess KOH by thoroughly rinsing with DI H_2O, and allowing it to soak for at least 4 hr.

Anion Exchange Membrane Fuel Cell Testing

The MEAs were placed in a 5 cm^2 Fuel Cell Technologies cell hardware with serpentine flow channels. A palladium (Pd) coated Cu wire was included as a pseudo-reference electrode. The cell temperature, relative humidity (RH) and gas flow rates were controlled with a Fuel Cell Technologies test station. The cells were tested at 60°C with 200 ml/min of 100% RH hydrogen and oxygen gas flows and ambient pressure. Unless otherwise specified, 1 mg_{NPMC}/cm^2 and 0.4 mg_{Pt}/cm^2 were used as standard loadings for non-precious and precious metal catalysts, respectively.

X-ray Powder Diffraction

X-ray diffraction patterns were recorded with a Bruker Phaser D2 diffractometer using Ni-filtered Cu Kα radiation (λ = 0.154184 nm, 30 kV, 10 mA, 0.02 deg/step, 0.5 s/step) in the Bragg-Brentano geometry fitted with a 0.6 mm antiscatter slit in the incident beam and a 2.5 deg. Soller slit in the diffracted beam.

Results and Discussion

X-ray Diffraction

X-ray diffraction was conducted on the catalysts before and after pyrolysis. Before pyrolysis XRD peaks in the Cu, Ni, and Fe spectra attributed to the metal phthalocyanine were observed. These peaks disappeared during pyrolysis, indicating the destruction of the phthalocyanines structure during this step. This is demonstrated in Figure 1.8a by the disappearance of the peak at ~28 and ~25 for the Ni TrPc and Fe TrPc catalysts respectively. Also apparent from Figure 1.8a is the presence of metallic particles in the Ag TrPc and Fe TrPc samples. These peaks were observed in each catalyst containing the respective metal. The structure of the particles was determined to be a mix of silver and silver oxide for the Ag TrPc and iron (III) oxide for the Fe TrPc. Metal or metal oxide peaks were detected for each catalyst after heat treatment as can be seen in Figure 1.8b-l.

For most of the bi-metallic catalysts the XRD patterns were indicative of non-alloyed combinations of both metals. However, for the CoFe TrPc 700°C catlayst new peaks were obsereved associated with a CoFe metal alloy and for CoNi TrPc 700°C and FeNi TrPc 700°C slight shifts in peak locations were observed which were indicative of metal alloying.

Oxygen Reduction Activity

The activity of each catalyst was measured as prepared and for each pyrolyzation temperature. The as-synthesized samples generally had decent ORR activity in alkaline solution, but the catalytic activity is greatly enhanced after pyrolysis. Figure 1.9a shows the effect of pyrolyzation on the Ni TrPc catalyst. The performance of this catalyst as prepared is poor, but the activity increases after pyrolyzation at 700°C and is further improved at even higher temperatures. The pyrolysis temperature at which the peak ORR activity occurs varies with the metal in the catalyst. Generally, the more easily oxidized metals required lower pyrolysis temperatures.

Figure 1.9a shows the ORR performance of the pyrolyzed single metal catalysts compared to platinum and the catalyst containing no metal. All of the catalysts have a higher activity than the modified carbon; although the onset of the nickel catalyst was similar. The copper and cobalt are the only single metal catalysts which outperform platinum.

The ORR performances for the bi-metallic catalysts are shown in Figure 1.9c-l. The onset potentials, half-wave potentials ($E_{½}$), and limiting current densities derived from Figure 1.9 are given in Table 1.3.

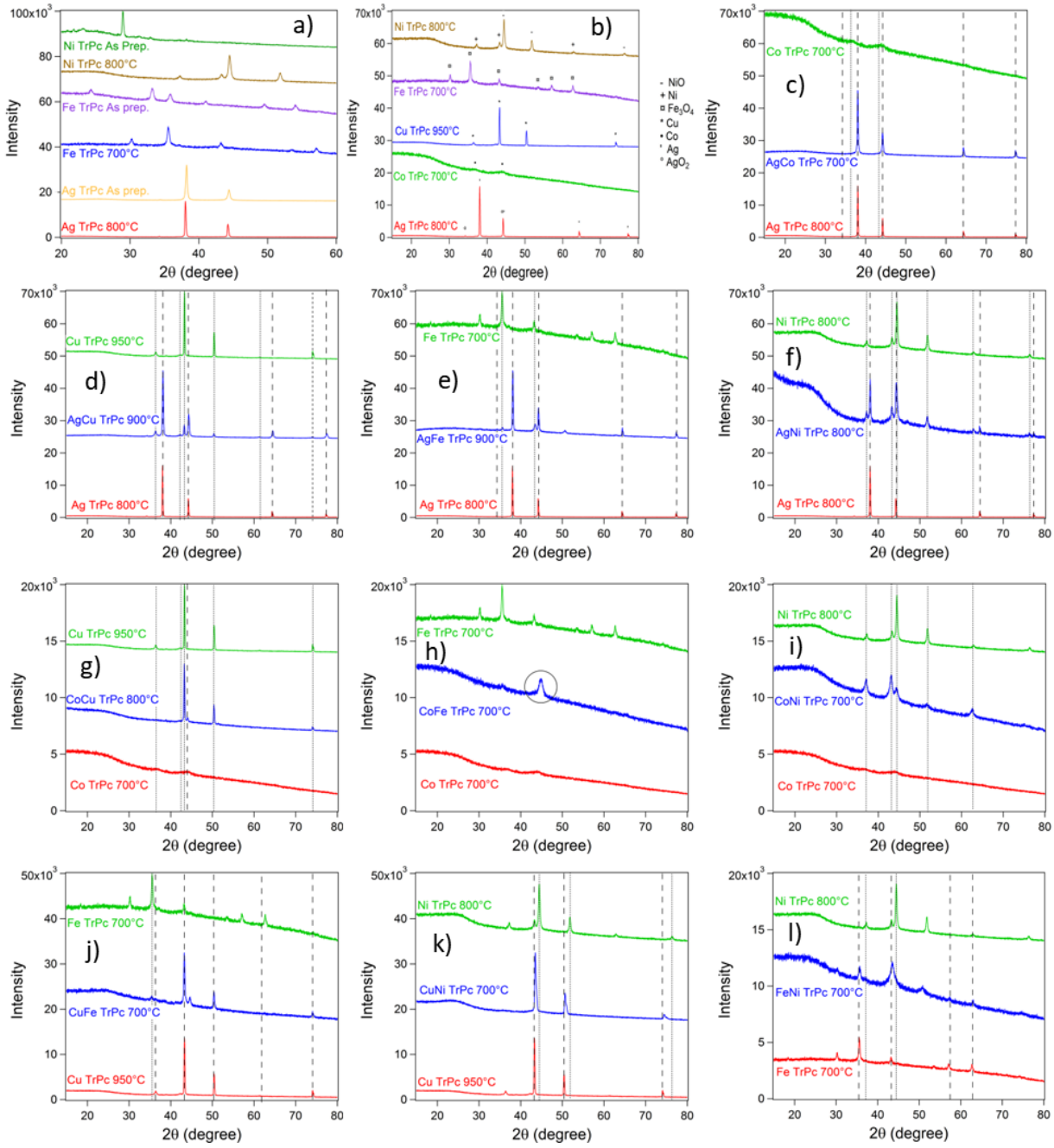

Figure 1.8: XRD spectra of the a) Ag, Fe, and Ni TrPc catalysts before and after pyrolysis, b) pyrolyzed single metal catalysts, and bi-metallic catalysts and the respective single metals c) AgCo, d) AgCu, e) AgFe, f) AgNi, g) CoCu, h) CoFe, i) CoNi, j) CuFe, k) CuNi, l) FeNi.

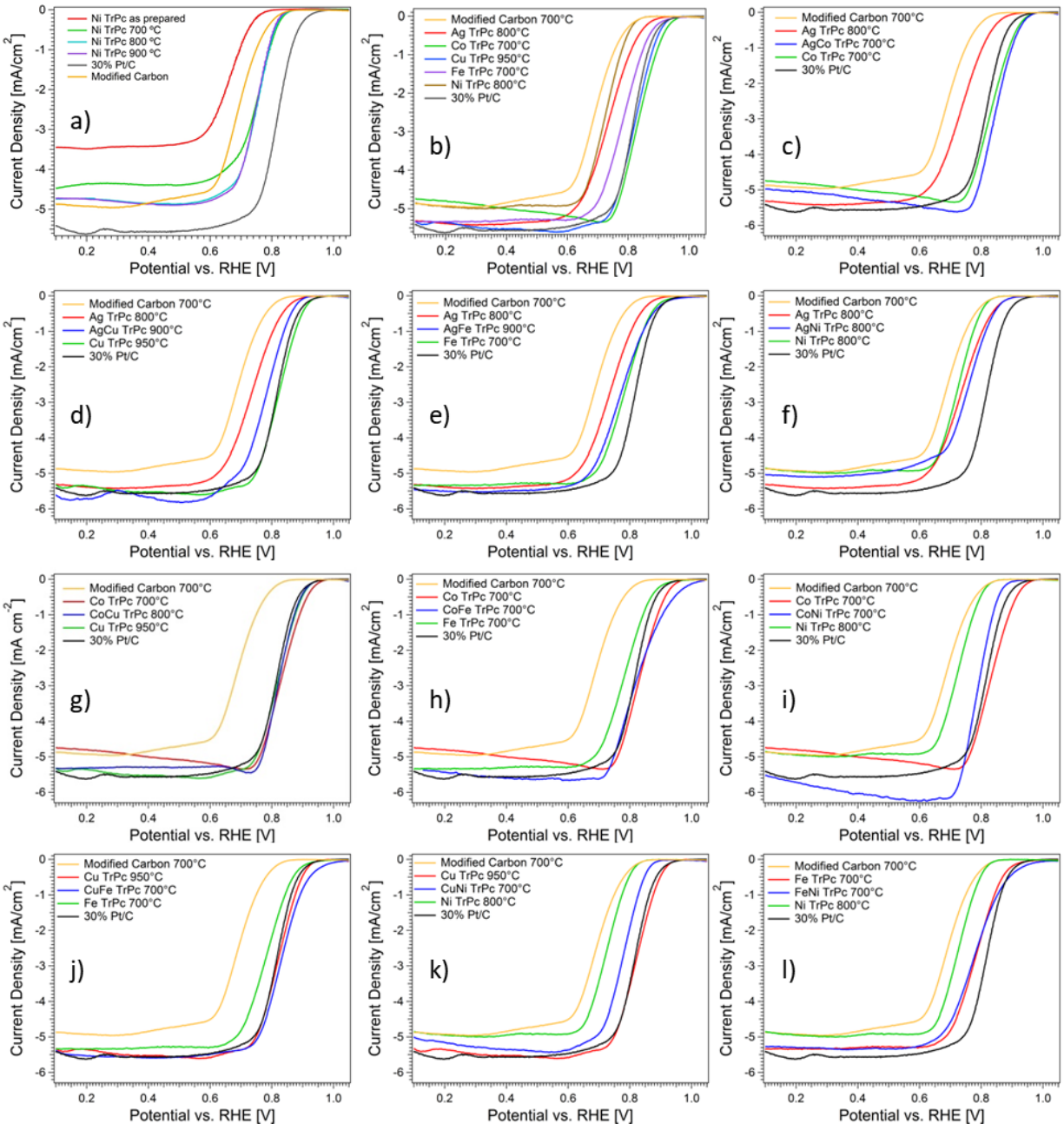

Figure 1.9: ORR RDE plots of the a) Ni TrPc at different pyrolyzation temperatures, b0 single metal TrPc catalysts, and bi-metallic catalysts and the respective single metals c) AgCo, d) AgCu, e) AgFe, f) AgNi, g) CoCu, h) CoFe, i) CoNi, j) CuFe, k) CuNi, l) FeNi. Oxygen Saturated 0.1 M KOH with 10 mV/s scan rate, 1600 rpm electrode rotation speed with Hg/HgO reference electrode and gold counter electrode.

Table 1.3: RRDE and physical parameters for Me TrPc HT catalysts. For electrochemical measurements: Oxygen Saturated 0.1 M KOH with10 mV/s scan rate, 1600rpm electrode rotation speed with Hg/HgO reference electrode and gold counter electrode.

Metal	Treatment Temp [°C]	Onset Potential [V]	$E_{1/2}$ [V]	J_L [mA/cm^2]	Tafel Slope [mV/decade]	BET [m^2/g]	O_2 Reaction Order	Stability $\Delta E_{1/2}$ [V]
Pt/C	N/A	0.949	0.817	5.62	59/122	--	0.692	0.10
Single Metals								
Ag	900	0.897	0.737	5.33	63.5	818	0.798	-37
Co	700	0.962	0.838	5.34	48.6	755	0.893	-2
Cu	950	0.946	0.821	5.57	54.1	782	0.891	-2
Fe	700	0.941	0.784	5.26	67.6	891	0.795	-8
Ni	800	0.837	0.728	4.88	41.0	792	0.744	-4
Bi-Metallic								
Ag/Co	700	0.967	0.849	5.61	48.7	738	0.950	-4
Ag/Cu	900	0.940	0.778	5.82	58.3	782	0.895	-6
Ag/Fe	900	0.949	0.770	5.49	73.9	958	1.378	-9
Ag/Ni	800	0.896	0.759	5.08	66	792	0.910	5
Co/Cu	800	0.948	0.833	5.13	44.8	668	0.848	-2
Co/Fe	700	1.027	0.822	5.63	78.6	823	0.874	0
Co/Ni	700	0.900	0.789	6.11	36.8	774	0.850	0
Cu/Fe	700	1.001	0.831	5.52	71.6	792	0.823	0
Cu/Ni	700	0.902	0.779	5.43	32.3	716	0.859	-2
Fe/Ni	700	0.972	0.779	5.29	96	1574	0.901	-3

For the AgCu TrPc 900°C, AgFe TrPc 900°C, CoCu TrPc 800°C, CoNi TrPc 700°C, and CuNi TrPc 700°C catalysts the activity is close to an average of the single metal catalyst components. The other catalysts appeared to be greater than an average of the parts. It was observed that the bimetallic catalysts containing iron had onset potentials at least 50 mV higher than the either of the respective single metal catalyst and the inclusion of cobalt increased the slope of the kinetic region.

Oxygen Reaction Order

The current at the disk electrode may be described by the equation:

$$J = nFk(E) \times (C_{O2}^{*})^{m} \times \left(1 - \frac{J}{J_L}\right)^{m} \quad [1.42]$$

Where J is the disk current, n is the number of electrons transferred, F is Faraday's constant, k(E) is a kinetic parameter, C^*_{O2} is the concentration of oxygen, m is the oxygen reaction order, and J_L is the diffusion limited current. The kinetic current (J_k) can be defined as:

$$J_k = nFk(E) \times (C_{O2}^{*})^{m} \quad [1.43]$$

Plots of J vs. E at different rotation speeds would be expected to be coincident at low overpotentials, i.e. below the onset of mass transport effects, since the kinetic current is independent of rotation rate. At overpotentials lower than the divergence, it can be assumed that the current is equal to the kinetic current, that is:

$$J = J_k \times \left(1 - \frac{J}{J_L}\right)^{m} \approx J_k = nFk(E) \times (C_{O2}^{*})^{m} \quad [1.44]$$

Therefore, the slope of a plot of log (J) vs. log (C_{O2}*) should be equal to the reaction order.

Figure 1.10a shows RDE curves for the Co TrPc 700°C catalyst at different scan rates in electrolyte saturated with 10% oxygen. The circled region on the plot marks the beginning of the divergence caused by mass transfer effects. At higher potentials Equation [1.44] can be said to be true. The divergence was found to occur at ~0.18 mA/cm^2 for both Pt/C and Co TrPc 700°C. In order to ensure the data was firmly within the kinetic region, the analysis for each catalyst was carried out at the potential which corresponded with a current of 0.1 mA/cm^2 for 10% oxygen saturation; this parameter will is referred to as $E_{J=0.1}$. Because the divergence occurs at higher overpotentials for higher oxygen concentrations, establishing the divergence point in the lowest concentration studied ensured the analysis was carried out below the onset of mass transport effects for all oxygen concentrations studied. To determine the reaction order, RDE experiments were conducted at 1600rpm with different partial pressures of oxygen ranging from 10-100%.

Figure 1.10b shows the RDE curves for the Co TrPc 700°C collected at each oxygen concentration. The dashed line in the plot represents $E_{j=0.1}$. Figure 1.10c shows a log (J) vs. log (C_{O2}*) plot which was determined to have a reaction order of m=0.893 for Co TrPc 700°C. This analysis was conducted for each catalyst and the results are summarized in Table 1.3. The reaction order was found to be 0.8-0.9 for most catalysts. This analysis was attempted with a Pt/C catalyst, resulting in a reaction order of 0.692; the deviation from the expected value of one may be due to the presence of oxide species on platinum at the relevant potentials.

The confirmation of reaction order sufficiently close to 1 allows the kinetic current to be extracted from the data using the Koutecky-Levich approximation (which can be derived from Equation [1.44] if m=1):

$$J_k = \frac{J}{\left(1-\frac{J}{J_L}\right)} \qquad [1.45]$$

Tafel Analysis

Tafel Plots were obtained by plotting the logarithm of the kinetic current against the IR corrected potential. Tafel plots for some of the single metal catalysts are shown in Figure 1.11. The Tafel slopes and other catalyst parameters for the single metal and bi-metallic catalysts can be found in Table 1.3. The observed Tafel slopes are generally between 40 and 70 mV/decade which is consistent with similar catalysts based in literature.[55–57] The Pt/C catalyst was found to have two Tafel slopes which is consistent with literature also[13,58]. The unclear nature of the catalytic site(s) with heat treated macrocycle catalysts limits the conclusions which can be drawn about the possible reaction pathway. However, in general, lower Tafel slopes are preferred because it requires lower overpotentials to reach higher current densities. From Table 1.3, one can observe that adding Fe to the catalysts increases the Tafel slope in each case; whereas adding Co decreases it.

Number of Electrons Transferred

In alkaline media, the ORR can precede through either a 2 electron reaction to produce peroxide [1.47], a 2+2 electron process with peroxide as an intermediate and a following reaction to produce hydrogen peroxide [1.47 + 1.48], or a direct 4 electron process to hydroxide [1.46]. The 4 electron processes are highly desirable as they maximize the power and efficiency of the cell. Furthermore, the direct process is preferred as peroxide species are notorious for degrading polymer electrolytes. RRDEs and the Koutecky-Levich equations are commonly used to determine the number of electrons transferred.

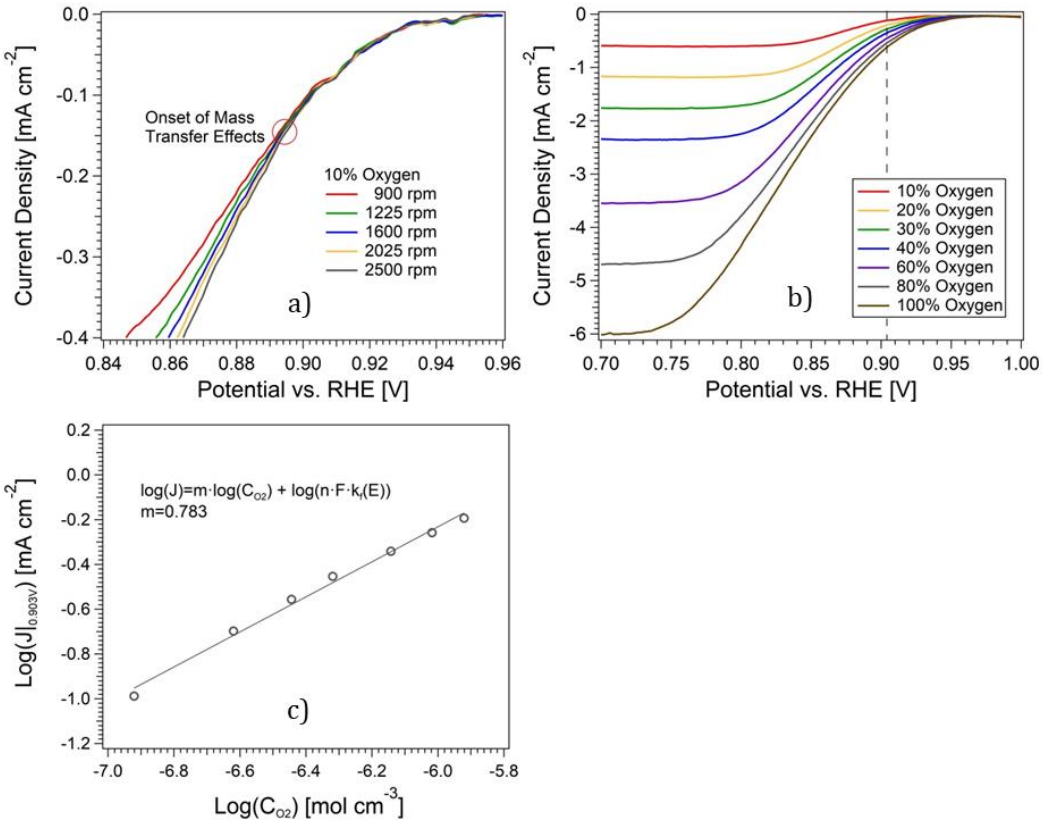

Figure 1.10: RDE voltammograms for the Co TrPc catalyst at different rotation speeds. The divergence of the curve marks the onset of mass transfer effects. **b)** RDE plots for Co TrPc 700°C carried out at different oxygen concentrations, c) plot of log-log plot of current density vs oxygen concentration. 0.1 M KOH with10 mV/s scan rate, 1600 rpm electrode rotation speed with Hg/HgO reference electrode and gold counter electrode.

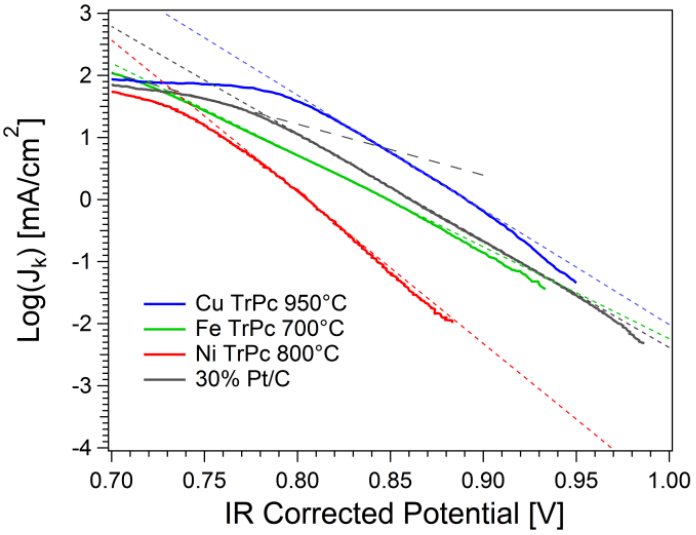

Figure 1.11: Tafel plots for the single metal catalysts derived from the plots in Figure 1.9.

$$O_2 + H_2O + 2e^- \leftrightarrow OH^- + HO_2^- \quad E = 0.904V \qquad [1.46]$$

$$HO_2^- + H_2O + 2e^- \leftrightarrow 4OH^- \qquad E = 1.708V \qquad [1.47]$$

$$O_2 + 2H_2O + 4e^- \leftrightarrow 4OH^- \qquad E = 1.278V \qquad [1.48]$$

RRDEs were conducted at 5 rotation speeds (625, 900, 1225, 1600, 2025, and 2500 rpm) and using 3 levels of catalyst loading (200, 400 and 600 μg/cm^2). The ring potential was held at 1.3 V vs RHE. Equation [1.49] describes how the number of electrons can be determined from RRDEs:

$$\boldsymbol{n} = 4\frac{I_D}{I_D - I_R/N} \qquad [1.49]$$

Where **n** is the number of electrons transferred, I_D is the disk current, I_R is the ring current and N is the collection efficiency (38%).

Figure 1.12a shows the number of electrons transferred for the Fe and Ni catalysts at different loadings. The effect of loading is more pronounced for the Ni catalyst, for which the number of electrons transferred decreases from 3.95 at 600 $\mu g_{PGM\text{-}free}/cm^2$ to 3.8 at 200 $\mu g_{PGM\text{-}free}/cm^2$. For the direct 4-electron pathway the number of electrons transferred would not be expected to depend on the catalyst loading. A higher apparent value for n may indicate that the catalyst layer at high loadings is too thick for the required geometry of the RRDE experiments. Alternatively, this suggests that the reaction proceeds through the 2+2 mechanism rather than the direct 4-electron. In this case a thinner electrode would give less opportunity for the peroxide to be further reduced to hydroxide within the catalyst layer. In either case, a low value for ***n*** at low catalyst loadings indicates that the catalyst may generate a significant amount of peroxide.

The number of electrons transferred is also commonly determined using the Koutecky-Levich approximation. If the reaction order is found to be close to 1 then Equation [1.42] will simplify to Equation [1.50], which is the Koutecky-Levich equation, with the limiting current density described by the Levich equation, Equation [1.51]:

$$\mathrm{J} = \frac{1}{J_k} + \frac{1}{J_l} \qquad [1.50]$$

$$J_L = 0.62\boldsymbol{n}FD_{o2}^{2/3}\upsilon^{-1/6}\omega^{1/2}C_{o2}^* \qquad [1.51]$$

$$\frac{1}{J} = \frac{1}{0.62\boldsymbol{n}FD_{o2}^{\frac{2}{3}}\upsilon^{-\frac{1}{6}}C_{o2}^*}\omega^{-\frac{1}{2}} + \frac{1}{J_k} \qquad [1.52]$$

The Koutecky-Levich approximation for determining **n** involves conducting RDEs at different rotation speeds and plotting the inverse of the current in the mass transport limiting

region as a function of $\omega^{-½}$ and solving the resultant slope for n according to Equation [1.52]. A representative plot is shown in Figure 1.12b for Ni TrPc and Fe TrPc catalysts with loading of 200 $\mu g_{PGM\text{-}free}/cm^2$ compared to a plot for Pt/C. From this data, the Fe catalyst has ***n*** = 3.95, while for the Ni catalyst ***n*** = 3.28. Unlike RRDE experiments, there is no dependence on the thickness of electrodes for the determination of n. Therefore, a deviation in the apparent number of electrons would suggest a 2+2 electron pathway. Only the Ni and AgNi showed a significant reduction in the number of electrons transferred with loading. This suggests that for most of the catalysts oxygen reduction takes place through a direct 4 electron pathway.

Table 1.4 shows values of n calculated using the Koutecky-Levich approximation and RDDE experiments for the lowest loadings tested. In general, the two techniques to determine ***n*** are in agreement. Achieving a number of electrons transferred close to 4 in a cobalt catalyst was somewhat surprising given the earlier discussion involving end-on adsorption of oxygen on cobalt species. Other workers have found that similar cobalt catalysts have generate significantly higher amounts of hydrogen peroxide in acidic media.[52] In acidic media the end-on adsorbed OOH species would be expected to react quickly with the free protons. In basic media, where the proton is supplied by water molecules, this reaction would be significantly slower if it occurred at all. Therefore, in basic media the OOH species will have additional time for further electro-reduction to produce hydroxide.

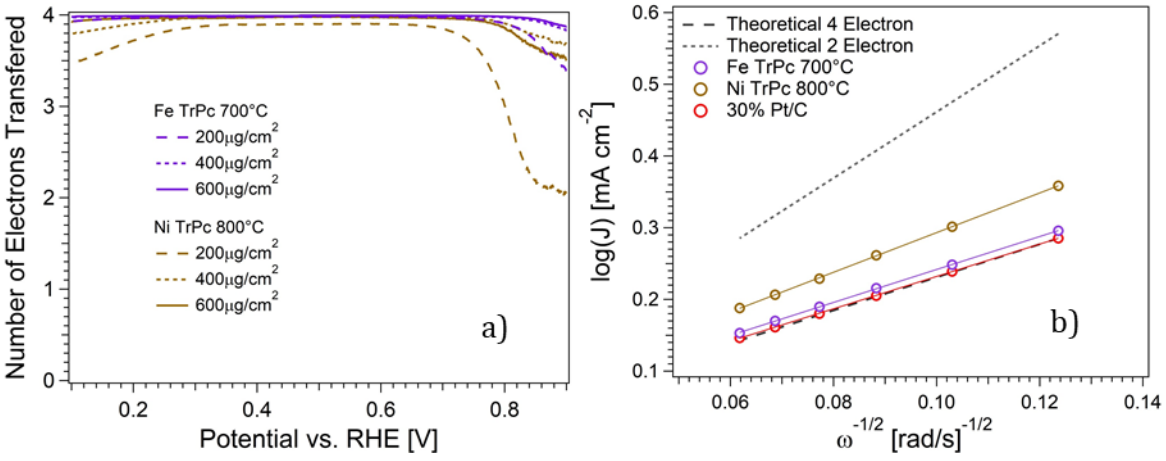

Figure 1.12: Number of electrons transferred calculated from a) RRDE data b)Koutecky-Levich approach

Table 1.4: n calculated from RDE data at 0.5V and the Koutecky-Levich approach for catalyst loadings of 200µg/cm^2

RRDE						Koutecky-Levich					
M	**Ag**	**Co**	**Cu**	**Fe**	**Ni**	**M**	**Ag**	**Co**	**Cu**	**Fe**	**Ni**
Ag	4.00	3.97	3.99	3.99	3.99	**Ag**	4.03	3.81	4.13	3.99	3.56
Co		3.98	3.97	3.98	3.96	**Co**		3.82	3.71	4.04	3.94
Cu			3.77	3.99	3.99	**Cu**			3.77	3.76	3.53
Fe				3.98	4.00	**Fe**				3.95	3.95
Ni					3.90	**Ni**					3.28

Catalyst Stability

The catalyst stability was tested using the RRDE experiment by cycling in the kinetic region of each catalyst (potentials between the half-wave potential ($E_{½}$) and $E_{½}$ + 0.25 V) 5000 times at 50 mV/s. Similar stability protocols have been previously reported by others[42,59–61]. Degradation was assessed by comparing to ORR half-wave potential ($E_{½}$) before and after cycling. This test was first conducted in nitrogen-saturated electrolyte as has been done previously[59]. No change was observed in the catalyst activity before and after cycling. To test the catalyst in a more challenging and realistic situation, the test was repeated in an electrolyte saturated with 20% oxygen and 80% nitrogen (close to air composition). As an example, Figure 1.13 shows the ORR curves of the CoFe TrPc catalyst before and after cycling. The changes in $E_{½}$ for each catalyst are displayed in Table 1.3. Cycling resulted in a $E_{½}$ potential decay of only a few millivolts, a result typical of all catalysts studied in this work, with only the silver mono-metallic catalysts with a loss higher than 10 mV. Cobalt-containing catalysts were the most stable. CoFe and CoNi catalysts showed no change in the $E_{½}$ after 5000 cycles. Conducting this test with Pt/C resulted in a slight increase in activity.

Removal of Excess Metal

Removal of excess metal in the catalysts with sulfuric acid and EDTA treatments was attempted. The acid treatment was found to nearly completely remove metallic particles from Co TrPc 700°C and Fe TrPc 700°C only; the other catalysts still showed metallic XRD peaks, although the intensity was lower. The EDTA treatment was unsuccessful, leaving behind large metal deposits which were visible in SEM images in each case.

The acid treatment of the catalysts was found to have a detrimental effect on ORR activity in RDE experiments for most catalysts, indicating that the catalytic centers are susceptible to acidic treatments, or that the metallic particles are catalytically active.

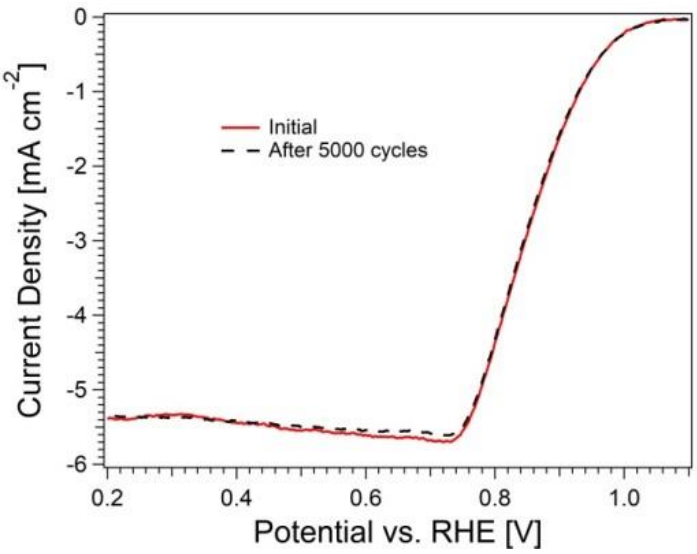

Figure 1.13: ORR activity of the CoFe TrPc 700°C catalyst before and after cycling in 20% oxygen saturated electrolyte. Oxygen Saturated 0.1 M KOH with10mV/s scan rate, 1600 rpm electrode rotation speed with Hg/HgO reference electrode and gold counter electrode.

XRD spectra of the single-metal catalysts before and after the acid treatment are shown in Figure 1.14a&b, respectively. Peaks associated with metals and metal oxides are clearly visible in the catalysts before and after acid treatment. After acid treatment the intensity of the peaks is reduced and width broadens for all catalysts, indicating the particle size was reduced. The use of harsher acids or longer treatment times, would be required to fully remove the metal; however, this may have a detrimental side-effects such as oxidizing the carbon support, which would increase corrosion as will be discussed later.

RDE experiments conducted on the acid-treated catalyst showed the treatment effected the onset potential and slope. Figure 1.15 shows the effect of acid treatement on the RDE activity of Cu TrPc 950°C, Fe TrPc 700°C, and Ag TrPc 900°C. Table 1.5 shows the change in the half-wave potential for all catalysts. For most of the catalysts the acid treatment resulted in a shift to a higher overpotential; only the catlayst with significant metal contents (Ag, Ni, AgCu, and AgFe) appeared to benefit from the acid treatment. This may be explained by the removal of inert metal from the catalyst resulting in higher effective loading of the catalysts.

The acid treatment was found to reduce the slope of the kinetic region for the Co, Cu, CoCu, CoNi, & CuNi catalysts, while the slopes were found to increase for the Ag & Fe containing catalysts as well as the Ni catalyst.

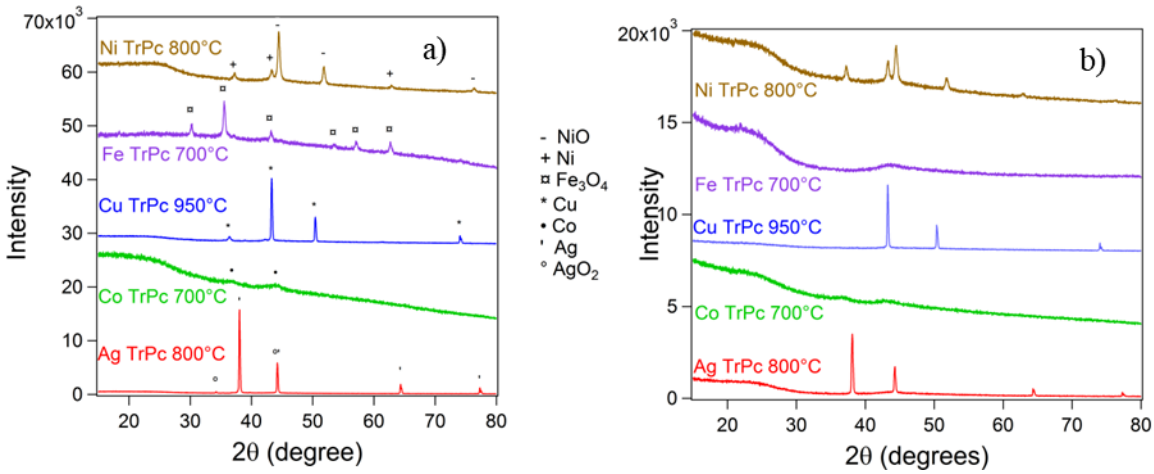

Figure 1.14: XRD spectra of the single-metal catalysts a) before and b) after acid treatment.

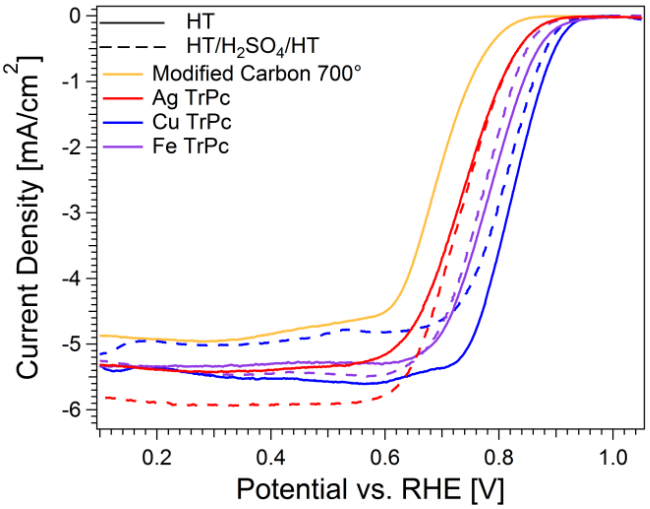

Figure 1.15: ORR Activity of catalysts before and after acid treatment. Oxygen Saturated 0.1 M KOH with10 mV/s scan rate, 1600 rpm electrode rotation speed with Hg/HgO reference electrode and gold counter electrode.

Table 1.5: Change in the half-wave potential (in mV) for the catalyst due to acid treatment

M	Ag	Co	Cu	Fe	Ni
Ag	+1	-2	0	+28	-19
Co		-37	-33	-8	-20
Cu			-9	-45	-13
Fe				-2	-3
Ni					+15

For the Cu TrPc 950°C catalyst the onset potential and slope are reduced after acid treatment while the onset of the Ag TrPc 900°C catalysts is unaffected, the slope of the kinetic region is increased and higher current densities are achieved. The onset potential of the Fe TrPc 700°C catalyst is reduced but the slope is increased. The differences in the slope of the RDE curves before and after acid treatment may indicate that there are multiple catalytic active sites which are effected differently by acid treatment. Further analysis of the catalyst sites can be investigated by selectively removing or poisoning the different sites expected to be present in these materials[42,48].

Selective Poisoning

Selective poisoning of the catalyst was conducted in an attempt to elucidate the activity of different active sites. Heat treated macrocycle catalysts may have multiple catalytic sites; Metallic particles, Me-N_x/C, and N/C sites have been proposed[42,44]. It is known that Me-N_x/C centers are poisoned with potassium cyanide (KCN)[40,42,44,48], while metallic particles and N/C centers are not.

To probe the activity of different active sites the ORR activity of the Fe TrPc before and after acid treatment was studied. The iron catalyst was chosen because the acid treatment was successful in removing nearly all the metallic particles. Figure 1.16 shows the effect of cyanide poisoning on the iron catalyst. The activity of the each test can be ascribed to:

A. Fe TrPc 700°C-Initial	Particles + Me-N_x/C + N/C
B. Fe TrPc 700°C-Poisoned	Particles + N/C
C. Fe TrPc 700°C/AT/700°C-Initial	Me-N_x/C + N/C
D. Fe TrPc 700°C/AT/700°C-Poisoned	N/C

The poisoned, acid treated sample (D) has the lowest performance and is quite similar to the control catalyst created without any metal. This indicates the N/C centers are the least active for ORR. Comparing the results before and after acid treatment (A&C) shows there is only a small change in activity, which suggests the metallic particles do not contribute significantly to the overall activity. Further evidence of this is given by the reduction in performance when KCN is added to the electrolyte with the non-acid treated catalyst (B). Here, the activity is between the initial catalyst and the control sample with no metal, indicating that while the metallic particles are ORR active, they are not primarily responsible for the observed activity. Therefore, we can arrange the different catalyst sites in order of decreasing activity from Me-N_x/C centers to metal/metal oxide particles to the N/C centers.

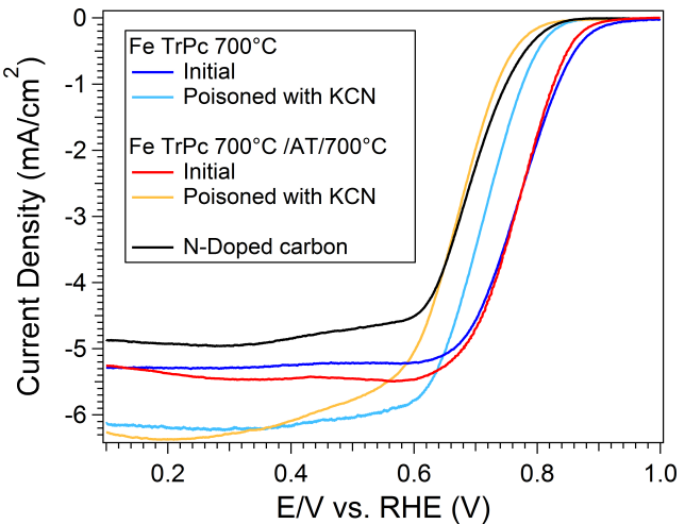

Figure 1.16: Effect of potassium cyanide poisoning on the Fe TrPc catalyst. Oxygen Saturated 0.1 M KOH with10 mV/s scan rate, 1600 rpm electrode rotation speed with Hg/HgO reference electrode and gold counter electrode.

AEMFC Testing

Figure 1.17 shows the full cell performance for hot-pressed MEAs in AEMFCs. These tests used the catalysts that surpassed Pt in our RRDE tests. The area-specific resistance (ASR) of the cells was fairly consistent, varying from 0.15-0.20 Ω/cm^2. From Figure 1.17a can be observed that at 0.6V the Pt/C catalyst reached a current density of 70 mA/cm^2 while the best PGM-free, Co-TrPc, reached 60 mA/cm^2. The performance of the AEMFCs constructed in this work is on par with that reported in the literature for other cells tested with A201 membranes[59,62,63].

In PEMFCs the HOR is facile compared to the ORR. For this reason, cell polarization is dominated by the cathode polarization and a reference electrode is generally not used. However, in alkaline environments the HOR is much slower, requiring higher overpotentials and higher catalyst loadings. To isolate the cathode behavior in AEMFCs, a reference electrode must be included. For this work, a Pd-coated Cu wire was used. The cell polarization was broken down into the contribution from the anode and cathode, shown in Figure 1.17b and c, respectively. The use of the reference electrode was found to be extraordinarily useful in this work. The anode performance was found to vary significantly from cell to cell even though the same set of conditions was maintained. The cause of this poor and variable performance will be further investigated in a later section.

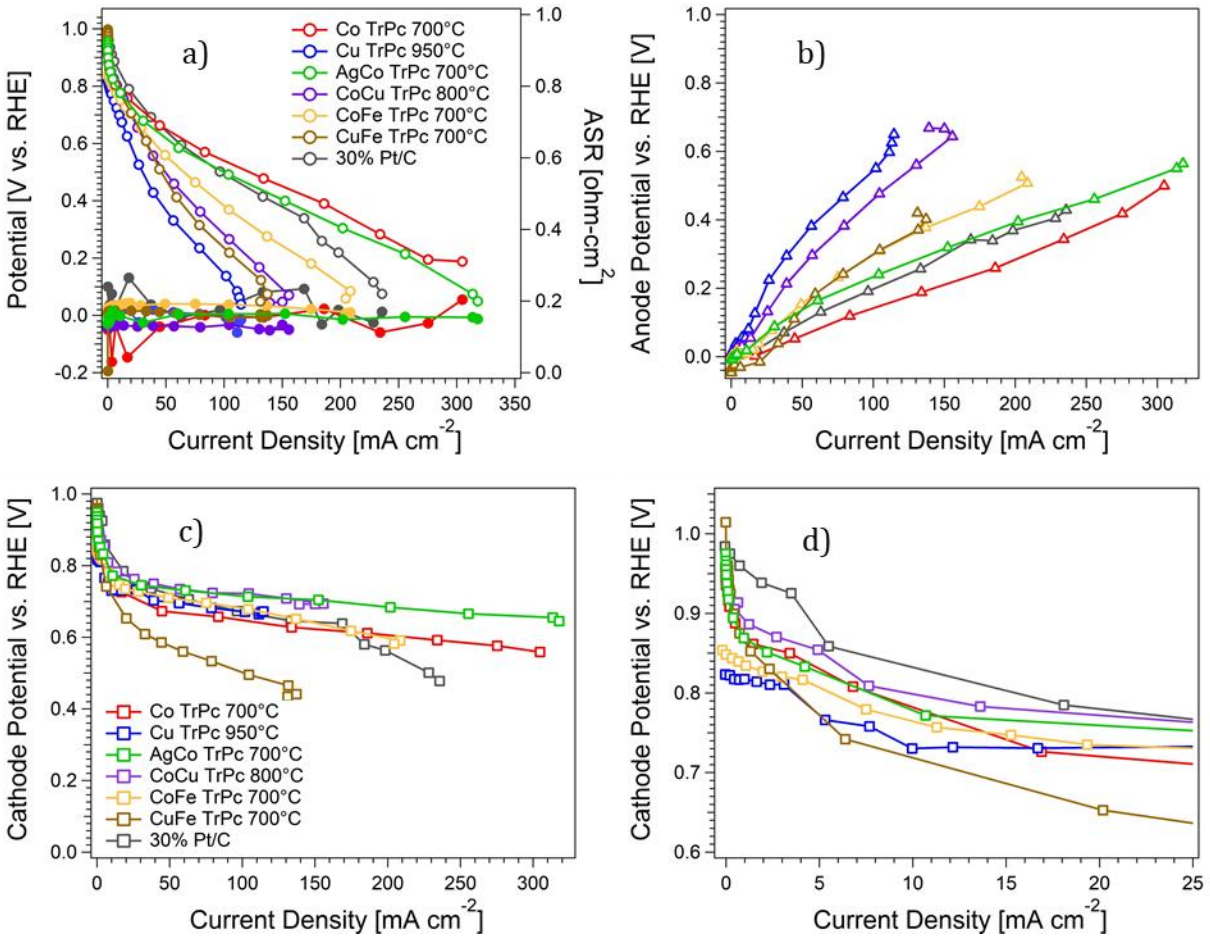

Figure 1.17: AEMFC polarization curves of the a) whole cell (with ASR shown), b) anode, and c) cathode using hot-pressed MEAs. D is a close-up of the kinetic region in a) Testing Conditions: 200 ml/min of 100%RH UHP H_2 and O_2 gas flow, 60°C cell temperature, ambient pressure, 0.4 mg_{Pt}/cm^2 or 1 $mg_{PGM\text{-}free}/cm^2$ loadings.

As shown in Figure 1.17d none of the catalysts are as active as platinum within the kinetic region. This indicates platinum is still a superior catalyst for AEMFCs at the loadings used. The performance of the PGM-free catalysts in comparison to each other in the AEMFC generally matches the observed trend from the RRDE studies. In the high current density region of Figure 1.17c, the performance of all but the CuFe catalyst was superior to Pt. The cathode polarization increase generally was modest after the initial strong decline. This indicates that our catalyst layers have at least sufficient mass transfer properties to support the current density shown and may indicate that the structure of the PGM-free catalyst layer is better for mass transport within the electrode. The single cell results highlight the importance of in-cell testing to confirm RRDE results. The catalysts with the highest activity in the *ex situ* testing did not give the best performance in the cell. It was evident that the catalysts which performed the best in an AEMFC all included Co. As discussed previously, the inclusion of Co in the catalyst decreased the Tafel slope leading to higher currents at larger overpotentials.

In PEMFCs, MEAs are prepared by hot-pressing the electrodes onto the membrane. This method helps to improve contact between the catalyst layer and the membrane, reducing contact resistance effects. Hot-pressing was conducted in the tests in Figure 1.17 under the assumption that the same would hold true for AEMFCs. For comparison, MEAs were prepared without hot-pressing, by just mechanically pressing the membrane between the anode and cathode in the cell. This method improved performance, especially for the MEA prepared using Pt/C as the cathode catalyst. At the cell potential of 0.6 V the current density for the Pt/C catalyst the current density was 70 mA/cm^2, and for the Co TrPc catalyst the current density reached 90 mA/cm^2. Figure 1.18a shows the cathode performance for Pt/C and Co TrPc mechanically-pressed vs. hot-pressed MEAs. For the Co TrPc catalyst, there is little difference in the kinetic region (enhanced in Figure 1.18b) between the MEAs, but a significant difference in mass transport region polarization curve. This indicates that the catalyst is not affected by the hot-pressing procedure but that the mechanically pressed MEA allows for better transport of water or oxygen to the electrode. Results were similar for the other PGM-free catalysts. For the Pt/C catalyst there is a significant improvement in performance in both the kinetic and mass transport regions of the polarization curve which indicates that the ORR on platinum is negatively affected by a process that occurs during hot pressing. It is known that the anion exchange ionomers and membranes are susceptible to degradation and it is possible that a degradation product poisons the platinum.

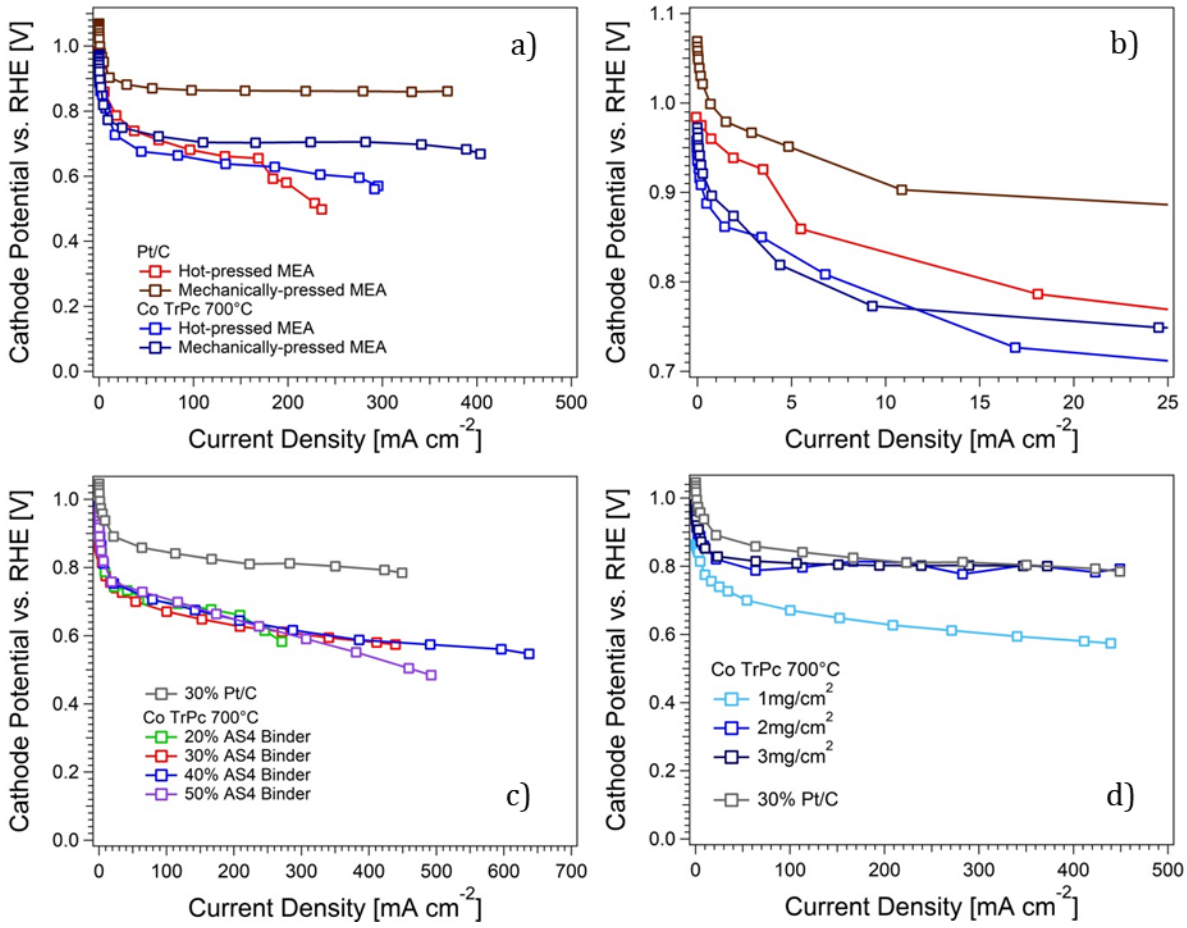

Figure 1.18: a) IR corrected cathode performance for hot-pressed and mechanically pressed MEAs with b) close of the kinetic region. IR corrected cathode polarization for AEMFC with c) standard cathode catalyst and different binder loadings and d) standard cathode binder and different catalyst loadings. Testing Conditions: 200 ml/min of 100%RH UHP H_2 and O_2 gas flow, 60°C cell temperature, ambient pressure, standard loadings for Pt.

The effect of catalyst loading and AS4 content in the electrodes was investigated with the Co TrPc catalyst. The cathode performances are shown in Figure 1.18c and d. The AS4 content in the catalyst layer was not found to have a measureable effect on cathode performance within the range of 20-50 wt%. The catalyst loading, on the other hand, had a significant effect on performance. Doubling the loading of the PGM-free catalyst to 2 $mg_{PGM\text{-}free}/cm^2$ resulted in a cathode performance on par with Pt/C in the high current density region. However, in the kinetic region the performance was still lower than that of Pt/C cathode. Further increase to 3 $mg_{PGM\text{-}free}/cm^2$ only resulted in a minimal performance change. The higher overpotential shown by the Co TrPc catalyst can be attributed to a possible lower number of active sites in addition to lower intrinsic activity.

Conclusion

A family of PGM-free catalysts was synthesized using an array of different metals to determine which metal or metal combination yields the best catalyst performance. Collaborating researchers studying the materials, using SEM, EDS and XRD, observed that different metals introduce marked differences, such as particle size, metal species and metal-metal interaction, in the final material.

The observed catalytic activity in RRDE experiments varied significantly based on the metal or metal combination used. The more noble metals Ag, Cu, and Ni required higher temperatures during the pyrolyzation and generally performed worse than more easily oxidized metals Fe and Co. Our results indicate that bi-metallic catalysts tend to perform better, with the CoFe combination having the highest activity. Adding Fe improves the catalyst onset potential, while adding Co helps to improve the ORR rate and catalyst stability.

The use of a reference electrode in AEMFC tests proved to be a key tool to interpret and understand polarization curves in the anode and cathode electrodes independently. Catalysts that showed higher ORR catalytic activity than Pt in the RRDE experiment did not match the activity of Pt in the kinetic region in the single cell experiment, indicating that the RRDE experiment, often used by researchers to compare PGM-free catalysts to Pt, is not the best metric for real AEMFCs applications. It was also observed that the Co containing catalysts had the best performance in the AEMFC, likely due to the higher ORR reaction rate.

By using 2 mg/cm^2 catalyst loadings for the PGM-free catalysts in the AEMFC it was possible to match the performance of Pt electrodes (1.33 $mg_{Pt+support}/cm^2$) in the high current

density region of interest in fuel cells. AEMFC single tests highlighted issues for further study, including the poor performance of AEMFC anodes and poor membrane stability.

Chapter 2: Bifunctional Oxygen Catalysts for Zinc-Air Batteries

Introduction

Lithium Ion battery technology is integral to modern technological devices. It is the power source of choice for virtually all consumer electronics such as laptops, cell phones and battery powered vehicles. In recent years, it has become clear that the limits of lithium ion technologies are quickly being reached with only small gains in performance stemming from optimization of components. This has led to a recent push in the development of next-gen battery technologies.

The necessity is clearest in transportation applications. Gasoline, which is by far the most widely used fuel for passenger vehicles, has an impressive specific energy of approximately 13,000 Wh/kg. However, the poor tank to wheel efficiency of internal combustion engines means less than 15% of the energy in gasoline results in vehicle motion. The practical specific energy of gasoline for vehicles is close to 2,000 Wh/kg. This is still an order of magnitude higher than current lithium ion batteries which have specific energies of 200-250 Wh/kg. Clearly, there is a need for new technology.

Different battery technologies are often compared based on their energy density or specific energy. The energy density and specific energy are a measure of the amount of energy stored in a battery normalized to its volume or weight, respectively. For transport applications, both parameters are important. Other important parameters are the operating potential, and charge and discharge rates. Several strategies have been proposed to develop batteries with higher specific energy and energy densities. Among these strategies is the use of multivalent metals such as magnesium and aluminum, solid metal electrodes, and oxygen from the atmosphere.

In current lithium ion batteries, lithium metal atoms are intercalated in a graphite or silicate electrode. As the battery is discharged the lithium sheds its electron and moves through a thin separator and is intercalated into a metal oxide electrode. One strategy to develop higher energy density batteries is to replace the lithium with elements such as magnesium and aluminum which have higher oxidation states and can provide 2 and 3 electrons, respectively. While this would increase the energy density, the fact that both of these elements have significantly higher masses than lithium means the gains in specific energy may be minimal. Furthermore, the reduction potentials for Mg (2.37V) and Al (1.66V) are also significantly lower

than Li (3.05V), meaning the power density of the cells will be significantly diminished. The only metal which has a higher charge per atomic mass than lithium is beryllium. Beryllium is only 1/10th as abundant as lithium, 10 times more expensive, toxic, and has a reduction potential of only 1.85V. For these reasons beryllium ion batteries are impractical.

Another proposed method to increasing the energy density of lithium based batteries is to use solid lithium metal electrodes as opposed to lithium intercalated in graphite. Graphite can accommodate one lithium atom for every 6 carbons[64]. Therefore the total lithium content of the electrode is below 10% by mass. By using lithium metal it may be possible to develop batteries 10x higher energy density. Primary, or single use, lithium metal anode based batteries are available on the market. However, lithium metal is well known for forming dendrites on cycling which may threaten to pierce a separator, cause a short, and potentially ignite the non-aqueous electrolyte. Strategies to mitigate dendrite formation would likely add weight and complexity to the cell decreasing the gains achieved by using metal electrodes.

Realistically, in order to achieve a radical increase is energy density a change in battery chemistries will be needed. For instance, using a redox participating chemical on the cathode of lithium ion batteries would increase the energy density of the cell. Lithium-sulfur batteries are commercially available and have specific energy and energy densities up to twice as high as current lithium ion batteries[65]. Metal-air batteries are perhaps the most attractive option for next generation battery technologies. They have theoretical energy densities up to 10 times greater than lithium ion batteries depending on the metal[2]. The gains in energy density for metal-air batteries stems from the use of oxygen from the atmosphere as half of the battery chemistry, reducing the weight and size of the cell. The practical specific energy of metal air batteries could be on par with gasoline engines.

Various metals have been considered as candidate materials for metal-air batteries including Li, Na, Mg, Al, Ca, Fe and Zn[66]. A comparison of cell voltages, specific energy, and energy densities for these systems are shown below in Table 2.1. Among these materials lithium-air garnered a significant amount of attention due to its high energy density. However, serious challenges face the development of practical Li-air batteries such as side reactions between lithium and the electrolyte, sensitivity to water from the atmosphere, low efficiency, and poor understanding of the kinetics[66,67]. The actual energy density of lithium air batteries is expected to be only ⅓ to ¼ of the theoretical values[2].

Table 2.1: Battery Energy Density and Specific Energy comparison (Summarized from [68]).

Battery	Cell Potential (V)	Specific Energy (Wh/kg)	Energy Density (Wh/L)
Li-ion	3.70	416	1450
Li-Air	2.93	5252	10600
Na-Air	1.97	1703	3870
Mg-Air	3.03	4032	14400
Al-Air	2.75	4332	17300
Ca-Air	3.11	2972	9960
Zn-Air	1.68	1109	6220

The high specific energy magnesium and aluminum air batteries are also promising; however, they receive relatively little attention in the literature. Zinc-air batteries (ZABs) have relatively low specific energies in comparison with other metals for use in air batteries. The advantages of zinc are abundance, low price, stability, and environmental benignity. Furthermore, the operating voltage of ZABs is low enough that an aqueous electrolyte may be used, thereby avoiding concerns of flammability experienced with lithium batteries. ZABs have been available commercially since the 1970s in the form of single use button cells. However, applications such as consumer electronics and electric vehicles necessitate the use of rechargeable batteries. There are many problems that affect rechargeable ZABs and have thus far proven to be an impediment to commercialization. The development of rechargeable ZABs has been complicated by poor oxygen electrocatalysis, dendritic growth issues, and instability of electrolyte due to carbonate formation and drying out[69–71].

The issues faced by rechargeable zinc air batteries are similar to major issues faced with other metal air battery technologies. In addition to making progress towards viable rechargeable zinc-air batteries, research into components for zinc-air batteries may provide insight and strategies that would aid in the development of air batteries using different metals.

Rechargeable ZABs have a high disparity between charging and discharging voltages, making them inefficient. The majority of this inefficiency arises from the large overpotentials required to both reduce and evolve oxygen. A diagram showing the electrode polarizations at different current densities is shown in Figure 2.1.

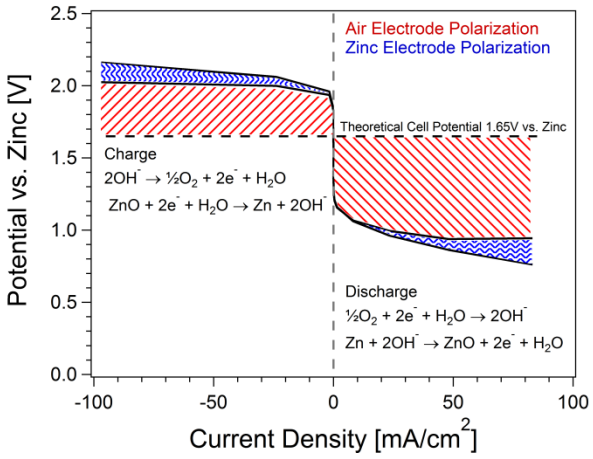

Figure 2.1: Zinc-air battery electrode polarizations during charge and discharge.

Air electrodes in metal-air batteries generally take one of a few forms. In some cases separate electrodes are used for the oxygen reduction reaction and evolution reaction. This way each electrode can be separately optimized for the required characteristics, e.g. hydrophobicity, catalyst type and loading, etc. However, this would add considerably to the weight and size of the cell, reducing the gains in energy density over current technology. The use of separate catalysts individually optimized for oxygen reduction and evolution in the same electrode has also been suggested. However, it is known that many oxygen reduction catalysts, such as Pt/C, are not stable at the high potentials required for the oxygen evolution reaction. The third option is to use a bifunctional catalyst capable of carrying out both the oxygen reduction and oxygen evolution reaction. Using appropriate bifunctional catalysts will keep the size and weight of the cell to a minimum while ensuring proper stability.

Historically, research into bifunctional oxygen catalysts has centered on various types of transition metal oxides. These materials generally have large particle sizes, poor electrical conductivity, and mediocre oxygen reduction activity.

ORR on Transition Metal Oxides

Many transition metal oxide and mineral oxide materials, such as perovskites (ABO_3), pyrochlores ($A_2B_2O_6$), spinels (AB_2O_4), and various forms of manganese oxide, show ORR activity in alkaline environments. Many of these materials are semiconductors, as such they are typically supported on metallic or conductive carbon supports. One drawback to oxide materials is their typically large particle sizes, which results in low surface areas.

Manganese Oxides

The oxygen reduction activities of different forms of manganese oxide are significantly different. Studies have shown that the activity increases from Mn_5O_8, Mn_3O_4, Mn_2O_3, and MnO_2[72]. The differences in activity even between nominally similar forms of MnO_2 are remarkable; Cao et al found the oxygen reduction activity increases in the order $\beta<\lambda<\gamma<\alpha=\delta$[73]. This trend exactly followed the reduction potential of MnO_2 to MnOOH which was highest in δ and lowest in β; this trend indicates that a surface redox reaction plays a role in the oxygen reduction mechanism. Besides onset potential, some forms of MnO_2 appear to catalyze ORR through a majority 2 electron processes while others appear to proceed through a majority 4 electron process.

Chabre and Pannetier reviewed the structure and electrochemical properties of different forms of manganese dioxide[74]. The difference in catalytic activity of the different forms of manganese oxides likely arises from the stability of crystal structure. β-MnO_2 is the densest and most pure form of manganese dioxide as indicated by its lower reduction potential it is also the most stable form. λ-MnO_2 has a spinel type structure, it is formed by the removal of intercalated lithium in $LiMn_2O_4$, and like the β form it has a distorted HCP structure. The remaining forms of MnO_2 are regarded as having a layered structure containing intercalated alkali, alkali earth ions, or water. γ-MnO_2 has been attributed to an intergrowth of β-MnO_2 and Ramsdellite MnO_2. α-MnO_2 has been characterized as $A(Mn^{4+},Mn^{3+})_8(0,0H)_{16}$, where A is a large cation, Ba^{2+} in natural systems. δ-MnO_2 has been described as having a similar composition to α-MnO_2 with very fine crystal sizes.

The forms of MnO_2 with layered and tunnel structures, γ, α, & δ, show higher ORR activities and onset potentials due to the ease in which the proton can be incorporated into the structure. The type of MnO_2 also has an effect on which type of MnOOH forms. For instance reduction of β-MnO_2 leads to the formation of γ-MnOOH[74,75]; in contrast γ-MnO_2 leads to δ-MnO_2[74]. Tye found that the discharge β-MnO_2 lead to a form of MnOOH in which was not dissociated while β-MnO_2 resulted in a dissociated form of MnOOH ($Mn(III)O + OH^-$)[76]. β-MnO_2 is reported to proceed through the 2 electron process.

Given the dependence of ORR onset potential on the surface redox couple potential, the first step in oxygen reduction on manganese dioxide electrodes is likely the reduction of MnO2 to MnOOH. This is followed by the adsorption of oxygen and oxidation of the metal center by the adsorbed oxygen. For the denser, more stable forms of MnO_2, β & λ, the hydroxide in the

reduced form, γ-MnOOH, is associated with the metal center. This would be expected to lead to weaker interaction between the metal and adsorbed oxygen; which may lead to the end on adsorption model. The weak interaction between the metal and the dioxygen molecule is likely insufficient to result in cleavage of the O-O bond in a significant proportion. Therefore ORR on the β & λ MnO_2 may proceed through the 2 electron process, as has been experimentally observed[77], in a scheme such as the following:

$$\beta - Mn(IV)O_2 + H_2O + e^- \rightarrow \gamma - Mn(III)OOH + OH^- \quad [2.1]$$

$$\gamma - Mn(III)OOH + O_2 \rightarrow Mn(IV)OOH - OO^- \quad [2.2]$$

$$Mn(IV)OOH - OO^- + e^- \rightarrow \beta - Mn(IV)O_2 + OOH^- \quad [2.3]$$

For the layered structures γ, α, & δ, the hydroxide in the reduced form, δ-MnOOH, is disassociated. This would be expected to lead to greater interactions between the metal and the adsorbed dioxygen molecule. If two centers are involved, the process may involve the cleavage of the oxygen bond, leading to an overall 4 electron process, which has been reported for γ & α MnO_2[73,77]. This could proceed through a scheme such as the following:

$$\gamma - Mn(IV)O_2 + H_2O + e^- \rightarrow \delta - Mn(III)O - OH^- + OH^- \quad [2.4]$$

$$2(\delta - Mn(III)O{-}OH^-) + O_2 \rightarrow Mn(IV)O - O - O - O(IV)Mn + 2OH^- \quad [2.5]$$

$$Mn(IV)O - O - O - O(IV)Mn + 2e^- \rightarrow 2\gamma - Mn(IV)O_2 \quad [2.6]$$

Step 3 as rate limiting would explain the experimentally observed dependence on oxygen concentration and Tafel slope determined by Cao et al for ORR on γ-MnO_2[73].

ORR on Perovskites

Perovskites with the crystal structure ABO_3, are by far the most researched mineral oxide catalysts for ORR. The properties of perovskites can vary widely depending on the choice of A and B site element. The A site is necessarily a large cation; otherwise the structure would likely be corundum or bixbyite. B site is most commonly a first row transition metal, Co, Ni, and Mn being the most popular. Doping of both sites has also been shown to dramatically affect properties. The Goldschmidt tolerance factor compares the radii of the A and B site atom to describe the distortion of perovskite structures.

$$G = \frac{r_A + r_o}{\sqrt{2} * (r_B + r_o)} \quad [2.7]$$

Where r_A, r_B, and r_o are the radii of the A site, B site, and oxygen, respectively. Factors between 0.9-1 will give cubic structures, factors between 0.7-0.9 will give tetragonal or orthorhombic structures and factors below 0.7 will not result in perovskites.

Hyodo et al. studied MMnO3 perovskites where M was a trivalent lanthanide ion or yttria, a correlation was established between increasing A site ionic radius and activity[78]. Lanthanum is commonly used because it has the largest ionic radius for the trivalent state among stable elements. The Goldschmidt tolerance factor for $LaBO_3$ (M=Mn, Fe, Co, or Ni) perovskites range from 0.84-0.88 while YBO_3 perovskites range from 0.8-0.84. Smaller ionic radii for the A site ion lead to greater distortion of the B site atom. This may indicate, as seen with spinels[79], the cubic phase may be more active towards ORR. Doping of the A site with a divalent alkali earth metal has also been shown to affect ORR activity by affecting the valence state of the B site metal[5].

Suntivich et al. conducted a systematic study in which B site atom was changed and the A site was selectively doped with Ca to establish trends in ORR activity[5]. Cr, Mn, Fe, Co, Ni, and Cu were investigated and it was found that the activity depended on the number of electrons in the D orbital. In particular the study found that the filling of the e_g orbital had a remarkable effect on the catalytic activity. Too much e_g filling was found to prevent oxygen adsorption, while too little filling resulted in passivation by hydroxide. Tafel slopes for different perovskites were all found to be close to 60mV/decade which likely corresponds to a first electron transfer to adsorbed oxygen, step 2 in the following scheme, as rate determining.

$$O_2 + {}^\circ \rightarrow {}^\circ O_2 \quad [2.8]$$

$${}^\circ O_2 + e^- \rightarrow {}^\circ O_2^- \quad [2.9]$$

$${}^\circ O_2^- + H_2O + e^- \rightarrow {}^\circ OOH + OH^- \quad [2.10]$$

$${}^\circ OOH + e^- \rightarrow {}^\circ O + OH^- \quad [2.11]$$

$${}^\circ O + H_2O + e^- \rightarrow {}^\circ OH + OH^- \quad [2.12]$$

$${}^\circ OH + e^- \rightarrow {}^\circ + OH^- \quad [2.13]$$

Other methods have been proposed to further increase the activity of perovskite catalysts. Introducing strain into the crystal structure by quenching hot catalysts, substituting A site atoms, or heteroepitaxy has been shown to increase catalytic activity[80,81]. The proposed mechanism for the increase activity is the altering of the spin state of the B site atom[80]. There are various methods for the synthesis of perovskites including solid state, sol-gel, and co-precipitation. After

synthesis the precursors are typically annealed in either air or oxygen environments at 700-1000°C[81,82]. This process typically results in particles ranging from several hundred nanometers to several microns[5,82,83]. Precious metal catalysts used for fuel cells are typically on the order of 5nm, and it is well known that catalytic activity is highly dependent on the size of the catalyst particle. Structuring perovskites on a nano-level may prove a challenge because they tend to agglomerate during heat treatment. Ball-milling is sometimes used to grind perovskites into smaller structures[82]. Harden et al. showed that freeze-drying the catalyst precursor before heat treatment lead to particles in the 20-50nm range; this was found to have a dramatic effect on both the oxygen reduction and evolution activity[83].

During long term testing of perovskites with mixed A sites in solid oxide fuel cells, a phase separation has been observed. The divalent A atom forms an oxide, which typically migrates to the electrode/electrolyte interface, reducing surface area and increasing cell resistance[84]. It is therefore important to ensure that the structure is stable.

Oxygen Evolution on Metal oxides

Within the relevant potential region of the oxygen evolution reaction nearly all catalyst surfaces will be coated with oxide or hydroxide layers. Among metal oxides catalysts the highly active ruthenium and iridium oxides are considered benchmarks; however due to the rarity of both metals there has been an extensive research effort into the development of non-precious metal OER catalysts.

The most cited OER mechanism for metal oxides is reported to be[10,85]:

$$^{\circ}OH + OH^{-} \rightarrow {}^{\circ}O + H_2O + e^{-} \quad [2.14]$$

$$^{\circ}O + OH^{-} \rightarrow {}^{\circ}OOH + e^{-} \quad [2.15]$$

$$^{\circ}OOH + OH^{-} \rightarrow {}^{\circ}OO + H_2O + e^{-} \quad [2.16]$$

$$^{\circ}OO \rightarrow {}^{\circ} + O_2 \quad [2.17]$$

$$^{\circ} + OH^{-} \rightarrow {}^{\circ}OH + e^{-} \quad [2.18]$$

Where, °X denotes a surface adsorbed species[1]. Observed Tafel slopes in the range 35-45 mV/decade correspond with step 2, the formation of the dioxygen bond, as rate determining[85,86]; which qualitatively makes sense.

[1] Literature reports describe the mechanism in acidic environments; the mechanism above was modified for alkaline conditions.

Norskov and coworkers combined DFT calculations with experimental OER properties of a broad range of oxide materials including rutile oxides, perovskites, and spinels among others[10]. The study indicated that the reaction pathway was similar for a wide range of oxide materials. For an ideal catalyst the change in free energy for each step should be equal; for instance, since °OH and °OOH are separated by 2 electron and proton transfers the ideal separation between the steps would be 2.46 eV. However, it has been shown that on metal and metal oxide electrodes a constant difference of 3.2 ± 0.4eV was observed between the adsorption energies of OH and OOH. This difference leads to a minimum OER overpotential of (3.2 ± 0.4-2.46)/2, or at least 0.17V. In practice the overpotential for the most active catalysts (IrO2, RuO2, NiFe oxide, SrCoO3) is close to 0.25V[85].

The overpotential for OER was shown to correlate with the difference between the binding energies of O and OH with a volcano-like relationship[10,85,87,88]. Catalysts which bind O too strongly are limited by the formation of OOH (Step 2), while O binding that is too weak is limited by the oxidation of OH (Step 1). The optimum oxygen binding was found to be close to the midpoint of OH and OOH binding energies.

With a fundamental lower limit on the overpotential for the oxygen evolution reaction on metallic and oxide surfaces, future research on OER catalysts is relegated to finding the most stable and cheapest materials with this overpotential or the development of a radically new catalyst structure.

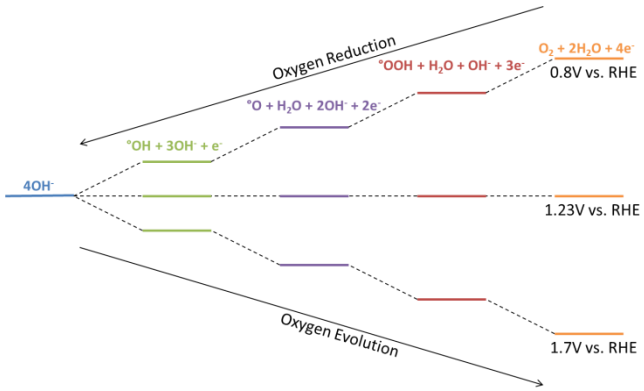

Figure 2.2: Reaction coordinate diagram for oxygen reduction and evolution reactions.

The linear relationship in binding energies of OOH and OH indicate that they adsorb on similar sites. It may be possible to synthesize OER catalysts which demonstrate lower overpotentials by altering the surface to increase the binding of OOH or decrease the binding of OH. In nature, enzymes catalyze the OER very efficiently, for instance in the $CaMn_4$ center of Photosystem II[89]. DFT calculations for Ni and Co modified RuO2 showed that Ni and Co introduced proton donor-acceptor states which altered the local surface property and modified the interactions with OH and OOH, resulting in theoretical overpotentials below 0.2V[9]. While these particular catalysts may be unstable in the environment of a ZAB, it suggests that surface modification via co-doping, organic molecule or anion adsorbate, may result in efficient OER catalysts.

Carbon Corrosion

Early fuel cells used Pt catalyst with large particle sizes. In an effort to reduce the cost per given surface area, the catalyst was scaled down to ~5-10nm paticles. This approach required the use of a conductive catalyst support to conduct electrons to and from the platinum nanoparticles. Conductive carbon materials have typically been used because of their chemical stability, low cost, decent conductivity, and light weight. However, it was observed that start-stop procedures or fuel starvation led carbon corrosion in the electrode, which would eventually lead to cell failure[90,91]. In alkaline conditions the corrosion is attributed to the reaction[91,92]:

$$C + 2OH^- \rightarrow H_2O + CO + 2e^- \quad [2.19]$$

$$C + 4OH^- \rightarrow 2H_2O + CO_2 + 4e^- \quad [2.20]$$

Carbon corrosion is believed to begin with the incorporation of oxygen at the edge sites of the graphene plane which later results in the removal of carbon dioxide or monoxide according to the scheme in Figure 2.3. The corrosion is therefore expected to be higher for high surface area carbons[93].

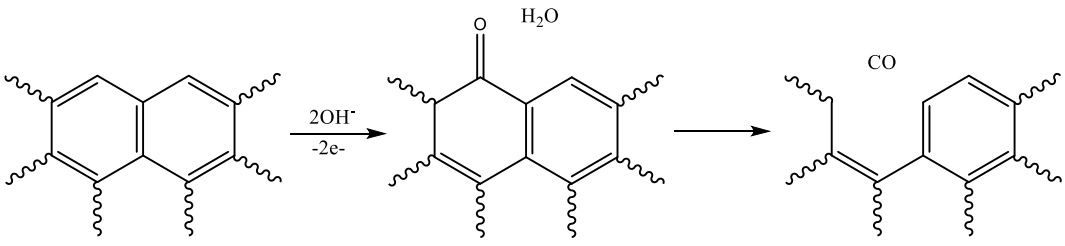

Figure 2.3: Representative mechanism of electro-oxidative carbon corrosion

Ross and coworkers studied the corrosion of carbon black supports within the relevant potential window for OER (1.4-1.6V vs. RHE)[92–95]. They determined that corrosion decreased with higher levels of graphitization. Among the supports, acetylene black was found to be particularly stable[93]; however the corrosion rate was still found to be around 1% weight loss per hour[94,95]. Most of the promising oxygen evolution catalysts are metal oxides and mineral oxides. These materials generally exhibit poor electronic conductivity; therefore the catalysts are usually supported on conductive carbon materials. Unfortunately, the incorporation of metal oxide catalyst was found to further increase the corrosion rate[95].

The corrosion of carbon in ZABs will have several effects on the cell. First the current from the corrosion of carbon leads to deviation from the desired stoichiometry and an increase in hydroxide concentration. The corrosion product, carbon dioxide, would form carbonate in the electrolyte, which can precipitate in the pores of the air electrode and block oxygen transport. Carbon corrosion can also lead to the destruction of the carbon support which would decrease the electrical conductivity of the electrode and may isolate the catalytic sites. Therefore, carbon corrosion is a significant issue in the long term operation of ZABs. Ex-situ half-cell experiments were conducted to determine the relative stability of different carbon support materials. Briefly, the carbon supports were dispersed in methanol to form an ink which was deposited onto a glassy carbon electrode. The electrode was cycled within a wide potential window in oxygen saturated alkaline electrolyte.

Figure 2.4 shows the effect of carbon corrosion after relatively few potential cycles on various carbon supports. Generally, the higher surface area and more amorphous materials exhibited the most corrosion. Unfortunately, metal oxide catalysts show the highest activities with these same supports. The acetylene black and graphite appeared not to be effected nearly as much and would be expected to be more appropriate supports for ZAB air electrode catalysts. However, in full cell experiments, when using a catalyst supported on graphite and acetylene black, a brown residue which has been attributed to carbon corrosion in previous experiments was observed after the cell had been tested. This suggests that non-carbon based supports should be investigated.

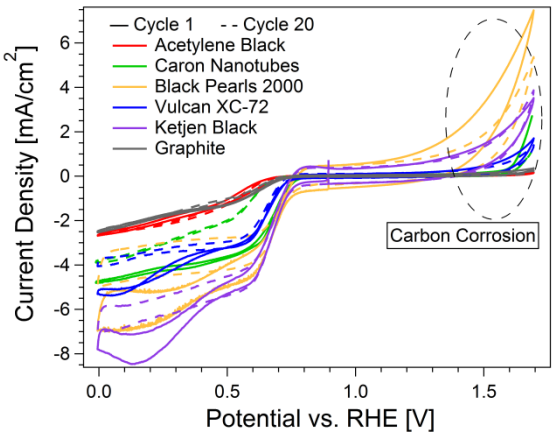

Figure 2.4: Corrosion of carbon support materials during high poten**tial** cycling. Oxygen Saturated 0.1 M KOH with 10 mV/s scan rate, 1600 rpm electrode rotation speed with Hg/HgO reference electrode and gold counter electrode.

Alternative catalyst supports for alkaline environments include conducting oxides such as tin or titanium oxide micro particles, transition metal nitrides and carbides, or 3-D structured noble or passivated metals such as nickel foam. Conducting oxides are typically substantially more resistive than carbon or metal electrodes, many of the most active transition metal nitrides show poor stability in alkaline environments and porous metal substrates typically have low surface area densities.

Experimental

Rotating Ring Disk Electrode Experiments:

Rotating ring disk electrode experiments were carried out using a multi-channel VMP3 potentiostat from Bio-Logic, a Pine instruments MSR rotator and RRDE electrode with a 0.2472 cm^2 glassy carbon disk and Pt ring (320 μm ring-disk gap, 6.25 mm and 7.92 mm ring inner and outer diameter, respectively). The RRDE collection efficiency *N* was measured experimentally and determined to be 38%. A gold counter electrode mounted in a glass tube with a frit at one end was used. A Radiometer Analytical XR400 Hg/HgO reference electrode with 1M KOH fill solution was used.

The potential of the reference electrode versus the reversible hydrogen electrode (RHE) was determined by saturating 0.1M KOH with hydrogen and measuring the OCV with a multi-crystalline Pt working electrode. Ultra-high purity (UHP) gasses from Airgas Co. were used for each experiment.

Inks were prepared using a 30 wt% Nafion® to 70 wt% catalyst ratio and methanol as solvent. Aliquots of the inks were solution-casted onto the GC disk electrode to reach loadings of

600 μg/cm^2. Catalysts were tested in aqueous 0.1 M KOH electrolyte. For each experiment, the electrolyte was de-aerated for at least 30min with nitrogen; voltammograms were collected between 1.1 and 0.1 V vs. RHE with a 10mV/s scan rate with the electrode static and rotating at 1600 rpm for background correction. This procedure was repeated in O_2-saturated electrolyte, with the ring held at 1.3 V vs. RHE to scavenge any peroxide generated at the disk electrode. The oxygen evolution activity of the catalysts was determined by collecting cyclic voltammograms between 0.9 to 1.7 V vs. RHE with a 10 mV/s scan rate while rotating at 1600 rpm.

Oxygen evolution stability experiments were conducted by alternatingly holding the electrode at 1.7 V vs. RHE for 2½ min then collecting an ORR CV. Additionally, some stability experiments were conducted comparing the most stable samples to non-precious metal oxide bifunctional catalysts by scanning the potential over the whole range (0-1.7 V vs RHE) at 10 mV/s several hundred times.

Zinc-air battery Air Electrode Preparation:

NPMCs inks were prepared by combining catalyst powders (70%) with PTFE (40%) and diluting 0.1 wt% with an equal IPA/water mixture. Platinum inks were prepared by mixing the catalyst inks were sonicated for at least 30min prior to spraying. The catalyst layers were spray painted onto Sigracet 25BC gas diffusion layers to achieve the desired loading (1, 2 or 4 mg_{NPMC}/cm^2).

Zinc-air battery Cell Testing:

A modified Fuel Cell Technology hardware was used for all ZAB testing. One graphite plate had a 5 cm^2 area recessed 0.5 mm in which a piece of zinc foil was placed. The other graphite plate used a standard serpentine flow channel. The air electrode was stacked in the cell with a membrane and the zinc foil. The ZAB tests were conducted using a proprietary anion exchange separator material developed in our lab. A palladium (Pd) coated Cu wire (synthesis details in supplementary information) was included in the cell as a pseudo-reference electrode; it was placed in contact with the membrane ~0.5 cm away from the electrodes. The cell was assembled and compressed to 80-inlbs of torque on each bolt.

The cell temperature, relative humidity (RH) and gas flow rates were controlled with a Fuel Cell Technologies test station. The cells were tested at 30°C with 200 ml/min of 100% RH oxygen gas flow and ambient pressure. Unless otherwise specified, 1 mg_{NPMC}/cm^2 was used as standard loadings for non-precious and precious metal catalysts, respectively.

Results and Discussion

Oxygen Reduction on Metal Oxide Catalysts

In order to optimize the efficiency of ZABs the disparity between the charge and discharge potentials must be minimized as much as possible. This can be accomplished by developing more active catalysts. Various metal oxides catalysts were synthesized and tested to evaluate their suitability for ZABs. The effect of catalyst support on activity and stability were assessed.

Manganese oxide was synthesized through a sol-gel process described elsewhere. The manganese oxide catalyst was combined with different supports and incorporated into RDE inks. Figure 2.5a shows the ORR activity of the catalyst compared to Pt/C for reference. The activity is very low by comparison. It is known that in alkaline conditions carbon materials are capable of catalyzing the ORR to a degree. For this reason an RDE curve for the bare glassy carbon (GC) electrode is included as a reference. It is clear that the MnOx has similar activity to the GC. It has been observed that for most catalysts, higher performance in RDEs can be achieved by increasing the loading. However, when this was attempted, it was found that the performance decreased.

Given that manganese oxides are poor electronic conductors, this observation could be explained by a thicker layer of the catalyst resulting in reduced conductance of the electrons to the catalytic sites which limits the ORRs. It is also possible, given the relatively similar performance of the manganese oxide and the GC electrode, that the manganese oxide electrode does not completely cover the surface of the glassy carbon, leaving a region of GC exposed to catalyze the ORR. In this case a higher loading would result in less exposed glassy carbon and lowered ORR activity.

To test this, electronically conducting catalyst support materials were included into the RDE ink. The chosen materials were acetylene black (AB), Ketjen Black (KJB), and Ni nanoparticles (~60 nm diameter). The RDE plots for the support materials, both with (solid lines) and without (dashed lines) manganese oxide, are shown in Figure 2.5b along with Pt/C for comparison. In each case the activity of the catalyst layer with manganese oxide is higher indicating that the low ORR activity observed in the unsupported catalyst is due to the poor electronic conductivity of the material. The performance of the supported catalysts increased dramatically, especially with the KJB support. Unfortunately, the Ni nanopowder support, which is expected to be the most stable, gave worse performance than either of the carbons.

Several different perovskites were prepared in accordance with the literature. The ORR activity of the materials was determined with and without carbon supports as shown in Figure 2.6. As with the manganese oxide catalysts, the activity of the unsupported catalysts was lower than the bare glassy carbon electrode. By including conductive carbon supports, the performance increased. The performance increased with additional percentage of carbon in the catalyst layer.

Even with the inclusion of conductive support materials to facilitate the transport of electrons to the catalytic sites, the activity of the metal oxide catalysts towards ORR was dramatically lower than Pt/C and other NPMCs described previously.

Oxygen Evolution on Metal Oxide Catalysts

The activity of the metal oxide catalysts towards the OER was also studied. Figure 2.7a shows the activity of the manganese oxide catalyst on different support materials. The activity is the highest when the catalyst is supported on Ketjen Black. However, given that the apparent onset potential is below 1.23 V and the high activity of the KGB itself, it is apparent that a significant portion of the current is derived from carbon corrosion. The activity of the catalyst supported on acetylene black is significantly lower in comparison, and the similar currents observed with the AB without catalyst present again suggests carbon corrosion effects the results. The activity of the nickel nanopowder alone was significantly higher than with the manganese oxide catalyst present. It is well established that nickel is one of the most active NPM OER catalysts.

The perovskite catalysts were tested with and without conductive support, as shown in Figure 2.7b. Within the relevant potentials there appeared to be little to no current observed from the catalyst support material, indicating the observed currents were likely derived only from the oxygen evolution reaction. Given the large increase in activity with the inclusion of the conductive carbon support is clear that poor electronic conductivity affects the OER activity in perovskites.

While the ORR activity of the different perovskites was fairly similar, it is evident that the OER activity varies greatly for different B site atoms. For the supported catalysts, the $LaMnO_3$ catalyst shows almost no activity while the activity of the $La_{0.5}Sr_{0.5}CoO_3$ and $LaCoO_3$ are fairly close, and the $LaNiO_3$ shows the best performance.

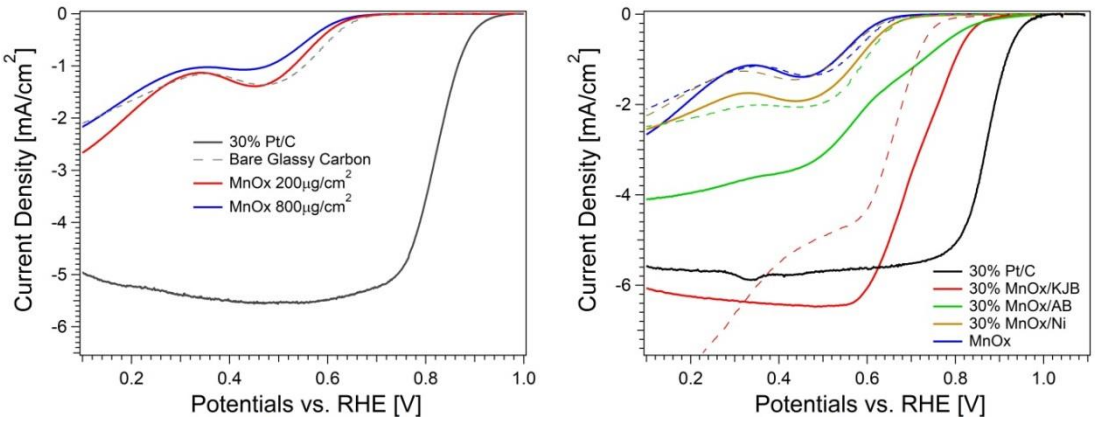

Figure 2.5: RDE curves for manganese oxide catalysts with a) different loadings and b) different catalyst supports. Oxygen saturated 0.1 M KOH, with 10 mV/s scan rate, 1600 rpm electrode rotation speed, Hg/HgO reference electrode, and gold wire counter electrode.

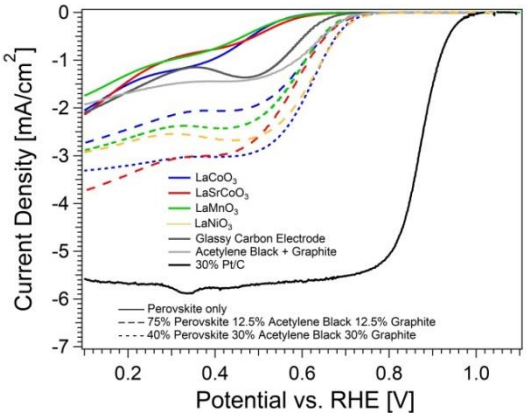

Figure 2.6: RDE curves for perovskite catalysts with and without conductive carbon supports. Oxygen saturated 0.1 M KOH, with 10 mV/s scan rate, 1600 rpm electrode rotation speed, Hg/HgO reference electrode, and gold wire counter electrode.

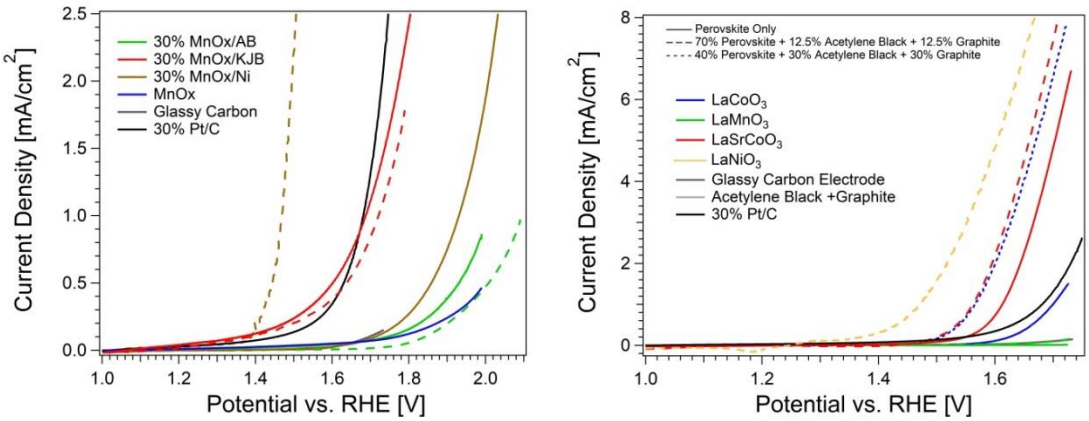

Figure 2.7: Oxygen Evolution behavior for a) manganese oxide catalysts on different supports (Solid lines represent supported catalysts and the dashed lines represent the activity of the support) and b) perovskite catalysts with and without carbon supports. Oxygen saturated 0.1 M KOH, with 10 mV/s scan rate, 1600 rpm electrode rotation speed, Hg/HgO reference electrode, and gold wire counter electrode.

Bifunctional NPM Heat Treated Macrocycle Oxygen Catalysts

While working with heat treated metal phthalocyanine-based catalysts described previously in the ORR section, it was observed that some showed activity towards the oxygen evolution reaction as well. The bifunctionality of these catalysts opens the possibility for their use as the positive electrode in metal air batteries.

Activity and Effect of Pretreatment

Each catalyst was tested for ORR and OER activity as prepared, after heat treatment, and after acid treatment. Figure 2.8 shows the XRD spectra and OER activity of the Ni TrPc catalyst in various states. A test was carried out on the carbon support, Black Pearls® 2000 (Cabot Corp), used for synthesis of the catalyst to determine how much carbon corrosion could contribute to the measured current. As is evident from the voltammograms, the current of the Ni TrPc catalyst in each state is significantly above that of the carbon, which indicates a most of the current is from oxygen evolution reaction.

Figure 2.8a clearly shows the XRD spectrum of the as prepared catalyst has only one significant peak at ~28, which is associated with the Ni TrPc complex. The CV of the catalyst demonstrated peaks consistent with the Ni(II) to Ni(III) transition. These transitions have been reported for nickel phthalocyanine complexes in the literature[96]. It likely that after transitioning to the Ni(III) state these macrocycle complexes in the as prepared catalyst become OER active.

Peaks associated with the phthalocyanine complex were observed in the XRD spectra of the other as prepared catalysts. Fe TrPc was the only catalyst to demonstrate metallic peaks in

the as prepared state, these were attributed to Fe_2O_3 and are likely the result of excess iron used during catalyst synthesis. Figure 2.9 shows the RDE plots for the each of the other catalysts in the three states. Only the catalysts which contain nickel are active before pyrolysis, the activity of the other catalysts is similar to the carbon support. This indicates only the nickel phthalocyanine complex is OER active. The Cu/Ni and Co/Ni catalysts were less active than the Ni catalyst, indicating there may be a dilution effect, while the Fe/Ni catalyst was more active.

The activity of the catalysts increased significantly after the pyrolyzation step. XRD analysis showed the formation of metal/metal oxide particles and the destruction of the phthalocyanine complexes during the pyrolyzation process. It is not clear if the metallic particles or new metal-ligand complexes incorporated into the graphene sheets are responsible for the increased activity.

The increase in current at low overpotentials, i.e. 1.2-1.4 V, after the pyrolyzation step(s) indicates that the process leads to increased carbon corrosion, making the catalysts less stable. The performance metrics for the pyrolyzed catalysts are given in Table 2.2.

Attempts were made to remove the metal particles with an acid treatment. The XRD spectra of the catalysts before and after acid treatment are shown in Figure 2.10. For all catalysts there was a significant decrease in the XRD peak intensity, indicating the size of the metallic particles was reduced in the process. Longer acid treatment times or the use of harsher acids would likely be required to fully remove the metallic particles. The activity of all catalysts containing Ni diminished after the acid treatment, indicating the nanoparticles are important for OER activity. For all of the other catalysts except Co/Cu the activity increased after the acid treatment.

Stability

The stability tests involved holding the catalyst at 1.7 V vs. RHE for 2.5 min and then collecting an ORR RDE curve and repeating. Figure 2.11 shows the results of the stability tests. Figure 2.11a shows the amount of charge passed during the OER hold normalized for each catalyst to the charge passed during the first OER step. Figure 2.11b shows the shift in ORR half-wave potential of each catalyst normalized to the initial value.

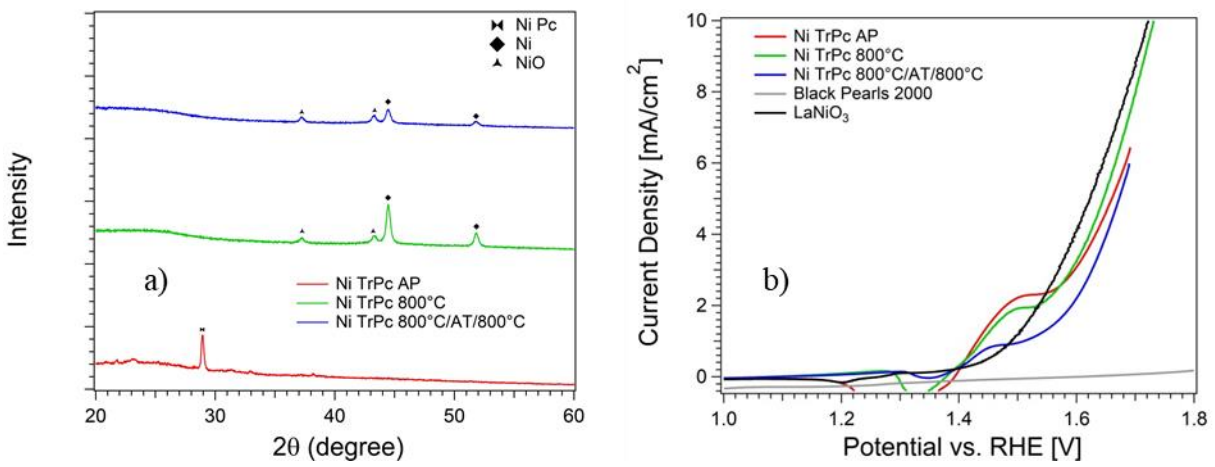

Figure 2.8: a) XRD spectra and b) RDE for Ni TrPc catalyst in as prepared, after heat treatment, and after acid treatment. N_2 saturated 0.1M KOH, 1600rpm rotation speed, 10mV/s scan rate, Hg/HgO reference electrode, gold wire counter electrode.

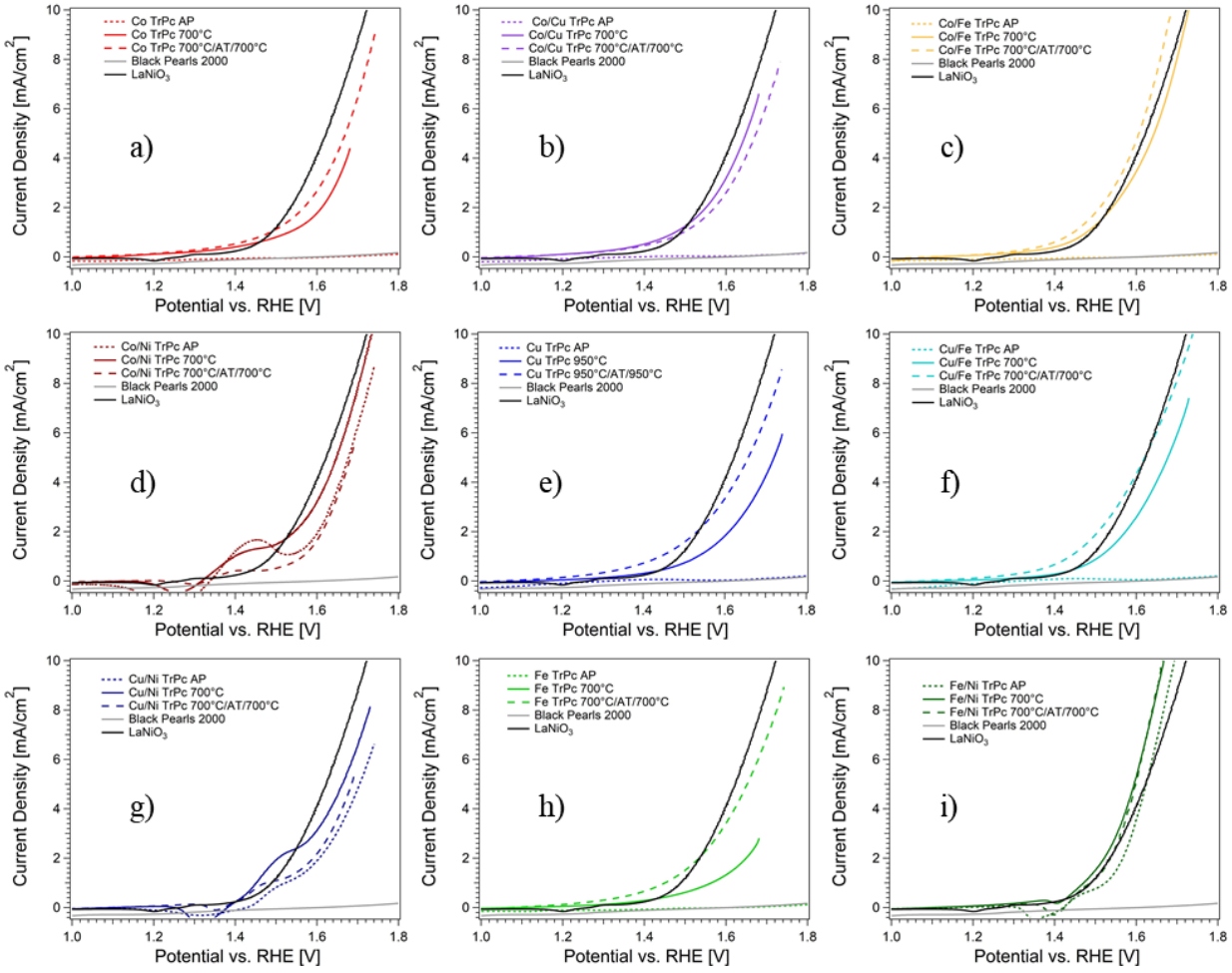

Figure 2.9: RDE plots of a) Co, b) Co/Cu, c) Co/Fe, d) Co/Ni, e) Cu, f) Cu/Fe, g) Cu/Ni, h) Fe, and i) Fe/Ni catalysts as prepared, after the initial pyrolysis, and after the acid treatment followed by the second pyrolysis. N_2 saturated 0.1 M KOH, 1600 rpm rotation speed, 10 mV/s scan rate, Hg/HgO reference electrode, gold wire counter electrode.

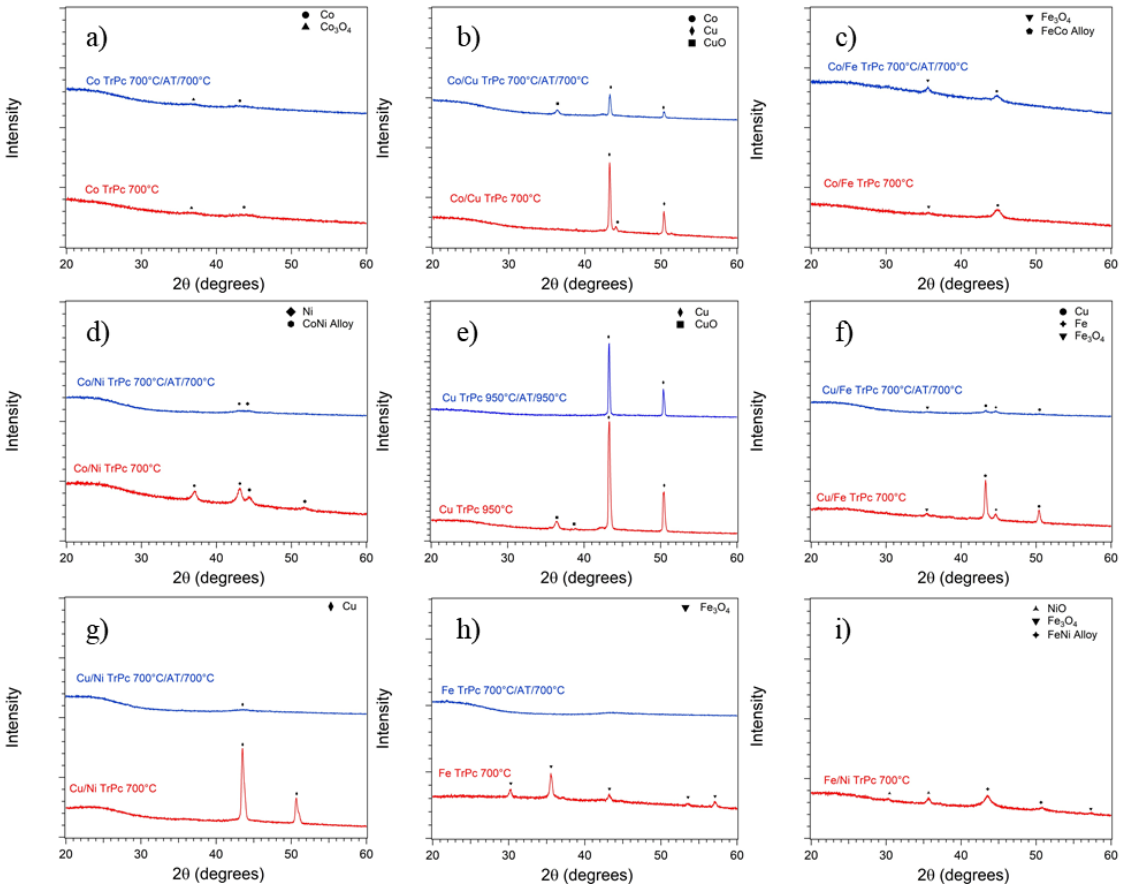

Figure 2.10: XRD spectra of the a) Co, b) Co/Cu, c) Co/Fe, d) Co/Ni, e) Cu, f) Cu/Fe, g) Cu/Ni, h) Fe, and i) Fe/Ni catalysts before and after the acid treatment.

Table 2.2: RDE and physical parameters for Me TrPc HT catalysts. For electrochemical measurements: Oxygen Saturated 0.1 M KOH with 1600 rpm electrode rotation speed with Hg/HgO reference electrode and gold counter electrode.

Metal	Treatment Temp (°C)	$E_{1/2}$ (ORR) [V]	$E_{2.5mA/cm2}$ (OER) [V]	OER Tafel	BET (m^2/g)
Single Metals					
Co	700	0.838	1.633	122.2	755
Cu	950	0.821	1.637	194.2	782
Fe	700	0.784	1.673	246.4	891
Ni	800	0.728	1.569	120.1	792
Bi-Metallic					
Co/Cu	800	0.833	1.575	157.3	668
Co/Fe	700	0.822	1.564	101.3	823
Co/Ni	700	0.789	1.571	121.6	774
Cu/Fe	700	0.831	1.597	186.2	792
Cu/Ni	700	0.779	1.562	179.9	716
Fe/Ni	700	0.779	1.538	79.6	1574

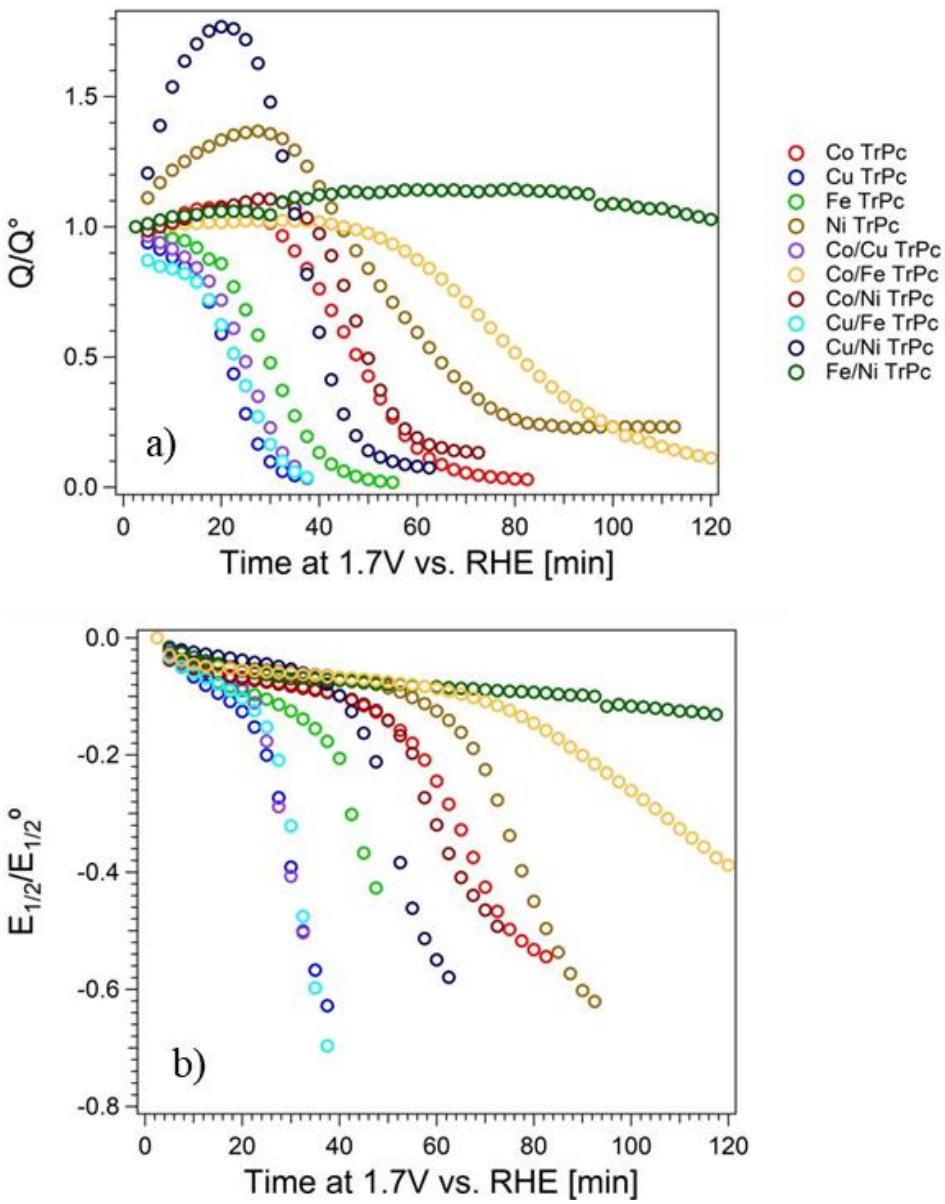

Figure 2.11: a) change in charge passed during the potential hold at 1.7 V. b) change in the ORR half wave potential over time held at 1.7 V.

The Cu containing catalysts were the least stable towards high potentials. For the Cu, Co/Cu, Cu/Fe catalysts, the OER activity was completely diminished after 40 min of holding at 1.7 V and there was a significant negative shift in the ORR half-wave potential. The exception was Cu/Ni TrPc 700°C which showed a large initial increase in current but ultimately degraded faster than the Ni TrPc 700°C. The Co/Fe TrPc 700°C and Fe/Ni TrPc 700°C catalyst had significantly higher stabilities than any of the respective metals indicating that iron stabilizes the catalyst. The only catalyst which showed any appreciable activity after 80 min were Ni TrPc 800°C, Co/Fe TrPc 700°C, and Fe/Ni TrPc 700°C. The Ni TrPc 800°C appeared to stabilize at ~20% initial OER activity however the half-wave potential for ORR continuously declined. The Co/Fe TrPc 700°C lasted significantly longer than most other catalysts but did not appear to stabilize. The Fe/Ni TrPc 700°C did not lose any OER activity during the test and showed a relatively small 0.1 V negative shift in the ORR half-wave potential after 2 hr at 1.7 V vs. RHE.

The stability of the Co/Fe TrPc 700°C and Fe/Ni TrPc 700°C were compared to other non-precious metals bifunctional catalysts commonly suggested for use in metal air batteries. Catalysts were cycled between 0 and 1.7 V vs. RHE 200 times; the results are shown in Figure 2.12.

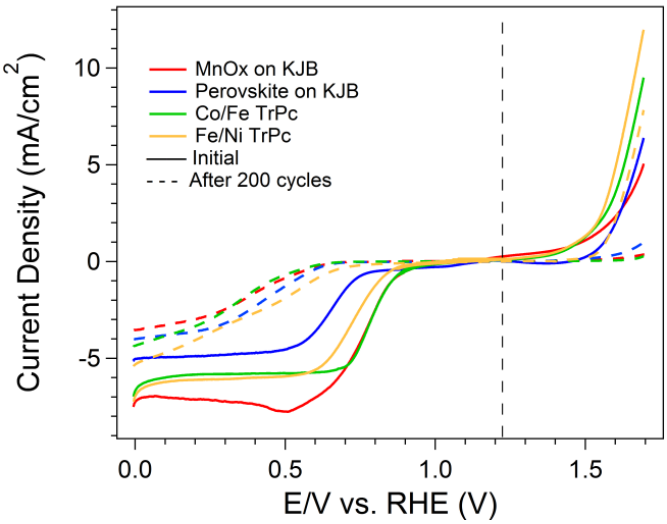

Figure 2.12: Stability of TrPc catalysts compared to other bifunctional NPM oxygen catalysts. Oxygen Saturated 0.1 M KOH with 10 mV/s scan rate, 1600 rpm electrode rotation speed, Hg/HgO reference electrode, and gold counter electrode.

Manganese oxide and a commercial perovskite were chosen as comparison. Both materials were supported on a high surface area carbon to more directly compare with the TrPc catalysts. At the onset, the Co/Fe TrPc 700°C and the MnOx catalyst had similar ORR activity while the Fe/Ni TrPc 700°C and perovskite had ca. 0.08 V & 0.15 V, respectively, higher overpotential. The Fe/Ni TrPc 700°C and Co/Fe TrPc 700°C catalysts had the best OER activity initially.

After cycling the oxygen reduction activity was severely diminished in all cases. The ORR activity of the cycled perovskite and manganese oxide was similar to that of the respective catalysts supported on low surface area carbon supports, such as acetylene black or graphite. This indicates that the amorphous regions of the carbon supports were degraded. The OER activity of the Co/Fe TrPc 700°C, perovskite, and manganese oxide were also severely decreased. The OER activity of the Fe/Ni TrPc 700°C was diminished after cycling; however, it still remained more active than either of the metal oxides were initially.

ZAB Testing

The most promising catalyst, Fe/Ni TrPc 700°C was tested in a full zinc-air battery cell and compared to manganese oxide and a perovskite. All cells used a zinc foil as the negative electrode and standard catalyst loadings of 1 mg/cm^2. Figure 2.13a shows the whole cell polarization during charging and discharging for the ZABs. In order to study and compare the polarizations of the air electrode, a reference electrode was included in the cell. The separated cathode polarization is shown in Figure 2.13b.

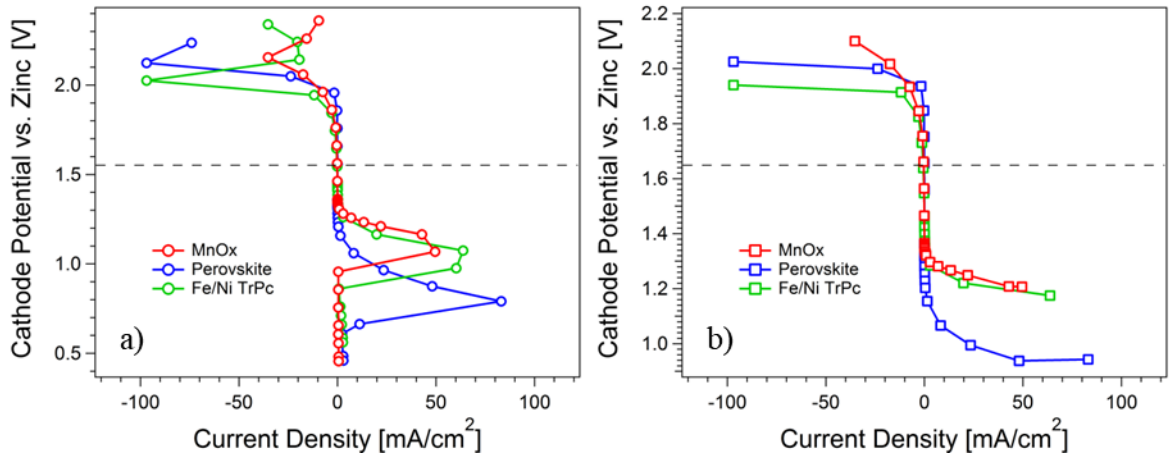

Figure 2.13: a) Full cell polarization of zinc-air battery. b) Positive (air) electrode polarization only. Testing Conditions: 200 ml/min of 100%RH UHP O_2 gas flow, 30°C cell temperature, ambient pressure, Zn foil anode.

During the discharge, all cells reached a peak current between 50-100 mA/cm^2 after which no more current could be drawn from the cell. A similar peak was observed on the charge step. This is most likely due to the low surface area of the zinc plate electrode and well known issues of the passivation of zinc electrodes with zinc oxide layers[97]. Various strategies have been suggested to avoid this passivation, such as limiting the maximum current density, creating 3D zinc structures, or flowing negative electrode systems[71,97–99]. However, these are beyond the scope of this work. Issues with the zinc foil electrode also prevented longer-term stability testing of the catalysts in situ.

In order to study and compare the polarizations of the air electrode, a reference electrode was included in the cell, as shown in Figure 2.13b. The Fe/Ni TrPc 700°C and the manganese oxide had similar activity during discharge, whereas the perovskite had a much higher overpotential. During the charge step, the Fe/Ni TrPc 700°C was superior to both of the metal oxide catalysts. Cell cycling was attempted to probe the stability of the catalysts in cell. However, issues arising from the zinc electrode resulted in cell death before any substantial degradation in air electrode behavior was observed.

The effect of catalyst loading on cell performance was studied for the Fe/Ni TrPc catalyst. The results are shown in Figure 2.14, and the increased loading significantly improved the catalyst performance. However, at the highest catalysts loading the onset of charging current below 1.65 V indicates a non-trivial carbon corrosion current.

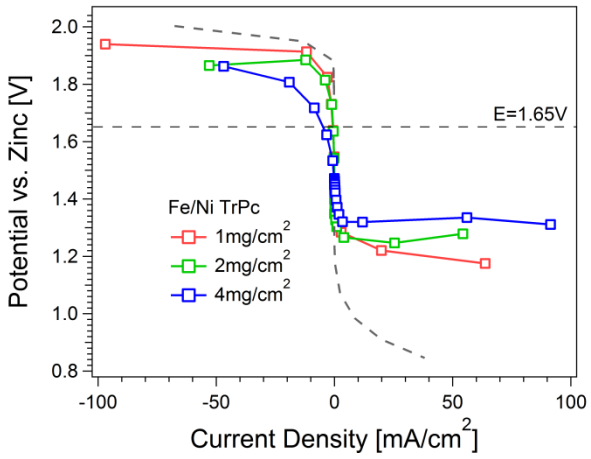

Figure 2.14: Effect of Fe/Ni TrPc loading on ZAB air electrode performance. Dashed lines represent a commercial perovskite material (1 mg/cm^2) for comparison. Testing Conditions: 200 ml/min of 100%RH UHP O_2 gas flow, 30°C cell temperature, ambient pressure, Zn foil anode.

Comparing Oxygen Evolution and Carbon Corrosion

The rotating ring disk electrode technique was utilized in order to distinguish between current from oxygen evolution and carbon corrosion. In this case the OER was carried out in nitrogen saturate electrolyte and the potential of the platinum ring electrode was held at ~0.4V vs. RHE to reduce the evolved oxygen. The collection efficiency of the ring electrode was measured with an unsupported perovskite catalyst. In this case, all of the measured current at this disk is from oxygen evolution. The collection efficiency was determined to be 20%, which is well below the value of 39.1% measured using the potassium ferro/ferri cyanide couple. It is probable that oxygen produced from the OER quickly supersaturates the solution, leading to the formation of bubbles which are not captured at the ring electrode. Therefore, the potential range was adjusted for each catalyst to prevent current densities above ~5 mA/cm^2. The experiment was conducted with Ketjen Black, Acetylene Black, and graphite. In all cases there was no observed ring current, suggesting that the observed activity can all be attributed to carbon corrosion.

Figure 2.15a shows the disk and ring currents observed from the manganese oxide catalyst supported on acetylene black, and Figure 2.15b shows the processed data indicating the contribution to the overall current from the oxygen evolution reaction. The peak current diminishes with each subsequent cycle, while the OER current remains relatively stable, indicating that less carbon corrodes with each cycle. As can be seen in the Figure 2.15a, there is an increase in the double layer capacitance of the catalyst layer between 0.8-1 V with cycling. This suggests the electrochemically active surface area is increasing as carbon corrosion increases the surface roughness or hydrophilicity.

The relative proportion of calculated OER current to measured current for several catalysts are given in Table 2.3. As expected, the OER current for the manganese oxide on the high surface area Ketjen Black was significantly lower than the observed current, indicating a large amount of carbon corrosion. In contrast, the manganese oxide on Acetylene Black had a significantly higher OER contribution. The perovskite catalyst was supported on the more stable carbons, and this electrode had a lower carbon content than either of the manganese oxide electrodes. As a result, all of the observed current was attributed to the OER. ZAB cell testing conducted using perovskite catalysts with the same carbon supports and the same perovskite to support ratios has qualitatively indicated carbon corrosion is still an issue in situ.

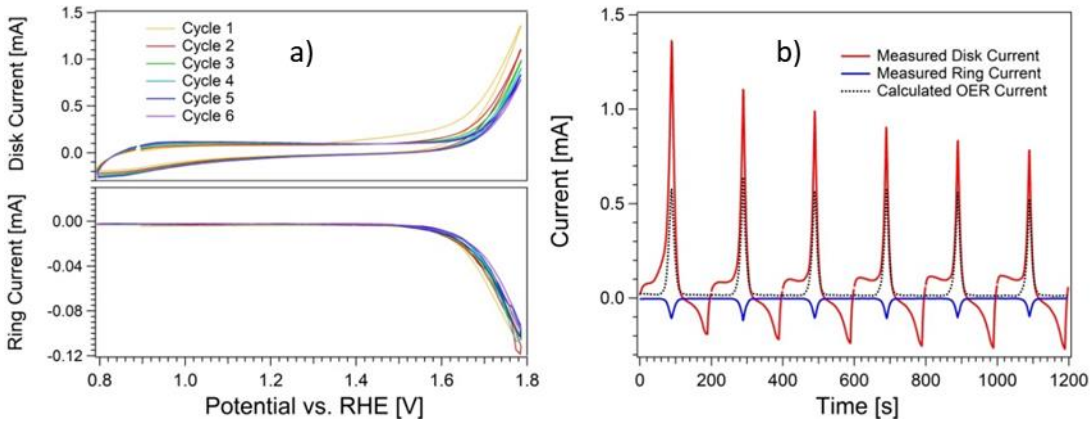

Figure 2.15:a) I vs. E plots for ring and disk electrodes with the 30%MnOx/AB catalysts. b) I vs time plot constructed from a) showing the measured disk and ring current and the calculated OER current. Nitrogen Saturated 0.1 M KOH with 10 mV/s scan rate, 1600 rpm electrode rotation speed, Hg/HgO reference electrode, and gold counter electrode.

Table 2.3: Calculated OER currents for several supported catalysts at ~1mA/cm^2 observed current.

Catalyst	Potential [V]	Measured Current [mA/cm^2]	OER Current [mA/cm^2]	% OER Current
75%LaNiO3+AB+Graphite	1.685	0.965	0.978	101.3
30%MnOx/AB	1.695	1.024	0.744	72.6
30%MnOx/KJB	1.665	1.003	0.163	16.2
NiFe TrPc 700°C	1.556	0.921	0.138	60.4

Conclusion

Oxygen reduction and evolution on metal oxide materials, e.ge perovskites and manganese oxide, was evaluated for use in a rechargeable zinc-air battery. The materials studied were common in the literature. Even in the most active catalysts there was a ~1 V discrepancy between charging and discharging voltages, limiting the battery efficiency.

Earlier work characterized the oxygen reduction behavior and activity of a family of PGM-free catalysts synthesized using an array of different metals or metal combinations. In the course of this work it was observed that some materials demonstrated oxygen evolution activity as well.

In pursuit of a more active bifunctional catalyst behavior of these novel non-precious metal catalysts for the oxygen reduction and evolution reactions in alkaline environments was studied. The catalytic activity and stability was probed using rotating disk electrode electrochemical methods and compared to manganese oxide and perovskite. The best performing catalyst was tested in a rechargeable zinc-air battery and compared with the metal oxide catalysts.

The catalyst in this work compares favorably in both stability and activity to the metal oxide catalysts, however it appears to be limited to the same minimum OER overpotential as all catalysts. Furthermore the observed corrosion of even highly graphitic, stable carbon supports in zinc-air batteries indicates real challenges facing the development of rechargeable ZABs. Therefore, future work on cathodes for rechargeable ZABs should focus on radically different chemistries to achieve higher efficiencies.

Chapter 3: Reversible Two Electron Oxygen Catalyst

Introduction

As discussed in the previous section, the limitations of bifunctional oxygen catalysts for metal air batteries are well known. Metal oxide materials suffer from poor electrical conductivity and large particle sizes (low surface area) and therefore require a conductive support, of which carbonaceous materials are the most promising. However, this leads to issues with carbon corrosion at the high potentials of oxygen evolution. The materials are also fundamentally limited to a large discrepancy in the charging and discharging voltages by the by the scaling factors related to intermediate specious adsorption enthalpy.

An attractive option then is to forgo the 4 electron oxygen reduction reaction in favor of the two electron pathway. These two reactions are:

$$O_2 + 2H_2O + 4e^- \rightarrow 4OH^- \qquad 1.23\text{V vs. RHE} \qquad [3.1]$$

$$O_2 + H_2O + 2e^- \rightarrow OH^- + OOH^- \qquad 0.84\text{V vs. RHE} \qquad [3.2]$$

Even though the 4 electron process is nominally at 1.23 V, the large overpotentials required mean that even for the most active precious metal catalysts the onset potential in RDE experiments is typically below 1 V. Therefore, switching to the 2 electron pathway would not be expected to reduce the power density of the cell on discharge significantly as long as low overpotentials can be achieved.

The main advantage of switching to a two electron pathway is in the charge step. Even non-precious metal catalysts such as nickel are known to be active for peroxide oxidation below 1 V. Therefore a zinc-peroxide battery (ZPB) could operate with a 0.2 V discrepancy between charge and discharge as opposed to a 1+ V discrepancy for ZABs. The low potential for peroxide oxidation is also below the potentials where carbon corrosion would be expected to occur, meaning carbon based gas diffusion layers and catalyst supports may be used.

This approach is predicated on the use of a catalyst which is highly selective towards the 2 electron pathway. Many non-precious metal catalysts produce a significant amount of peroxide; however it is imperative that the catalyst proceeds only through the 2 electron pathway. This is because any current which goes through the 4 electron pathway on discharge will not produce peroxide and will require charging the battery through the 4 electron pathway to reach 100% state of charge; i.e. charging at 1.6+ V vs. RHE.

Some work with gold catalysts in our lab led to the discovery of a reversible 2 electron pathway catalysts several years ago. This catalyst was a cobalt salen (Co Salen) complex adsorbed onto the surface of a gold electrode. It was not clear whether the Co Salen was responsible for the oxygen reduction to peroxide, or if it modified the surface structure of the gold electrode, leading to the 4 electron pathway.

Experimental

Catalyst Synthesis

Catalysts were synthesized by a collaborating researcher.

Rotating Disk Electrode and Cyclic Voltammetry

Half-cell experiments were carried out using a multi-channel VMP3 potentiostat from Bio-Logic, a Pine instruments MSR rotator and RDE electrode with a 0.1963 cm^2 glassy carbon (GC) disk. A gold wire mounted in a glass tube with a frit was used as the counter electrode. A Radiometer Analytical XR400 Hg/HgO reference electrode was used.

The potential of the reference electrode versus the reversible hydrogen electrode (RHE) was determined by saturating the 0.1 M NaOH with hydrogen and measuring the OCV with a multi-crystalline Pt working electrode. Ultra-high purity (UHP) gasses from Airgas Co. were used for each experiment.

Inks were prepared by dispersing 5 mg of catalyst into 0.5 g methanol. The volume of ink required to achieve the desired 200 $\mu g/cm^2$ loading was determined by depositing aliquots of the inks onto a pre-weighed piece of aluminum foil and allowed to dry then weighing with a Mettler Toledo XP2U Ultra Micro Balance. The ink was then solution-casted onto the GC disk electrode. Catalysts were tested in aqueous 1 M NaOH electrolyte. For each experiment, the electrolyte was de-aerated for at least 30 min with nitrogen. Cyclic voltammograms were then collected between 0.1 and 1.3 V vs. RHE with a 10 mV/s scan rate for background correction. This procedure was repeated in O_2 saturated electrolyte without rotation and while rotating the electrode at 1600 rpm. The uncompensated solution resistance was then measured using the Potentio-Electrochemical Impedance Spectroscopy (PEIS) technique. Cyclic voltammograms were collected at different scan rates typically between 0.6 and 1.1 V. In some cases the potential bounds were expanded to observe the relevant reactions.

Symmetric Cell Electrode Preparation

Catalyst inks were prepared by dispersing the 20 mg of the catalyst in enough 4 g of isopropanol to form a 0.5 wt% solution. ~95 mg of Tokuyama AS4 ionomer solution (5 wt%) and ~190 mg of polytetrafluoroethylene (PTFE) solution (5 wt%) were then added to achieve a

58%/28%/14% ratio of catalyst/PTFE/AS4. The catalyst inks were sonicated for at least 30 min prior to spraying. The catalyst layers were spray painted onto Sigracet 29BC gas diffusion layers (GDLs) to achieve the desired loading of 1 $mg_{catalyst}/cm^2$.

Membrane Electrode Assembly

Membrane Electrode Assemblies (MEAs) were prepared by stacking the electrodes with an in-house prepared anion exchange membrane saturated with a 1M NaOH solution. In some cases a gold-coated nickel foam with a Co Salen film electropolymerized over the surface was included between the membrane and GDLs for separate liquid flow

Symmetric Cell Testing

The MEAs were placed in a 5 cm^2 Fuel Cell Technologies cell hardware with serpentine flow channels. A palladium (Pd) coated Cu wire was included as a pseudo-reference electrode. The cell temperature, relative humidity (RH) and gas flow rates were controlled with a Fuel Cell Technologies test station. The cells were tested at room temp with 200 ml/min of 100% RH oxygen or air gas flows and ambient pressure. Unless otherwise specified. In some cases a liquid 1 M NaOH solution containing hydrogen peroxide was flowed at a constant rate of 60 ml/min.

Results and Discussion

Influence of the Electrode Surface

Initial testing was previously conducted with a polycrystalline gold electrode with the organometallic complex adsorbed on the surface. Scaling the electrode up to sizes of commercial interest (>1 m^2) would likely be too expensive, given the cost of gold. Therefore it was important to recreate the recreate the catalyst on the nano-scale using cobalt salen attached to the surface of gold nanoparticles.

The catalytic center for the observed reversible 2 electron process was initially unknown. Tests were conducted to determine if the reversible activity was a result of modifications to the gold surface, or if the cobalt salen ligand was the catalytic center. In this experiment, a Co Salen ligand was attached to either gold or iron nanoparticles immobilized on a carbon support, or directly attached to the carbon support with no metal. Cyclic voltammograms for these catalysts are shown in Figure 3.1. The anodic peak at ~0.85 V vs. RHE is the oxidation of hydrogen peroxide back to oxygen. The fact that it is present in each sample indicates that the Co salen ligand is the catalytic center. Therefore, the catalyst could be produced by immobilizing the Co salen on the surface of a high surface area carbon black, avoiding the use of high-cost gold.

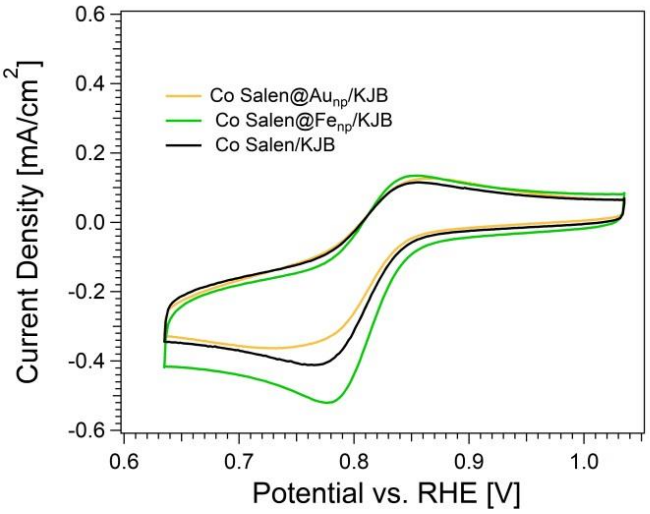

Figure 3.1: Cyclic voltammograms for cobalt salen supported immobilized on different surfaces on. Oxygen saturated 0.1 M NaOH, 10 mV/s scan rate, Hg/HgO reference electrode, and gold counter electrode.

Influence of the Macrocycle and Metal

Further experiments were conducted to determine if the reversible behavior was unique to the Co Salen ligand. The influence of the metal center in the macrocycle was investigated by collecting CVs in 1M NaOH solutions containing 2 mM cobalt, iron, nickel, and copper salen. The results are given in Figure 3.2. The cobalt salen complex demonstrated reversible behavior, as expected. The copper salen had appeared to both generate and oxidize peroxide; however the reactions did not appear as reversible as with the cobalt complex. Neither the iron nor the nickel had a peroxide oxidation peak, indicating that these complexes either don't interact with the gold electrode, are incapable of oxidizing peroxide, or proceed through the 4 electron pathway.

To investigate whether the 2 electron reaction is unique to the salen ligand, experiments were conducted in solutions containing other macrocycles, such as phthalocyanine (Pc). A trend was observed for the Fe Pc complex in which the lower cathodic potential limit was set, the more reversible the reaction appeared. This behavior appeared unique to this particular complex and was observed for other Pc or Salen complexes. As can be seen in Figure 3.3, only a modest peroxide oxidation peak is observed when the electrode is cycled within the standard window, but as the electrode is allowed to reach lower potentials, both the peroxide oxidation and oxygen reduction peaks intensify and move become more reversible. This indicates that the Fe Pc catalyst requires lower potentials to be activated. This would be impractical for use in a cell, where a constant potential close to the reversible potential is desired.

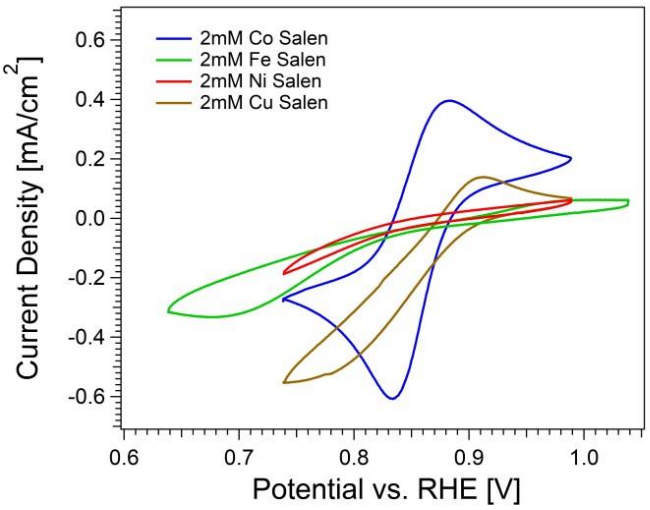

Figure 3.2: Cyclic voltammograms of gold electrode in 0.1 M NaOH containing different salen compounds. Oxygen saturated 0.1 M NaOH, 100 mV/s scan rate, Hg/HgO reference electrode, and gold counter electrode.

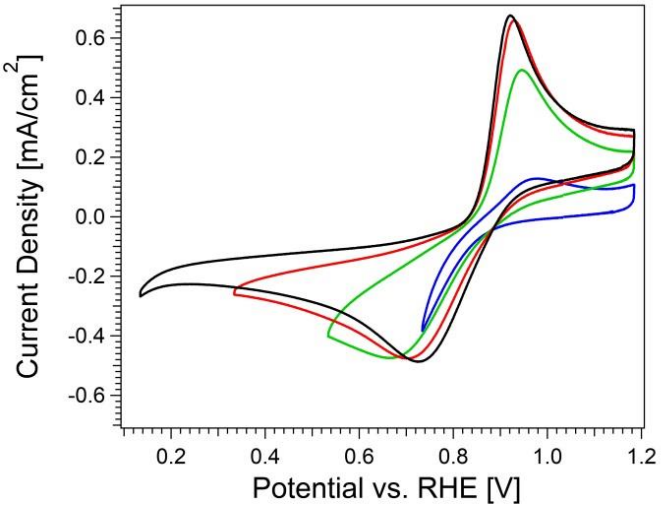

Figure 3.3: Cyclic voltammograms of gold electrode in 0.1 M NaOH containing 2 mM iron phthalocyanine with different cathodic potential limits. Oxygen saturated 0.1 M NaOH, 100 mV/s scan rate, Hg/HgO reference electrode, and gold counter electrode.

The results for the other phthalocyanine complexes are shown in Figure 3.4 and compared to Co salen. The Co Pc complex is less reversible than the Co Salen complex. Conversely, each of the other metals appears to be more reversible with the than their respective Salen ligands.

Additionally, the cobalt salen and phthalocyanine complexes were incorporated into a catalyst with gold nanoparticles and supported on a high surface area carbon. This allowed for a comparison in a more realistic catalyst formulation. The results are illustrated in Figure 3.5. It is immediately evident that the Co Pc is not reversible and demonstrates no peroxide oxidation peak. The Co salen containing catalyst does show a peroxide oxidation peak, but it is not as reversible as with the gold disk electrode.

In-Situ Electrode Testing

With the reversible 2 electron catalyst proven in RDE setting, experiments were conducted to incorporate the catalyst into a full cell type electrode. Due to ongoing issues with the long-term cyclability of zinc electrodes, the bulk of this work focused on a symmetric cell environment. Initial tests were conducted using a standard fuel cell set-up with two electrodes separated by a membrane, each with a humidified gas stream delivered to the catalyst layer through a gas diffusion layer. Several different catalyst formulations and electrode structures were investigated to develop a reversible oxygen full cell electrode.

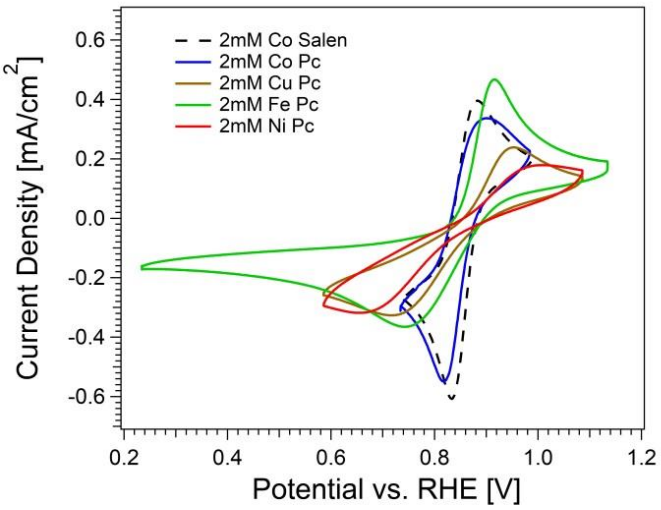

Figure 3.4: Cyclic voltammograms of gold electrode in 0.1 M NaOH containing different phthalocyanine compounds. Oxygen saturated 0.1 M NaOH, 100 mV/s scan rate, Hg/HgO reference electrode, and gold counter electrode.

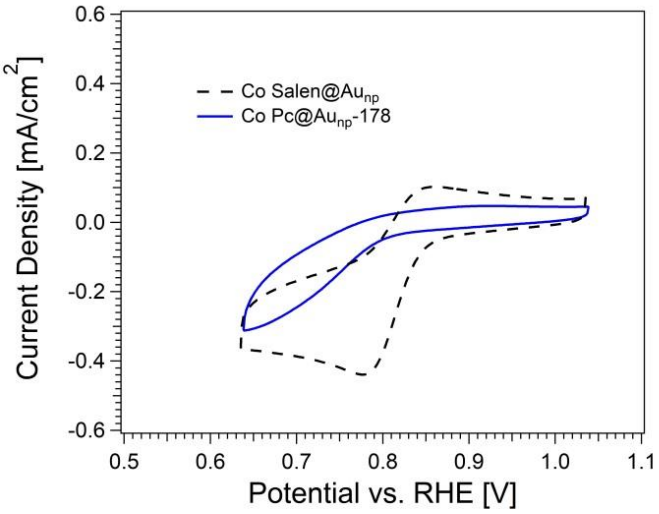

Figure 3.5: Cyclic voltammograms Co Salen and Pc ligands immobilized on a gold nanoparticle catalyst. Oxygen saturated 0.1 M NaOH, 10 mV/s scan rate, Hg/HgO reference electrode, and gold counter electrode.

The first method of preparing electrodes involved galvanostatic replacement nickel in a porous nickel foam with gold followed by electropolymerization of commercial cobalt salen. This set up will be referred to as $AuCoS_E@Ni_{foam}$, where the E subscript denotes the electropolymeriataion process. Figure 3.6a show CVs of this electrode in an RDE setup, confirming the reversibility of the electrode. Polarization curves from the symmetric cell are shown in Figure 3.6b. The dashed lines represent 90% voltage efficiency. Both reactions have poor voltage efficiencies and the overall cell has a low current density. The cathode polarization does reaches well below 0 V and the increase in current at ca. -0.2 V could be from hydrogen evolution. The high potential at the anode (1.6+ V) indicates the anodic reaction is oxygen evolution from hydroxide rather than peroxide. This indicates that there is not sufficient delivery of hydrogen peroxide to the anode through the membrane.

In order to better study the electrode behavior, a pseudo-symmetric cell was used. In this case the same setup detailed above was used for the oxygen reduction electrode, and a flowing 1 M NaOH solution containing 0.5 M H_2O_2 was used at the oxygen evolution electrode. Figure 3.7 shows the performance of this cell compared to the previous test. The oxygen evolution electrode in this setup is significantly improved. In order to implement the gains of the flowing anode, a full cell battery or fuel cell will be required to either use a dual phase liquid and gas flow at the air electrode, or use separate electrodes for the reduction and evolution reactions.

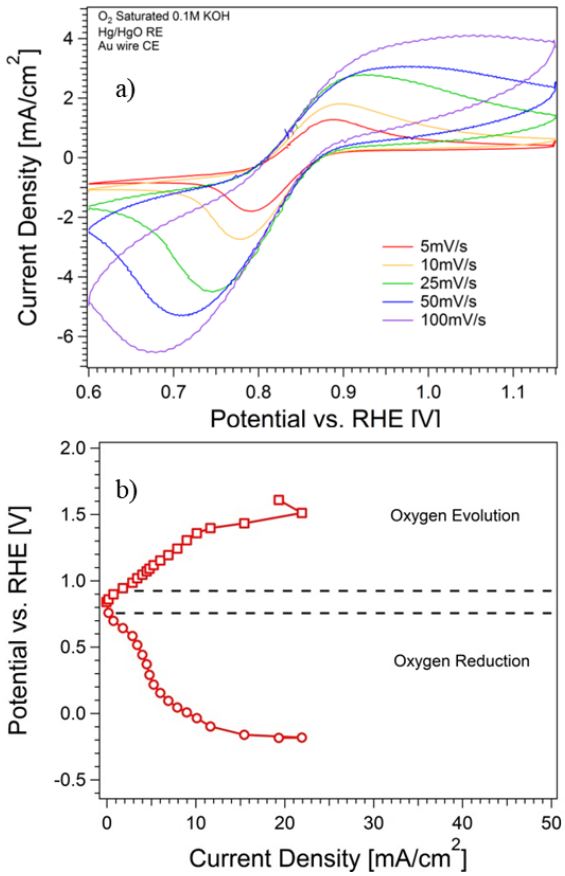

Figure 3.6: a) Cyclic voltammograms of electrode with cobalt salen electropolymerized on gold coated nickel foam in a half-cell environment. b) Polarization curves for oxygen reduction and evolution using the same electrode in a symmetric cell with 100 ml/min oxygen flow rate, room temperature, with CLAM membrane saturated in 1 M KOH/0.5 M H_2O_2 electrolyte.

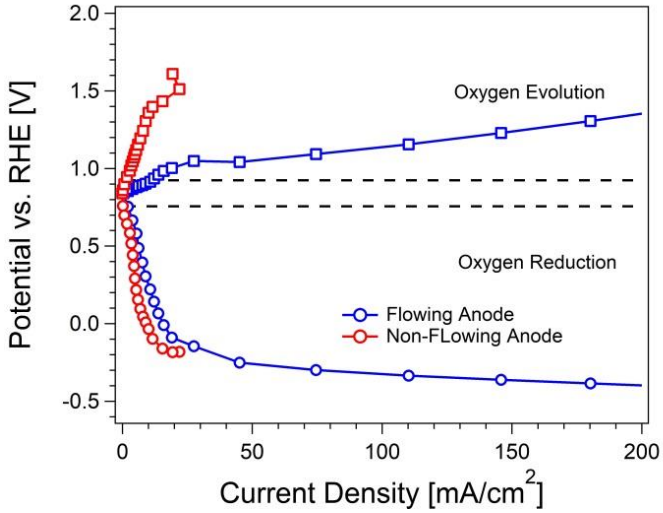

Figure 3.7: Polarization curves for oxygen reduction and evolution in a symmetric cell using $AuCoS_E@Ni_{foam}$ electrodes with and without liquid solution flow at the anode. Test Conditions: 200 ml/min oxygen flow or 60 ml/min 1 M NaOH/0.5 M H_2O_2 electrolyte flow, room temperature.

The polarization of the oxygen reduction electrode was similar to the initial test. This would be expected since there was no change in structure or catalysts at this electrode. The poor performance could be attributed to several factors. First, nickel foams have very low surface area compared to standard fuel cell gas diffusion layers; therefore the poor performance could be attributed to insufficient catalytic sites. Second, the nickel foam is significantly more hydrophilic than standard GDLs, indicating the electrode may be flooded, preventing a sufficient amount of oxygen from reaching the catalsyt. Several methods of increasing ORR performance in symmetric cells were attempted.

Gold nanoparticles (Au_{np}) were spray painted onto the microporous layer of a Sigracet 29BC gas diffusion electrode. The electrode was then submerged in an acetonitrile solution containing commercial cobalt salen which was electrodeposited on the surface of the electrode. This type of electrode is refered to as $Au_{np}CoS_E$@29BC. The electrodes were incorporated into a symmetric cell with a hydroxide/peroxide solution flowing at the anode. The polarization curves are shown in Figure 3.8. The oxidation reduction polarization is dramatically reduces using this type of electrode. The oxygen evolution polarization closely matches the $AuCoS_E@Ni_{foam}$ electrode until ~30 mA/cm2 at which point the overpotential increases sharply. This indicates that the $Au_{np}CoS_E$@29BC electrode limits the mass transport of electrolyte.

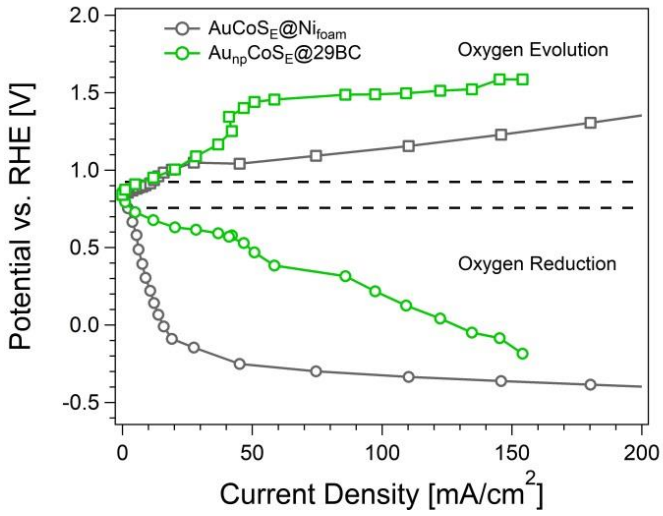

Figure 3.8: Symmetric cell polarization curves for $Au_{np}CoS_E$@29BC electrodes compared to the initial tests with $AuCoS_E@Ni_{foam}$. Test Conditions: 60 ml/min 1 M NaOH/0.5 M H_2O_2 liquid flow at anode, 200 ml/min oxygen flow at cathode, room temperature.

A similar electrode was conducted with a catalyst produced in a one-pot synthesis route in which Au_{np}s were supported on carbon black the the cobalt salen was chemically polymerized over the surface. The catalyst was spray painted onto Sigracet 29BC which was incorporated into a cell. This type of electrode is refered to as $Au_{np}CoS_C$@29BC, where the C subscript denotes the chemical polymerization process. The advantage of this system is the relative ease of electrode fabrication compared to the multi-step process used for the $Au_{np}CoS_E$@29BC electrodes. The polarization curve for this cell is shown in Figure 3.9. The ORR performance of this catalyst was significantly better than the electropolymerized Au_{np}CoS@29BC electrode. Here again, the use of the GDL caused large mass transport losses for the oxygen evolution reaction.

A nanoporous gold ($_{np}$Au) film was produced by etching the silver from a 14 Karat gold leaf in concentrated nitric acid as described by Ding et al[100]. The film was supported on either gold coated Sigracet GDL or anickel foam. Cobalt salen was then electropolymerized on the electrode. This type of electrode is refered to as $_{np}AuCoS_E$@29BC or $_{np}AuCoS_E@Ni_{foam}$. The polarization curves for both methods are shown in Figure 3.10a. There is a significant increase in oxygen reduction performance when the nanoporous gold layer is added to the nickel foam. This confirms that the high overpotentials observed in th initial cell were the result of low surface area. The oxygen reduction performance of the nanoporoius gold on the GDL and Ni foam electrodes was similar at below ~30 mA/cm^2, but the GDL performance supassed the Ni foam electrode electrode was significantly higher current densities. As seen with the other GDL based electrodes, the anode performance is simiar to the Ni foam electrode until ~20 mA/cm^2, at which point the overpotential increases sharply. The performance of the Ni foam based electrode with the nanoporous gold layer had significantly lower overpotential than without, indicating low surface area may also be limmiting for the OER.

The symmetric cell testing thus far has indicated that a porous electrode with high surface area and a flowing electrolyte is optimal for oxygen evolution while the standard catalyst upported on a multi-layer GDL structure used in fuel cells is optimal for ORR. A hybid cell with the GDL electrode at the cathode and Ni Foam electrode at the anode was cunstructed. The polarization curve for this cell is shown in Figure 3.10b. This cell had the better performance of each optimized electrode. However, this would require the use of separate ORR and OER electrodes in a fuel cell or battery, which would significantly add to the cost and complexity.

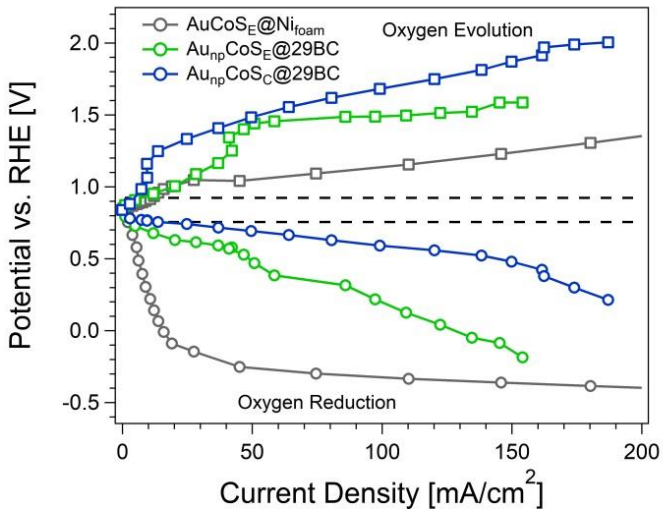

Figure 3.9: Symmetric cell polarization curves for $Au_{np}CoS_c$@29BC electrodes. The polarization of the $Au_{np}CoS_c$@29BC and $AuCoS_E$@Ni_{foam} electrodes are shown for comparison. Test Conditions: 60 ml/min 1 M NaOH/0.5 M H_2O_2 liquid flow at anode, 200 ml/min oxygen flow at cathode, room temperature.

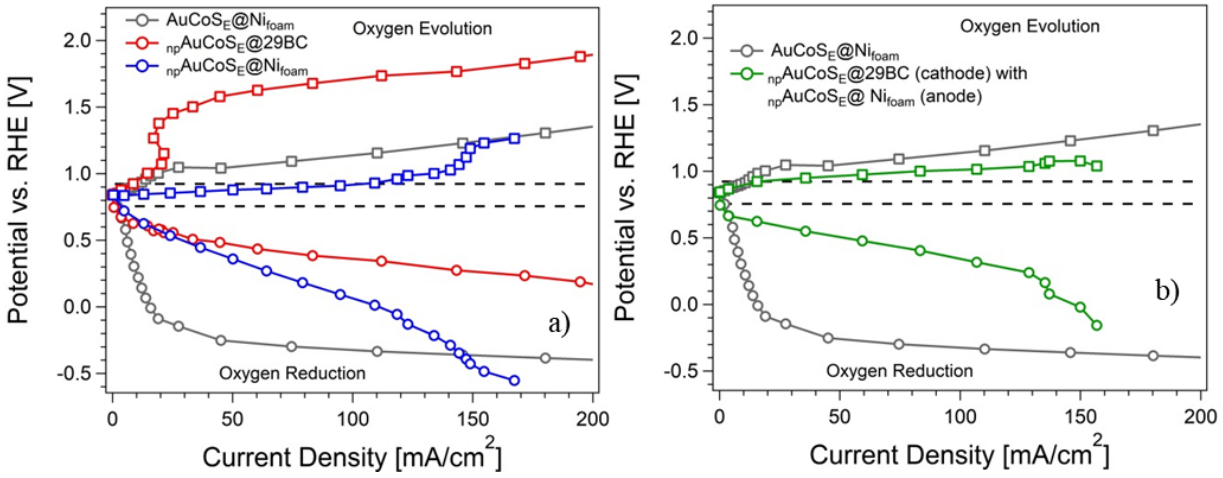

Figure 3.10: Symmetric cell polarization curves for a) $_{np}AuCoS_E$@29BC and $_{np}AuCoS_E$@Ni_{foam} and b) hybrid cell using the former at the cathode and the latter at the anode. The $AuCoS_E$@Ni_{foam} is shown for comparison. Test Conditions: 60 ml/min 1 M NaOH/0.5 M H_2O_2 liquid flow at anode, 200 ml/min oxygen flow at cathode, room temperature.

One additional method involved the depositing Au_{np}s onto the sigracet GDL and flowing an electrolyte comprised of 1M NaOH, 0.5M H2O2, and 2 mM Co Salen. The polarization curve for this cell is shown in Figure 3.11. The oxygen reduction performance was the best of any cell tested. However, the oxygen evolution resulted only from hydroxide leading to an overpotential of ~0.8 V. Ex situ experiments showed that the presence of cobalt salen in solution makes the peroxide significantly less stable. Therefore this resulted in oxygel evolution from hydroxide.

It is clear that in order to develop the optimal electrode, it must be designed for two-phase flow. A new electrode arcitechture was constructed with this goal. A schematic of this electrode is shown in Figure 3.12a. In this system, the one-pot synthesis catalyst is coated onto a standard GDL as previously described and gas flow is delivered to the catalyst through the GDL. For the liquid flow, a $_{np}AuCoSal_E@Ni_{foam}$ electrode is placed in between the GDL and the cell membrane. Liquid electrolyte is pumped through the Ni foam and carries away the peroxide and unreacted gas from the surface of the GDL. A polarization curve for a symmetric cell with this type of electrode is shown in Figure 3.12b. The oxygen evolution performance of the multi-phase electrode is similar to the original $_{np}AuCoSal_E@Ni_{foam}$ electrode, indicating the presence of the GDL doen't effect performance. The performance of the the $Au_{np}CoSal_C@29BC$ oxygen reduction electrode is improved significantly in the multi-phase flow setup compared to the original.

With the development of a a reversible 2 electron oxygen electrode proven in symmetric cell testing, the multi-phase flow electrode was incorporated into a zinc-air batter and tested. The performance of the cell is shown in Figure 3.13 and compared to a standard zinc-air battery. Even thought the OCV of the zinc-peroxide battery is lower than the zinc-air battery (1.2 V vs. 1.4 V) the reversibility of the peroxide electrode means there is virtually no difference in discharge performance. The real advantages of the zinc-peroxide battery are evident during charging. There is a reduction of ~0.5 V in the charging overpotential at 100 mA/cm^2, at this potential carbon corrosion are not expected to be an issue.

Issue with the cyclability of the zinc electrode prevented long term stability tesing on the catalyst and electrode, so instead these experiments were conducted in a symmmetric cell. Figure 3.14 shows the cycling performance of the multi-phase flow air electrode stability during a 500 hr test. There was an initial break in period, in which the perfromance increases. After this period, the cell remains stable over the entire test.

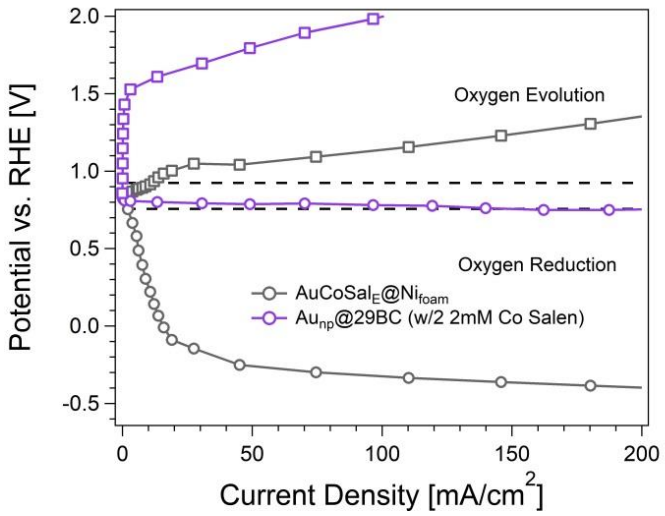

Figure 3.11: Symmetric cell polarization curves for Au_{np}@29BC electrodes compared to the initial tests with $AuCoS_E@Ni_{foam}$. Test Conditions: 60 ml/min 1 M NaOH/0.5 M H_2O_2/2 mM cobalt salen liquid flow at anode, 200 ml/min oxygen flow at cathode, room temperature.

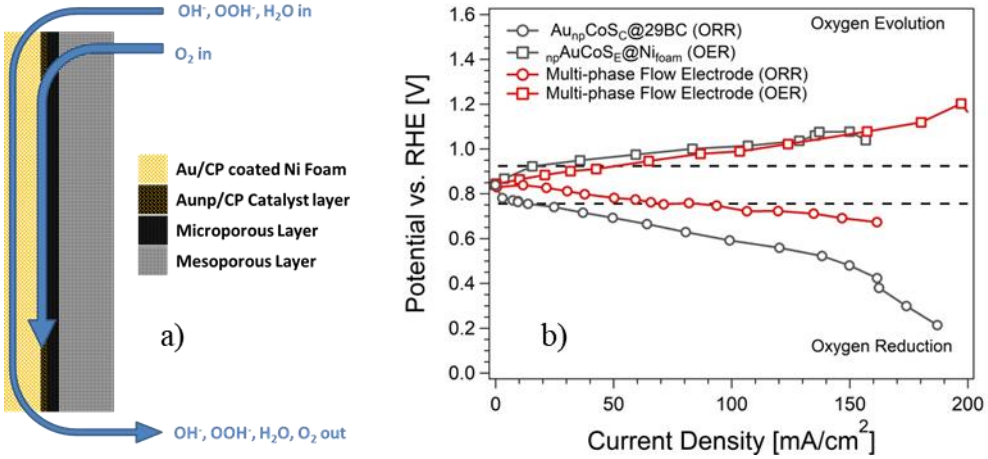

Figure 3.12: a) Diagram of the multi-phase flow electrode. b) symmetric cell polarization curves comparing the multi-phase flow electrode to the nano-porous gold electrodes. Test Conditions: mixed 100 ml/min oxygen flow and 10 ml/min 1 M NaOH/0.5 M H_2O_2 liquid flow, room temperature, 1 mg/cm^2 catalyst loading on GDL.

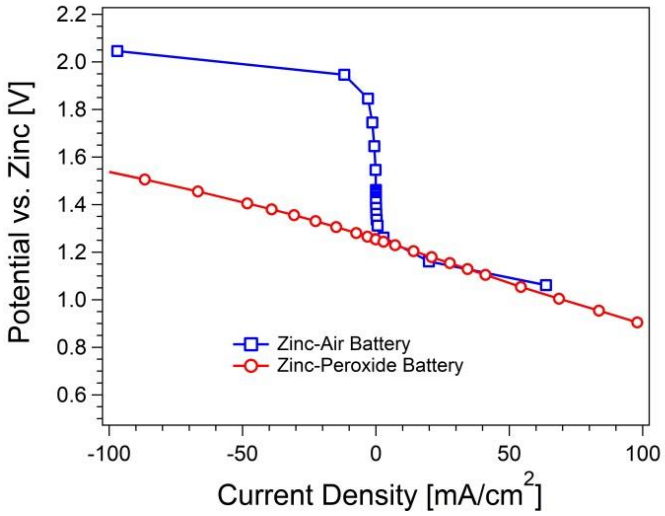

Figure 3.13: comparison of Zn-air and Zn-peroxide batteries. Zinc-air battery: 200ml/min oxygen flow, zinc foil anode, 1mg/cm2 perovskite cathode catalyst, room temperature. Zinc-peroxide battery: 100 ml/min air flow with 10 ml/min 1M NaOH/0.5M H_2O_2 mixed flow, room temperature, carbon felt GDL with electrodeposited zinc anode.

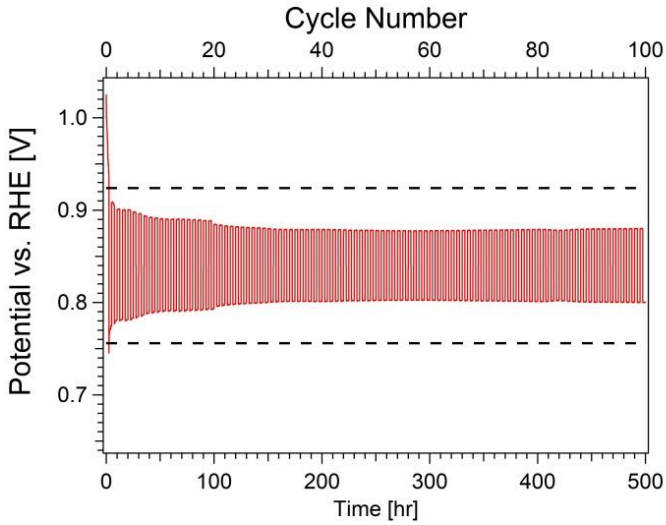

Figure 3.14: Cycling performance of the multiphase flow electrode 90% voltage efficiency is represented by the dashed black lines. Testing Conditions: 100 ml/min air flow with 10 ml/min 1M NaOH/0.5M H_2O_2 mixed flow, room temperature, 40mA/cm^2 current density.

Conclusions

The work of a previous graduate student was continued on a reversible, two-electron oxygen catalyst. The cobalt salen was determined to be the active site for the reaction. Cyclic voltammetry was conducted using a gold electrode in alkaline electrolytes containing various combinations of common metals (Co, Fe, Ni, Cu) and macrocycle ligands (Salen, Pthalocyanine) to determine if the reversible behavior was unique to Co Salen.

The cobalt containing ligands were the most promissing and were incorporated into nano-scale catalysts by attaching to the surface of gold particles on a conductive carbon black support. In this case it was shown that Co Salen was far superrior to the scale down catalysts.

The Co Salen catalyst was then used in symmetric cell testing by coating on to a standard fuell cell gas diffusion layer. Initial test revealed significantly higher overpotentials than expected for both oxygen reduction to peroxide and oxygen evolution from peroxide. Through various tests it was determined that the optimal electrode structure is significantly different for these two reactions with a hydrophobic electrode prefered for the former and a porous flooded electrode prefered for the latter. A multi-phase flow electrode was created in which the gas was supplied through a GDL to the catalyst layer as is typical and liquid electrolyte flowing through a gold-coated nickel foam placed between the catalyst layer and the membrane.

A ZPB was constructed using this new air electrode architecture. Comparing the performance to that of a standard ZAB showed an impressive reduction in overpotential during cell charging, and almost no difference in discharge polarization. The electrode was found to be stable over 500 hr of testing.

Chapter 4: Hydrogen Catalysts and Electrode Structure for AEMFCs

Introduction

Anion exchange membrane fuel cells are often promoted because of the ability to replace the expensive platinum oxygen reduction catalyst with a non-precious metal alternative. However, this doesn't take into consideration the substantially slower kinetics on the other side of the cell. In acidic environments platinum is a fully reversible catalyst for hydrogen. The hydrogen oxidation reaction (HOR) polarizations are so low in PEMFCs that a reference electrode is not typically used, even with low catalyst loadings (<0.05 mg_{Pt}/cm2).

However in alkaline media, the exchange current density is two orders of magnitude below acidic[101]. This suggests that a substantially higher Pt loading will be required at AEMFC anodes to achieve the same current densities. There are several different theories on the origin of the reduced kinetics.

There have been a few reports of non-precious metal catalysts for hydrogen oxidation at high pHs, but these catalysts are impractical due to extreme sensitivity to the atmosphere[102]. As such, precious metal catalysts are the strongest candidate for use in AEMFC anodes. Therefore, it is of the utmost importance to study the hydrogen oxidation on platinum and other precious metal catalysts in alkaline environments with the aim of increasing the mass normalized activity.

Hydrogen oxidation on platinum in alkaline electrolytes is typically ascribed to a combination of mechanisms:

Tafel Reaction: $* + H_2 \leftrightharpoons 2(*H)$

Heyrovsky Reaction: $* + H_2 + OH^- \leftrightharpoons *H + H_2O + e^-$

Volmer Reaction: $*H + OH^- \leftrightharpoons H_2O + e^-$

In the Tafel-Volmer mechanism the dissociative adsorption of the hydrogen molecule is followed by subsequent Volmer electrochemical steps on each of the hydrogen atoms. A Heyrovsky-Volmer mechanism follows the electrochemical adsorption and oxidation of hydrogen molecule in one step followed by a Volmer electrochemical step on the remaining adsorbed hydrogen atom. There are two main theories and much ongoing discussion of the origin of the poor HOR activity on platinum in alkaline environments.

The hydrogen binding energy (HBE) theory posits that an increase in Pt-H bond strength at high pH inhibits the Volmer reaction[103,104]. Proponents of this mechanism cite the shift of the hydrogen under potential deposition (H-UPD) peaks to higher potentials with increasing pH.

This shift is illustrated in Figure 4.1. The observed Tafel slope of ~120 mV/decade also suggests that the first electron transfer is rate limiting. Gasteiger's team suggest that HOR on platinum in alkaline conditions proceeds through a Tafel-Volmer mechanism with the latter being rate limiting[103,104]. In this case, alloying platinum with metals which decrease the affinity for hydrogen would be expected to increase activity.

The bifunctional theory posits that the in alkaline conditions a HOR catalyst needs active sites to accommodate the adsorption of both H_2 and OH^-[105,106]. The potential of zero charge is the potential at which an electrode must be held for there to be no net charge on the surface of the catalyst. For Pt this potential is typically ~0.55 V vs. RHE and varies slightly with pH. Below this potential there is a net negative charge on the surface of the catalyst. This charge repels the hydroxide making it more difficult to move protons out of the double layer. This would be expected to affect the rate of the Heyrovsky and Volmer reactions.

HBE proponents suggest that water, not hydroxide, acts as the proton acceptor to form a hydronium ion which combines with a hydroxide to form water away from the surface of the catalysts. The bifunctional theory suggests that alloying platinum with more oxyphilic metals or the inclusion of small amounts of metal (hydr)oxide particles in the catalyst layer may improve performance.

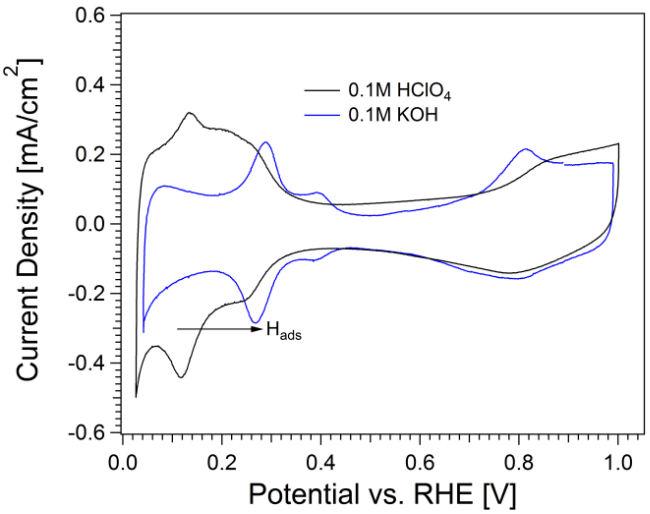

Figure 4.1: Comparison of cyclic voltammograms on a polycrystalline Pt electrode in Nitrogen saturated acid and basic electrolytes. Nitrogen saturated electrolyte, 20mV/s scan rate.

Ruthenium-platinum alloys have been shown to have significantly higher activity than platinum alone in RDEs[107,108]. There is an observed change in Tafel slope from 127 mV/decade on Pt to ~30-40 mV/decade on PtRu alloys[106–108]. This indicates a change in rate determining step from electron transfer (Volmer) to dissociating hydrogen adsorption (Tafel). There has been significant debate as to whether this is due to an electronic effect of decreasing Pt-H bond strength or an oxyphilic effect of Ru-OH surface specious providing a source of hydroxide within the double layer. A platinum-niobium catalyst studied by Mukerjee showed no shift in H-UPD peaks from Pt[106]. However, there was a significant increase in catalyst activity, which suggests that the oxyphilic niobium improves performance, supporting the bifunctional theorem.

Experimental

RDE Apparati

Rotating disk electrode (RDE) experiments were carried out using a multi-channel VMP3 potentiostat from Bio-Logic, a Pine instruments MSR rotator and RDE electrode with a 0.1963cm^2 glassy carbon disk, platinum gauze counter electrode, and either a Hg/HgO (alkaline) reference A Radiometer Analytical XR400 Hg/HgO (alkaline) or Gaskatel Hydroflex RHE (acid and alkaline) reference electrode. The potential of the Hg/HgO reference electrode versus the reversible hydrogen electrode (RHE) was determined by saturating 0.1M KOH with hydrogen and measuring the OCV with a multi-crystalline Pt working electrode. Ultra-high purity (UHP) gasses from Airgas Co. were used for each experiment.

2-propanol (IPA) LC-MS CHROMASOLV® grade was obtained from Fluka Analytical. 5wt% Nafion® perflourinated resin solution Sigma Aldrich. 5wt% AS4 ionomer solution was obtained from Tokuyama. $HClO_4$ Double Distilled GFS Chemicals) and KOH 99.99% Sigma Aldrich were used with 18.2 MΩ H_2O (Millipore) were used for all experiments. All gases used were ultra-high purity grade.

The glassy carbon electrodes were prepared by polishing with 5 micron then 0.05 micron alumina powders then rinsed and sonicated for 30s in DI water. The glassy carbon electrodes were then allowed to dry in air prior to ink deposition. The polycrystalline platinum was then sonicated in 0.1M $HClO_4$ for 30s then rinsed and immediately transferred to the RDE cell.

RDE Electrode Preparation

Inks were prepared using a by dispersing 5 mg of either 30% Pt/Vulcan XC-72 (Tanaka), 30%PtRu/ Vulcan XC-72 (1:1 Pt to Ru) (E-TEK), or an in house made catalysts in 1 g of isopropanol and ultrasonically mixing in ice water for 30 min to disperse the ink. In some cases

an ionomer was added to the ink for an 80:20 total catalyst to ionomer ratio. Aliquots of the inks were solution-cast onto the GC disk electrode to reach loadings of 20 $\mu g_{PGM}/cm^2$. The loading was determined by depositing the ink onto a piece of aluminum foil and weighting using a Mettler Toledo XP2U microbalance.

RDE Testing

Catalysts were tested in either aqueous 0.1 M KOH or 0.1 M $HClO_4$ electrolyte. For each experiment, the electrolyte was de-aerated for at least 30 min with nitrogen. The catalyst surface was first cleaned by conducting cyclic voltammetry between -0.05-1.2 V vs. RHE at a scan rate of 500 mV/s for 50-100 times. The ECSA was then determined by collecting CVs of the electrode between 0.025-1 V vs. RHE at 20 mV/s 5 times. The uncompensated solution resistance was then determined through potentio electrochemical impedance spectroscopy (PEIS) at 0.5 V vs. RHE.

The electrolyte was then purged with hydrogen for at least 30 min. The hydrogen oxidation activity was then measured by collecting CVs between -0.05 to 0.9 V vs. RHE with a 10 mV/s scan rate while static and rotating the electrode at 400, 900, 1600, and 2500 rpm.

AEMFC MEA Preparation

To prepare electrodes for the AEMFC experiments, catalyst inks were prepared by ultrasonically mixing 30 mg of the catalyst powder with 2.5 g of isopropanol and 150 mg of 5 wt. % AS4 solution (Tokuyama). A 5 cm^2 mask was placed over a piece of A201 (Tokuyama) and the ink was sprayed onto each side of the membrane until the desired catalyst loading was reached. 0.4 mg_{Pt}/cm^2 loadings were used for both the anode and cathode catalyst layers unless otherwise specified. MEAs were fabricated using the same 30%PtRu/Vulcan XC-72 (1:1 Pt to Ru) (E-TEK) or 30% Pt/Vulcan XC-72 (Tanaka) as the anode and the latter as the cathode catalyst. The catalyst coated membranes (CCMs) were stacked in the cell hardware with GDLs (Toray Paper TGP-H-090).

Reference Wire Synthesis

Due to the diminished HOR kinetics in alkaline environment, its contribution to cell overpotential cannot be neglected in AEMFCs as is typically done for PEMFCs. Therefore, in order to derive the polarization behavior of the anode and cathode separately, pseudo-reference wires were included in each cell. These wires were made by first cleaning 36 AWG copper wires with methanol, then removing the surface oxide layer by soaking in 0.1M HCl for 30s. Palladium was deposited onto the wire by soaking the cleaned wire in a solution of 10 g/L $PdCl_2$ in 0.1 M

HCl for 2 min. The wire was then rinsed and the palladium was reduced by holding the wire at -0.2 V vs. RHE in nitrogen saturated 0.1 M KOH for 2 min. The wires were then kept in 0.1 M KOH for at least 2 days prior to use in a cell. Each wire was used for only one cell test.

The potential of the reference wires was typically between 0.85-0.95 V vs. RHE. The reference wires were included in the cells by placing them in contact with the membrane in the vicinity of, but not in contact with, the cathode.

Fuel Cell Testing Hardware

Single cell experiments on the prepared MEAs were performed using a Fuel Cell Technologies test stand and single cell hardware. A Bio-Logic VSP3 potentiostat with a 10 A booster was used to collect polarization curves and PEIS. The cell has a serpentine flow channel and an active area of 5 cm^2. MEAs were positioned in the hardware and compressed to 80 inlbs of torque on the bolts. Ultra-high purity gases (Airgas) were used for all experiments.

AEMFC Testing

The cell operation temperature for all AEMFC experiments was 60°C and all gases were at 100% relative humidity (RH). The flow rate at the anode and cathode were held constant at 0.2 L/min. The cell was conditioned up to 60°C under N_2 gas flow which was then switched to H_2 and O_2 for the anode and cathode respectively. After reaching a stable OCV the electrodes were conditioned by holding the cell at 0.6V until a stable current was achieved (10-30 min). After the OCV fully recovered, a polarization curve was collected by applying increasingly negative overpotentials from OCV to 0V, once the current stabilized at each potential step PEIS measurements were made. After an initial polarization curve was collected, 2 atm of back pressure was applied to each electrode for subsequent polarization curves.

Results and Discussion

Rotating Disk Electrode Testing

A plot of the RDE polarization curves for Pt/C catalysts in hydrogen saturated basic and acidic electrolyte is shown in Figure 4.2. The raw data was corrected for the uncompensated solution resistance before plotting. The activity in acid is virtually indistinguishable from the Nernstian diffusion overpotential, which describes the minimum overpotential for a fully reversible catalyst based on the ability to transport reactants to the electrode. In comparison, the activity in basic electrolyte is subject to a significantly greater overpotential.

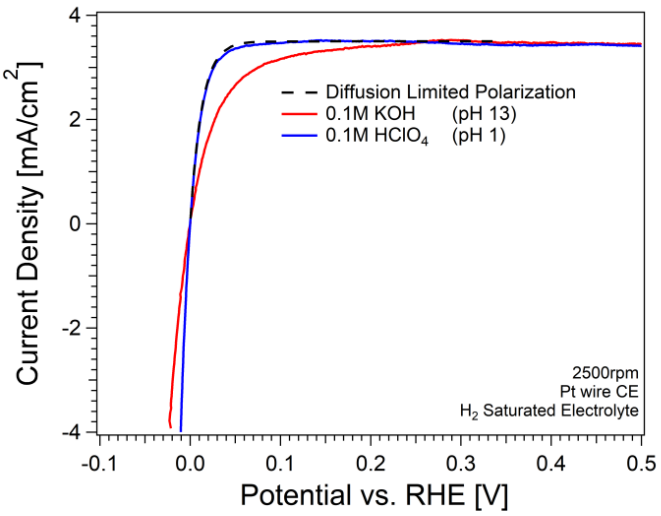

Figure 4.2: Hydrogen oxidation and evolution activity on Pt/C catalysts in acidic and basic electrolyte. The curves were corrected for the uncompensated solution resistance (measured from PEIS).

Alloying platinum with ruthenium is well known to produce a more active catalyst in basic environments. Figure 4.3 shows the RDE polarization curves for the PtRu/C alloy catalyst compared to the standard Pt/C catalyst in basic electrolyte. The activity is significantly improved for the PtRu alloy, coming close to the Nernstian diffusion limited overpotential and therefore the activity in acid.

From the discussion earlier, ruthenium is known to be more oxyphilic than platinum, and, as evident from the static CV curves of the electrodes in nitrogen saturated electrolyte, the hydrogen adsorption peaks are shifted toward the negative for the PtRu catalyst; this means the increased kinetics could arise from a weakening of the Pt-H bond strength or the presence of surface oxides/hydroxides on the ruthenium to accept the protons.

Several researchers have shown that alloying Pt with cobalt or niobium does not change the potential of hydrogen adsorption, yet still leads to a dramatically increased hydrogen oxidation activity[105,106]. Similarly Bates showed that alloying Pt with copper does not affect the hydrogen under-potential deposition peak locations but leads to significantly higher activity[105]. The activity diminished after leaching out the copper in an acidic media. This indicates that the HOR on platinum is limited by the removal of adsorbed hydrogen due to the electrostatic repulsion of the hydroxide.

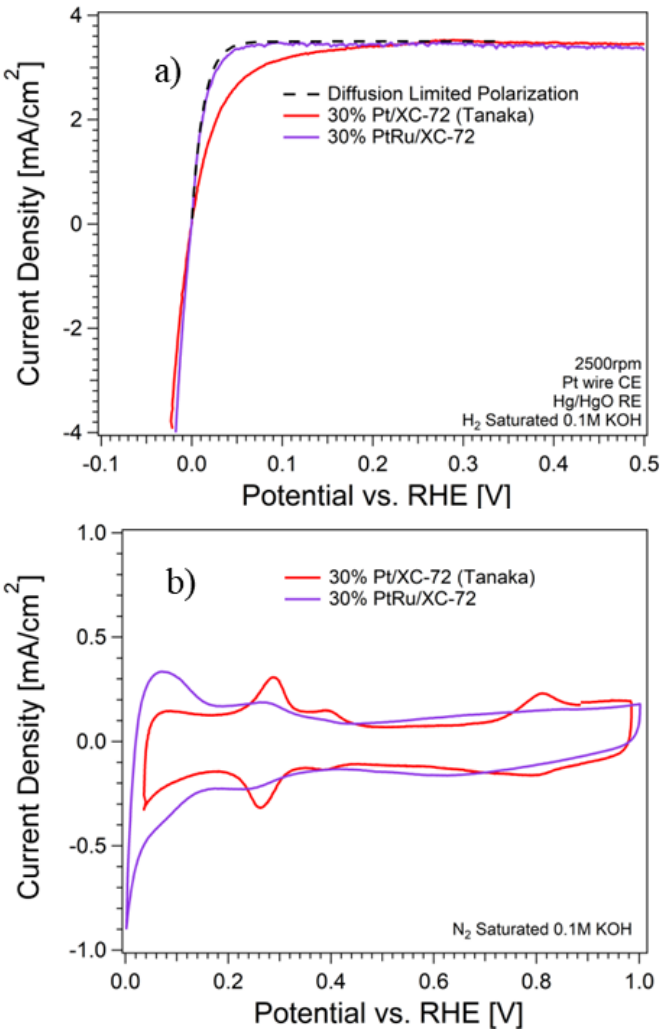

Figure 4.3: a) Hydrogen oxidation and evolution on Pt/C and PtRu/C catalysts in 0.1M KOH. The curves were corrected for the uncompensated solution resistance (measured from PEIS). B) static CV plots of the catalysts in N_2 saturated electrolyte.

Single Cell AEMFC Testing

In cell testing was conducted to try to improve anode performance in AEMFCs. This work was facilitated by the inclusion of a pseudo-reference electrode in the cell in order to apportion the cell overpotential to each electrode. In previous studies of cathode catalysts, it was observed that a significant amount of the cell overpotential was attributed to the anode. It was also observed that the anode performance varied significantly from cell to cell despite consistent loadings and test conditions.

Figure 4.4 shows a typical AEMFC polarization curve and the overpotential from each electrode. The cathode has a significant amount of overpotential in the kinetic region which is expected from the poor kinetics of the ORR compared to HOR. Outside the kinetic region, the cathode polarization does not change significantly with increasing current and there is no observed mass transport limit due to the high stoichiometric factor in the cathode feed (11.5 A). The anode overpotential increases almost linearly with current density throughout and is the major source of cell overpotential overall. The dashed lines represent the expected electrode polarizations from extrapolating the measured kinetic currents of ex-situ RDE tests and normalizing to the electrode loading used in AEMFC testing. The cathode behavior nearly perfectly matches expectation. The anode, however, has significantly higher polarization than expected.

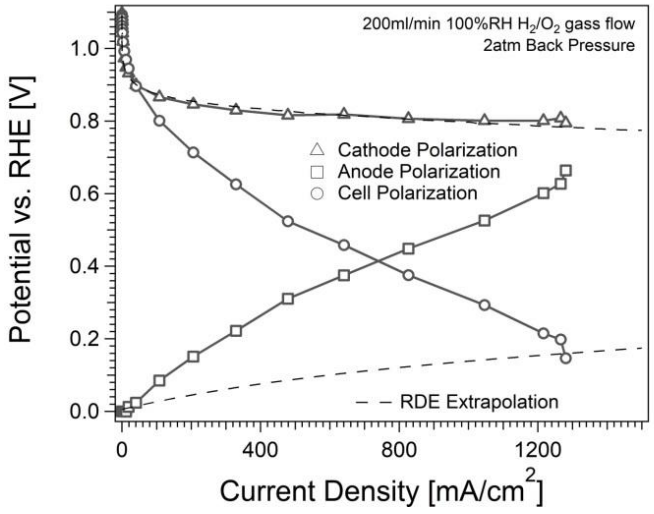

Figure 4.4: AEMFC polarization curves comparing the observed electrode performance to the expected activity determined from extrapolation of ex situ RDE studies data. 80°C cell temperature with 200 ml/min 100%RH H_2 and O_2 gas flow rates, 2 atm backpressure.

AEMFCs were constructed and tested with different anode loadings to determine if the poor anode performance results from decreased HOR kinetics on platinum in alkaline environments. The electrode polarization from AEMFCs using 4 different platinum loadings are illustrated in Figure 4.5a. If the large anode overpotentials were caused by poor HOR catalysis it would be expected that increasing the catalyst loading would lower the anode overpotential. However, this was not observed. The 0.2 mg_{Pt}/cm^2 and 0.4 mg_{Pt}/cm^2 were very similar and the 0.8 mg_{Pt}/cm^2 was worse. To further investigate, anode electrodes were prepared with a PtRu alloy nanoparticle catalyst. In RDE tests, these catalysts were nearly reversible. Therefore, it was expected that the anode polarization with these catalysts would be significantly lower. However, as shown in Figure 4.5b, the PtRu/C catalyst showed worse performance than Pt/C. This suggests that there is another factor which limits the HOR in AEMFC anodes.

The poor anode performance could also be explained by flooding of the electrode or poisoning of the platinum. Ex-situ testing of Pt catalysts in alkaline solutions containing cationic moieties, such as those in anion exchange membranes and ionomers, have shown dramatically reduced HOR and ORR performance[109,110]. It has been suggested that these groups show a similar poisoning behavior when attached to a polymer backbone and incorporated into the catalyst layer[105]. To determine a possible poisoning effect, RDE studies were conducted using Pt/C catalysts layers with either a Nafion® cation exchange ionomer, the Tokuyama AS4 anion exchange ionomer, or no ionomer. The cyclic voltammograms in nitrogen saturated electrolyte are shown in Figure 4.6a. Neither of the electrodes with a binder causes a reduction in the H-UPD peaks, which would be expected if there was a poisoning effect. There is a noticeable difference in the capacitance of the binder free catalyst layer and the catalyst layers which contain a binder. This may be due to a more uniform coating of the glassy carbon electrode resulting in a larger catalyst surface area in the latter. Figure 4.6b shows the hydrogen oxidation activity of the catalyst layers. There is no difference in the kinetic region, but a slight reduction in the diffusion limited current for both of the electrodes with binders present.

Based on these results, it does not appear to be the case that anion exchange ionomers poising the platinum surface or poor catalysis is the cause of poor anode performance observed in AEMFCs. Therefore, flooding is the most probable cause. Further work focused on optimizing AEMFC anode structure to improve performance with regard to flooding.

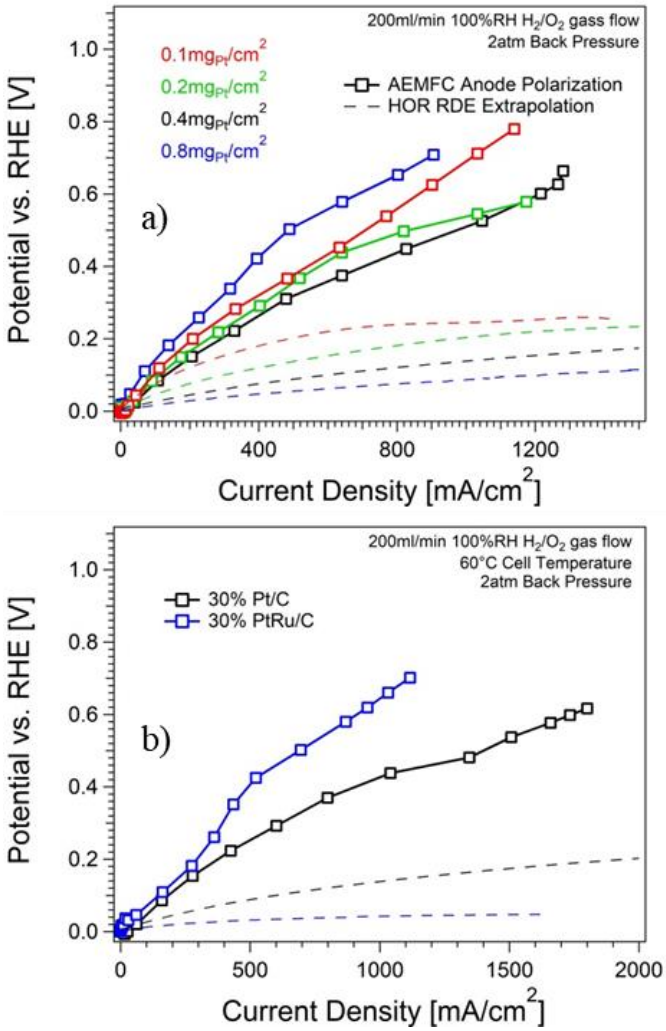

Figure 4.5: Anode polarization curves for AEMFC with different a) anode loadings and b) anode catalyst type (with 0.4 mg_{PM}/cm^2 loadings). 80°C cell temperature with 200 ml/min 100%RH H_2 and O_2 gas flow rates, 2 atm backpressure.

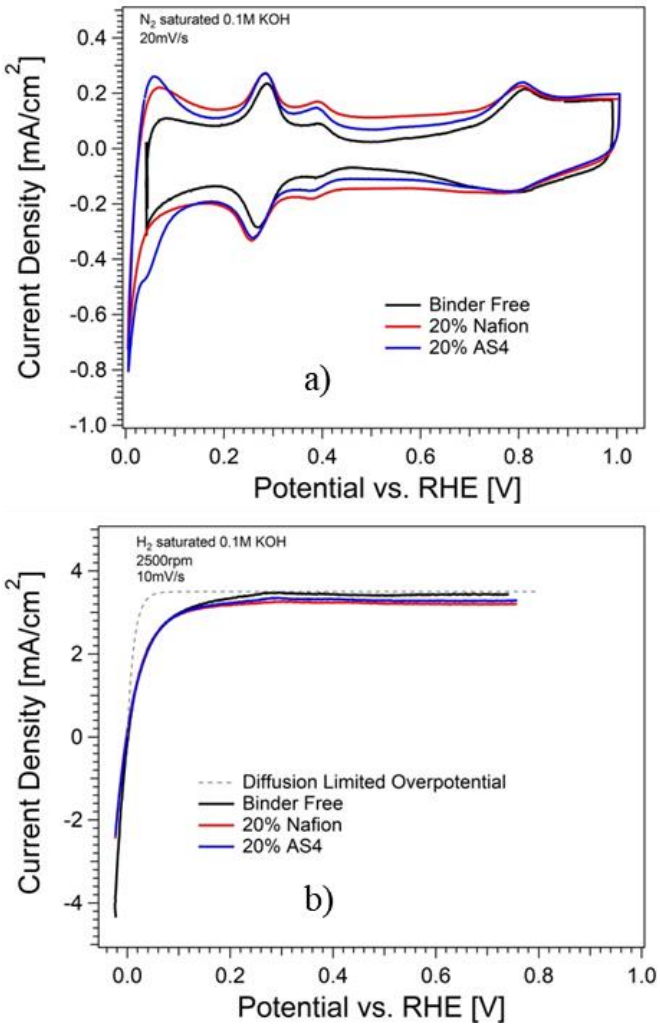

Figure 4.6: a) Cyclic voltammograms in nitrogen saturated electrolyte and b) HOR RDE plots in hydrogen saturated electrolyte for Pt/C catalysts with different binders

Tests were conducted using equivalent catalyst coated membranes, but different anode gas diffusion layers. The polarization plots are shown in Figure 4.7 and data is provided in Table 4.1. All of the GDLs compared contained no microporous layer (MPL). In previous tests, under different cell testing conditions (i.e. lower cell temperature), the anode performance was worse when GDLs containing microporous layers were used; this was the case for MPL containing GDLs with (Sigracet 25BC) and without (Fruedenberg F2) PTFE treatment. The thinnest GDL, Toray TGP-H-030, had much greater issues with flooding, reaching only ~100 mA/cm2 before the cell died. The thickest electrodes, Toray TGP-H-090 and Sigracet 35AA, had similar anode performance. The medium level thickness Toray paper without PTFE treatment was worse than the thicker electrodes, while the Spectracarb 2050A was slightly better. An interesting and unexpected result of the tests was the variance in the cathode electrode performance despite using the same loadings, test conditions, and GDL type for the cathode in each test. This suggests that there may be some interplay between anode and cathode performance which must be accounted for while optimizing electrode performance.

The anode catalyst layer ink formulation was modified in a further effort to optimize the AEMFC anode performance. It is well known from PEMFC research that the chosen solvent dielectric constant and boiling temperature can affect the structure of the catalyst layers[111–113]. Here several ink solvents were chosen; the solvent characteristics are displayed in Table 4.2.

IPA is the standard ink solvent used for the bulk of the work. THF was chosen as a comparison because the boiling point is similar (the substrate temperature for spray painting was lowered from 80°C to 60°C for this electrode to try to achieve similar solvent evaporation rates), while the dielectric constant is significantly lower. Butanol on the other hand was chosen because the dielectric constant is similarly but the boiling point is significantly higher. A plot of the electrode polarization from these AEMFCs is shown in Figure 4.8. The THF solvent anode catalyst layer performed worse than the IPA ink, the cathode catalyst layers from these cells had nearly identical performance. The anode catalyst layer prepared with the butanol solvent vastly outperformed the IPA ink solvent, suggesting this electrode structure was able to remove water more efficiently from the catalyst layer.

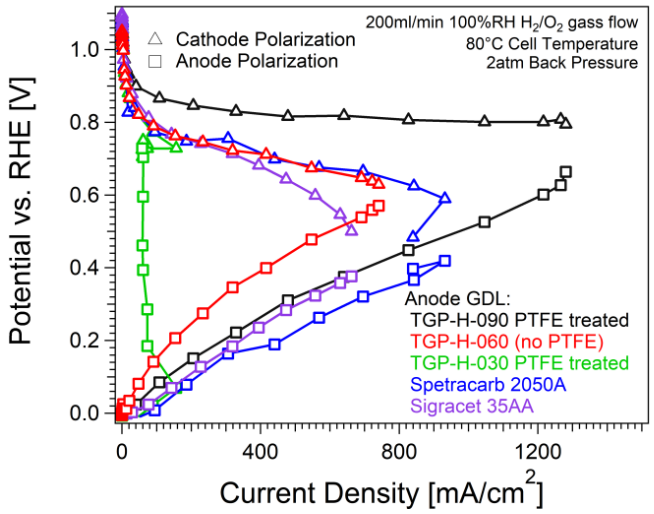

Figure 4.7: Electrode polarization in AEMFCs with different anode GDLs. 80°C cell temperature with 200 ml/min 100%RH H_2 and O_2 gas flow rates, 2 atm backpressure.

Table 4.1: Anode GDL characteristics and corresponding cell performance

Anode GDL	PTFE?	Thickness (µm)	E_{an} @0.5A/cm^2	E_{ca} @0.5A/cm^2
Toray TGP-H-030	Yes	90	N/A	N/A
Toray TGP-H-060	No	180	0.450V	0.685V
Toray TGP-H-060	Yes	270	0.316V	0.818V
Spectracarb 2050A	No	150	0.294V	0.685V
Sigracet 35AA	No	300	0.220V	0.635

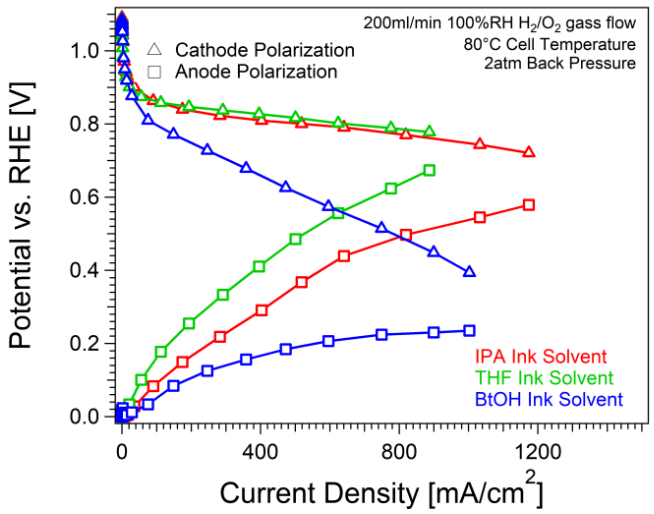

Figure 4.8: Electrode polarization for AEMFCs with anode catalyst layers prepared using different inks. 80°C cell temperature with 200 ml/min 100%RH H_2 and O_2 gas flow rates, 2 atm backpressure.

Table 4.2: Characteristics of solvents used for AEMFC anode ink formulations.

Solvent	Dielectric Constant (ε)	Boiling Point (°C)
Tetrahydrofuran (THF)	7.6	66
Isopropanol (IPA)	17.9	82
Butanol (BtOH)	18	118

A brief discussion of water management in fuel cells would be helpful towards further discussion. Proper water management in PEMFCs has long been known to be a significant concern. Since water is produced at the cathode, it must be removed efficiently to prevent electrode flooding at high current densities. Water is also dragged along with the protonic current from the anode to the cathode through the membrane and a buildup of water at the cathode causes back diffusion towards the anode. A balance must be achieved to prevent the membrane from drying out, which would lower the conductivity and increase cell resistance, while also preventing electrode flooding.

Water management in AEMFCs is even trickier. In AEMFCs twice as much water is produced from the reaction (in this case at the anode), but it is also a reactant at the cathode. Water will be dragged towards the anode with the hydroxide conduction. A buildup of water at the anode will cause back diffusion towards the cathode. Therefore in AEMFCs water must be managed to prevent the anode from flooding and the cathode from drying out.

As this relates to the above results, it is likely that the anode in most cases was at least partially flooded due to a large buildup of water. While this caused poor anode performance, the large buildup of water caused a significant amount of diffusion of water from the anode to the cathode. In the case of the anode catalyst layer prepared with the BtOH solvent, the structure of the catalyst layer allowed for more efficient removal of the water. However, this also resulted in less diffusion of water back towards the cathode and resulted in poorer cathode performance from water starvation despite high humidity in the oxidant gas flow.

Conclusion

The activity of platinum catalyst for hydrogen oxidation in alkaline is significantly lower than in acid. However, it has been shown that the performance can be increased by alloying the platinum with more oxyphilic metals which are significantly less expensive than platinum. As such it will be possible to produce an AEMFC anode catalyst which is close in cost to those used in PEMFCs.

However, the poor performance of anode electrodes in AEMFCs has been demonstrated to not be a result of poor catalysis, as increasing the catalyst loading didn't improve performance. It was found that anode catalyst layer flooding is the likely limiting factor in AEMFC anode performance. By changing the catalyst layer ink solvent it is possible to increase performance, however this comes at the detriment of the cathode performance. In order to improve overall AEMFC performance a significant amount of research must be conducted to better understand water transport in AEMs and develop better methods for water management.

Part 2: Membranes for Alkaline Fuel Cells and Batteries

Introduction and Background

Electrolytes are responsible for transferring ionic charge between electrodes in electrochemical devices. Electrolytes are characterized by their ability to conduct a charge between two electrodes. High conductivities are necessary in order to minimize the resistance losses in the cell; therefore, high temperatures or thin electrolyte gaps are preferred.

The first electrolytes used in devices were aqueous salt or acid solutions. While highly conductive, the use of aqueous electrolytes imparted severe limitations on early batteries and fuel cells such as danger of electrolyte spillage/leakage, limited potential window, and inability to use the battery in different orientations. Early on this was overcome by forming electrolyte pastes or gels which are still commonly used in commercial single-use batteries.

Current rechargeable batteries typically use salts dissolved in either water or an organic solvent depending on the potential of the cell. Nickel cadmium and nickel metal hydride systems use aqueous concentrated potassium hydroxide solutions while lithium ion batteries use lithium salts dissolved in and organic solvent. Aqueous solutions generally exhibit higher conductivities and are considered safer due to the flammability of organic solvents. However, water has a relatively narrow electrochemical window, the region in which it is neither oxidized nor reduced, limiting it to devices with potentials below 2 V. For the higher energy density batteries, such as lithium ion, an organic solvent is required. These electrolytes typically have much lower conductivities than aqueous systems.

The use of liquid electrolytes in fuel cells has largely been phased out over the past half century. Solid ceramic and molten salt electrolytes are used at high temperatures (>200°C) and solid polymer electrolytes are used at low temperatures (<200°C). The use of polymer electrolytes in low temperature fuel cells was preferred over liquid electrolytes because they eliminated issues of electrolyte leakage and salt precipitation.

Chapter 5: Anion Exchange Membranes for Fuel Cells

Introduction

The first polymer exchange membrane used fuel cells were based on sulfonated polystyrene. These early PEMFCs were developed for NASA, but they had issues with oxygen crossover and poor performance. The development and subsequent use of Nafion helped to make PEMFCs the standard for low temperature systems.

The perflourinated backbone structure of Nafion imparts a very high chemical resistance and also results in phase segregation between the hydrophobic backbone and the functionalized sidechains. This segregation leads to hydrophilic and hydrophobic domains; the result is a membrane which has extraordinary conductivity (~0.1 S/cm at room temp), due to the hydrophilic regions, and outstanding mechanical strength, due to the hydrophobic regions. The few drawbacks of Nafion are large changes in dimensions when hydrated vs. dry, reduction in conductivity at low relative humidity, and high cost. Nafion has remained the standard membrane material for PEMFCs, despite an extensive research effort into cheaper hydrocarbon based PEMS.

In order for AEMFCs to succeed AEMs need to demonstrate similar properties to Nafion. Desirable AEM properties should include:

- High conductivities of at least 60 mS/cm at operating temperature (80°C)
- Mechanically stable enough to produce thin membranes (20-50 μm)
- Dimensional stability at various levels of hydration.
- Long term stability at operating temperature
- Ability to be dried for fabrication of catalyst coated membrane
- Ability to be dissolved or created in situ for compatible ionomers in the catalyst layer
- Low cost

Many cheap commercially available polymers demonstrate satisfactory alkaline resistance to be considered for AEM backbone structures including, simple hydrocarbons, aromatics, and perflourinated polymers. AEMS based on a wide variety of backbone structures have been synthesized[114], the most popular choices have been poly(phenylene oxide)[115–119], polysulphone[120–125], and polystyrene[126–130]; although, the latter is mainly limited to study on solvated polymers or copolymers. Currently, the anion exchange membrane is the biggest material challenge for AEMFCs. AEMs with good mechanical and conductive properties produced thus far have not shown sufficient long term chemical stability, due to degradation of the backbone and/or functional group.

In Nafion, the proton conduction is achieved by a sulfonic acid group which is covalently bonded to the membrane. Hydroxide conduction in AEMs is similarly accomplished by using an organic cation attached to the backbone of the polymer. The ionic groups in anion exchange membranes are typically sulfonium, ammonium, or phosphonium[114,131]. Of these, quaternary ammonium is the most widely studied and is thought to have better chemical and thermal stability[114]. Ammoniums formed from simple alkyl amines are the most commonly used, specifically trimethylamine; however, many other, more exotic, nitrogen containing organic compounds have also been studied. Among these are imidazolium[117,128,130,132], pyridinium[133], guanidinium [118], morpholinium[134], and 1,4-diazabicyclo[2.2.2]octane (DABCO)[115,135]. Figure 5.1 shows examples of organic cations which have been studied for use in AEMs.

The organic cations are susceptible to attack from the hydroxide. Several degradation mechanisms are illustrated in Figure 5.2. Degradation may occur through E1 or E2 elimination, substitution, or ring opening reactions depending on the particular cationic species. Attempts to increase the alkali stability of organic cations have included utilization of compounds without a β hydrogen, to prevent the Hoffman Elimination mechanism (scheme b & c)[114], and addition of a methyl group to the carbon between the nitrogen atoms in imidazolium (scheme d)[128]. Water content has also been shown to have an effect on the stability of the membrane, indicating that solvation of the ionic group is important to chemical stability[114].

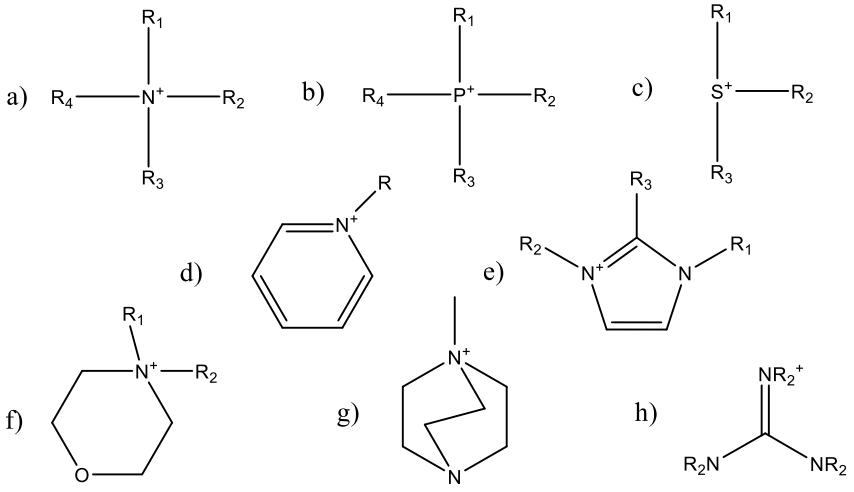

Figure 5.1: Organic cation structures used in AEMs a) Quaternary Ammonium b) Quaternary Phosphonium c) Tertiary Sulfonium d) Pyridinium c) Imidazolium e) Morpholinium f) DABCO g) Guanidinium

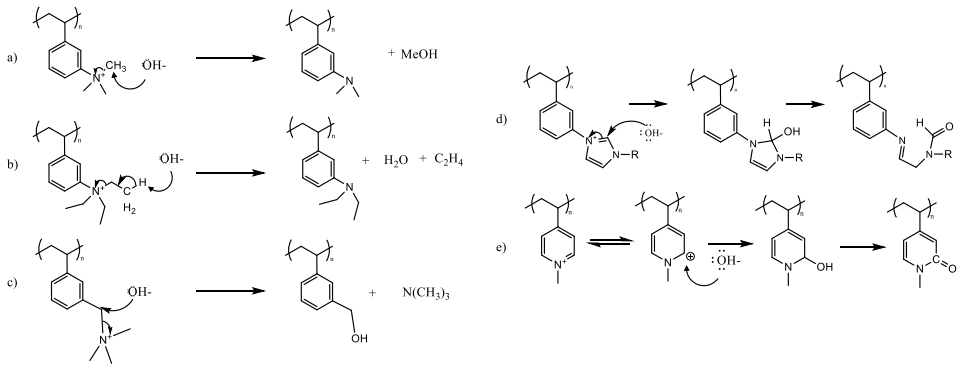

Figure 5.2: Cation degradation mechanisms as suggested by references[114,119,131]

There are also reports that indicate that while backbone structures may demonstrate good base stability, they are susceptible to degradation when functionalized with an organic cation[119,131]. For example, poly(phenylene oxide) is a base stable polymer; however, when an ammonium group is attached it is known to undergo chain scission. Some attribute this backbone degradation to increased contact between the backbone and hydroxide in AEMs, which are more hydrophilic, than in the bulk polymer[119]. However, it is more likely due to electron withdrawing effects from the quaternary ammonium groups as studied by Arges et al[120].

This phenomenon likely works both ways. A quaternary ammonium group may be more stable on a highly aromatized backbone, such as polystyrene, than it would be on a hydrocarbon backbone such as polyethylene. A recent model compound study suggested that quaternary amines which were separated from the aromatic backbone by a long alkane chain exhibited the highest stability among a wide variety of amines which were tested[136]; however, it should be noted that the stability of quaternary ammoniums in model compounds and incorporated into AEMs have not correlated well. Historically, it has been assumed that cations on long alkyl chains would not be stable due to Hoffman Elimination; however, chains longer than 4 carbons appear to have good stability[119].

The conductivity of hydroxide is intrinsically lower than that of protons. Therefore, in order to achieve similar conductance to that of Nafion AEMs must be made thinner or have higher ion contents. This is challenging on both fronts, Nafion membranes currently used in PEMFCs are already quite thin and producing AEMs which are thinner is likely to result in processing issues, e.g. pinholes, or unsatisfactory hydrogen crossover. Increasing the functional groups in the membrane may lead to high water uptake, resulting in poor mechanical stability.

One method to circumvent the latter issue would be to crosslink the AEMs so that they maintain dimensional stability even at high ion contents.

The development of anion exchange ionomers is another important task for AEM research. Typically polymer electrolyte fuel cell binders are made by dissolving the polymer in a low molecular weight alcohol. This is a likely strategy for AEMFCs; however there are several important considerations to take into account. If the AEM is crosslinked, then the binder must either have a different composition or the crosslinking should be carried out after the electrode is produced. The larger issue is the poisoning of platinum by anion exchange ionomers[109,110,137]. The cationic charges in the anion exchange ionomers may act as flocculants and cause agglomeration of the carbon support in inks for AEMFC electrodes. Additionally, Ong et al. showed that the presence of quaternary ammonium groups in RDE solutions had a significant negative impact on the oxidation reduction reaction[109]. Similar results have been observed for the effect of AEMs on HOR for platinum catalysts[110]. This poisoning effect is often overlooked in AEM literature.

The reduced performance of Pt with anion exchange ionomers for the oxygen reduction reaction may not represent a major issue since non-noble catalysts, such as heat treated metal macrocycles, are likely to be used in commercial AEMFCs. However, at the anode, there are no promising non-precious metal catalysts reported in the literature; the poisoning of platinum should therefore be considered a major issue for AEMFCs.

Properties of Controlled Morphology Anion Exchange Membranes

Introduction

AEMs comprised of a common backbone and different cation structures were synthesized in house and by collaborating researchers and tested to determine conductivity, base uptake, water uptake, stability, and catalyst interactions. Poly(phenylene oxide) was chosen as the polymer backbone because it is commercially available, relatively inexpensive, and demonstrates good base stability.

The PPO was modified through a bromination process to attach a halide to the backbone. The halide was further substituted though a quaternization reaction with tertiary amines resulting in quaternary ammonium based anion exchange membranes. This work focused solely on AEMs produced using non-cyclic ammoniums, i.e. imidazoliums, morpholiniums, and pyridiniums were not studied.

Degree of crosslinking, quaternization, and ammonium species were controlled and the effect on properties of the anion exchange membranes was studied. The crosslinking of polymers prevents the phase separation behavior that is observed in Nafion, however since dimensional stability is maintained by the crosslinking, high ionic conductivity may be achieved by high degrees of functionalization.

Controlling Morphology

The remarkable transport properties of Nafion are believed to occur because of the phase separation between the hydrophobic PTFE backbone and the hydrophilic sulfonic acid functionalized side chains. The hydrophilic phase provides hydrated ionic pathways while the hydrophobic chain maintains the mechanical stability. A similar approach has been targeted for the synthesis of anion exchange membranes. AEMs will especially benefit from this approach because the quaternary ammonium groups are believed to be more stable when fully hydrated. Several strategies were developed in an attempt to control membrane morphology.

i. ammoniums groups with short chain along the backbone (Conventional)
ii. long alkyl chains included separately from the ammoniums (Separated)
iii. ammonium groups separated from the backbone with long alkyl chains (Tethered)
iv. ammoniums groups with long alkyl chains along the backbone (Guarded)
v. crosslinking between chains with di-functional amines (Crosslinked)

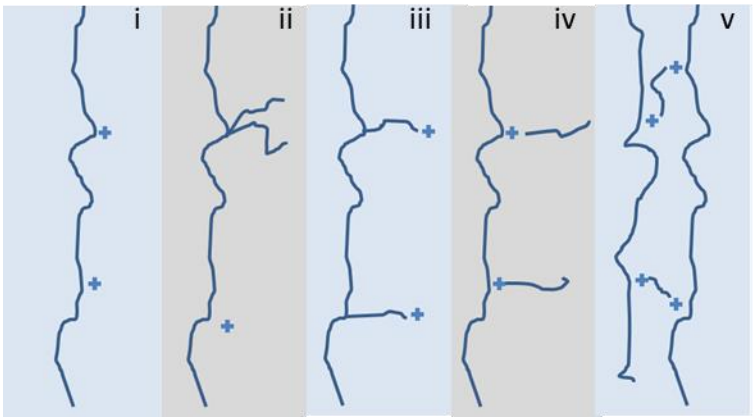

Figure 5.3: Strategies for controlling AEM morphology

Conventional AEMS

Conventional AEMS were made using trimethylammonium (TMA) as the quaternizing amines. These are the most widely studied in the literature and have been produced using a variety of different backbone chemistries. The AEMs were named according to the convention PPO-TMA X^-, where X^- represents the counter ion (OH^-, $HCO32^-$, Br^-, etc.).

Separated AEMS

Separated AEMS were made using trimethyl ammonium as the quaternizing amines. The phase separation was attempted by substituting half of the halide groups with hydrophobic long alkyl chain secondary amines. Separated AEMs were named according to the convention PPO-DOA-TMA X^-, where DOA refers to dioctylamine

Tethered AEMS

In Nafion, and other prominent commercial proton exchange membranes the charge is separated from the backbone by attaching it to a sidechain, which aids in the formation of the ion channels. This was the motivation for studying tethered AEMs.

Tethered AEMS were made with a long alkyl chain separating the ammonium group from the polymer backbone. Tethered amines were named according to the convention PPO-HTMA X^- where the "H" in HTMA refers to the hexyl alkyl chain that separates the ammonium from the backbone.

Guarded AEMS

Guarded AEMS were made using amines with two methyl groups and one 6 carbon long alkyl chain extending out from the backbone chain. It was hypothesized that the long alkyl chain would introduce some hydrophobicity around the ammonium group, shielding it from the hydroxide and producing a more stable AEM. Guarded amines were named according to the convention PPO-DMHA X^-. DMHA refers to the dimethylhexyl amine used to synthesize the cationic group.

Crosslinked AEMS

Guarded, separated, and tethered AEMs have shown the tendency to become water soluble in hydroxide form at high degrees of functionality. This is likely due to the disruption of regularity of the repeat units which is responsible for the formation of crystalline regions. Presumably, longer chain lengths increase this effect. Therefore one advantage of the Crosslinked AEMs is that the membrane will maintain its mechanical stability even at high ion contents.

Crosslinked AEMS were made from each backbone using tetramethyldiamines crosslinking agents which can undergo a substitution reaction at both ends in order to tie together two polymer chains. Crosslinked AEMs were named according to the convention PPO-TMHDA, where TMHDA is the tetramethylhexanediamine.

Experimental

Synthesis Materials

N-Methyl-2-pyrrolidone (NMP) was obtained from Advanced Chemtech. Brominated poly(phenylene oxide) (PPO-Br) (60% degree of functionalization) 10wt% in NMP was obtained from Akron Polymer Systems. Dioctylamine (DOA) (98%) was obtained from Sigma-Aldrich. Trimethyl Amine (TMA) 4.2 M in ethanol, 1-chloro-6-hexanol (95%), N,N-Dimethylhexylamine, (DMHA) (99%), and N,N,N',N'-Tetramethyl-1,6-hexanediamine TMDHA (99%) were obtained from Acros Organics. Sodium hydride (60% in mineral oil) was obtained from Alfa Aesar.

Acetonitrile-d3 (99.8%D) and Toluene-d8 (99.6%D) were obtained from Cambridge Isotope Laboratories Inc. Acetone-d6 (99%D) was obtained from Aldrich Chemical Company DimethylSulfoxide-d6 (99.8%D) was obtained from Norell Inc.

Synthesis of Sodium 6-(trimethylammonium chloride)hexan-1-olate

1ml of 1-hexanol was mixed with 5 ml of 4.2 M trimethylamine in ethanol (3x excess). The reaction was carried out at 60°C for 4 days with constant stirring. The excess trimethylamine and ethanol were evaporated in a vacuum oven at 90°C. The resultant powder was transferred to a nitrogen filled glove box and added to dry THF. An equimolar amount of sodium hydride was then added to form the olate salt. The reaction was carried out with mixing for several days at room temperature before centrifuging to recover the powder, which was washed several times with dry THF before drying under vacuum at room temperature.

Synthesis of poly(phenylene oxide)-trimethylammonium Bromide (PPO-TMA+Br-)

5 ml of 10% PPO-Br in NMP was mixed with 1.5 ml of 4.2 M trimethylamine in ethanol (3x excess) and stirred at 30°C for 4 days. The solution was then cast onto a clean glass plate and placed in an oven at 90°C for 16 hr without vacuum and 8 hr with vacuum.

Synthesis of poly(phenylene oxide)-dioctylamine-trimethylammonium Bromide (PPO-DOA-TMA+Br-)

5 ml of 10% PPO-Br in NMP was diluted with 10 ml of NMP and mixed with 0.12 ml of 4.2 M TMA in ethanol and 0.16 ml of dioctylamine. The addition of organic bases, such as dioctylamine, to the undiluted polymer solution caused immediate and irreversible gelation; the

addition of extra NMP to lower the polymer concentration prevented this. The solution was stirred at 60°C for 1 day before adding equivalent volumes of the amines as before. After another 24 hr of stirring, 0.5 ml of excess TMA was added. 4 days after the initial mixing, the solution was cast onto a clean glass plate and placed in an oven at 90°C for 16 hr without vacuum and 8 hr with vacuum.

Synthesis of poly(phenylene oxide)-Dimethylhexyl ammonium Bromide (PPO-DMHA+Br-)

5 ml of 10% PPO-Br in NMP was diluted with 5 ml of NMP. Separately, 0.385 ml of Dimethylhexylamine was added to 1 ml of NMP. The DMHA solution was added to the PPO solution dropwise. The solution was allowed to stir for 4 days at room temperature before the membrane was cast onto a clean glass plate and placed in an oven at 90°C for 10 hr without vacuum and 16 hr with vacuum.

Synthesis of poly(phenylene oxide)-hexyltrimethyl ammonium (PPO-HTMA+Br-)

2.5 ml of 10% PPO-Br in NMP and 0.27 g of *Sodium 6-(trimethylammonium chloride)hexan-1-olate* were mixed and diluted with 2 ml of NMP. The solution quickly gelled and was transferred to a glass plate which was placed in an oven at 90°C for several hours without vacuum, then 16 hr with vacuum

Synthesis of Crosslinked poly(phenylene oxide) (PPO-)

5 ml of 10% PPO-Br in NMP was diluted with 5 ml of NMP. Separately, 0.215 ml of tetramethylhexyldiamine was mixed with 1ml of NMP. The TMHDA solution was quickly added to the PPO solution and allowed to stir for several seconds to become well mixed. The solution was then immediately cast onto a glass plate and placed in an oven at 25C where it was allowed to react for 2 days before the temperature was increased to 90°C for 24 hr without vacuum and 24 hr with vacuum.

Characterization Materials:

All solutions were prepared with DI water produced from a Milli-Q Millipore 18 Mohm. Certified 1N HCl and NaOH solutions were obtained from Fisher Scientific for titrations. Lithium chloride (99%) was obtained from Acros Organics. Sodium chloride and potassium hydroxide (ACS grade) were obtained from Fisher Scientific

Ion Exchange Capacity

Ion Exchange capacity was determined experimentally from back titrations. The membranes were exchanged to hydroxide form by placing in 1 M KOH at room temperature for 24 hr with one exchange of solution and then removing the excess hydroxide by rinsing the

membrane thoroughly and placing in DI water for 24 hr with two exchanges of solution. The membranes were transferred to 25 ml solutions of 0.01 M HCl for 24 hr. The membranes were transferred to DI water for an additional 24 hr to leach out excess hydrochloric acid. The membranes were removed and dried under vacuum at 90°C for 24 hr and then weighed. The hydrochloric acid solution was combined with the leached water solution and titrated with sodium hydroxide using a Mettler Toledo DL-15 autotitrator. A blank 25 ml 0.01 M HCl solution was titrated for comparison. The IEC was determined by:

$$IEC\ (mmol/g) = \frac{(mol\ H^+)_{blank} - (mol\ H^+)_{membrane}}{dry\ membrane\ mass\ (g)} \quad [5.1]$$

Uptake and Conductivity of AEMs in Hydroxide Solutions

The base and water uptake and ionic conductivity of membranes saturated of hydroxide solutions ranging from 0-10 M were measured in order to build a detailed picture of the behavior of the AEM in a basic medium. All work with hydroxide solutions of concentrations 1 M or less and hydroxide form membranes was conducted in a glovebox to prevent the membranes from being exposed to carbon dioxide; thereby eliminating concerns of carbonate formation. Tests with concentrations between 2 and 10 M were conducted in open atmosphere as carbonate formation has not been observed to lead to significant carbonate build up on the timescales of interest.

Each membrane was placed in hydroxide solutions for 24 hr with one exchange of solution to fully equilibrate. The conductivity was measured and the membranes were replaced in solution for several hours to re-equilibrate. The saturated mass of the membranes was then recorded with care taken to remove any solution from the membrane surface. The membranes were placed in 0.1 M NaCl for 24 hr with one exchange of solution to ion exchange the membranes and leach out hydroxide. The membranes were then removed, rinsed well, soaked in DI water for 24 hr to remove excess electrolyte, and then dried at 90°C under vacuum for 24 hr. The hydroxide content of the sodium chloride solutions was determined using a Mettler Toledo DL15 autotitrator and hydrochloric acid as the titrant. After drying the mass of the membranes was measured.

The base uptake and water content and swelling ratios (BU, WC, & SR) were determined by:

$$\mathrm{BU[mol/kg]} = \frac{\mathrm{moles\ OH^-}}{\mathrm{m_{dm}}} * 10^6 \quad [5.2]$$

$$WU(\%) = \frac{(m_{sm} - \text{moles } OH^- * M_{KOH} - m_{dm})}{M_{H2O} * m_{dm}} = \frac{\text{moles } H_2O}{\text{moles QA}} \quad [5.3]$$

$$WC = \frac{(m_{sm} - \text{moles } OH^- * M_{KOH} - m_{dm})}{M_{H2O} * (\frac{IEC * m_{dm}}{1000})} = \frac{\text{moles } H_2O}{\text{moles QA}} \quad [5.4]$$

Where moles OH^- was determined from the titration, m_{dm} is the dry mass of the membrane in mg, m_{sm} is the mass of the saturated membrane in mg, M_{KOH} is the molar mass of KOH, M_{H2O} is the molar mass of water.

The conductivity was determined using potentio-electrochemical impedance spectroscopy (PEIS). Briefly, the equilibrated membrane was removed from solution, the excess solution was wiped away, and the membrane was placed in a 4 electrode conductivity cell. The membrane resistance was measured by applying a PEIS sweep from 10^5 to 1 Hz and circle fitting the resultant Nyquist plot to determine the high frequency resistance. The width and thickness of the membrane were then measured and the conductivity determined with the equation:

$$\sigma = \frac{L}{R * T * W} \quad [5.5]$$

Where R is the high frequency resistance determined from the Nyquist plot, W and T are the average width and thickness and L is the distance between the cell's two inner electrodes.

Swelling Ratio

The swelling ratio of the membrane is a measure of the dimensional stability between the dry and hydrated states. When the cell is not in operation for extended periods, it is possible that the membrane will dry out, and then rehydrate as the cell is operated. For membranes with a large swelling ratio, there is an increased risk of mechanical failure from the stress this repeated expansion and contraction cycling imposes. The swelling ratio is determined by measuring the area of a strip of membrane in the dry state (Cl- form) and hydrated state (OH- form). The dry state was measured in the chloride form to prevent degradation of the cationic sites during membrane drying.

$$SR = \frac{\text{Area of Saturated Membrane}}{\text{Area of Dry Membrane}} \quad [5.6]$$

Hydroxide form Membrane Handling and Ion Exchanging

Membranes were transferred to a nitrogen filled glovebox for ion-exchanging to hydroxide form. 1 N Sodium hydroxide was placed in the glovebox before opening and exposing to the atmosphere. This was done to avoid any carbonate formation in the membrane. The

membranes were placed in sodium hydroxide solutions for 24 hr with 1 exchange of hydroxide, then rinsed and placed in DI water for 24 hr with 2 exchanges of solutions.

Hydroxide form water content of AEMs at different water activities and temperatures

The membranes were placed in vials which were placed in a secondary container with LiCl solutions of known concentration to control the water activity. The secondary containers were then sealed and removed from the glovebox. The membranes were allowed 7 days to equilibrate with the water activity before placing in an environmental chamber to control the temperature. The membranes were given 2 additional days to equilibrate with the new temperature. The vials were then removed from the secondary container and quickly capped. The membranes were removed from the vial and weighed, then soaked in 0.1M HCl for 24hr followed by DI H_2O for 24hr to convert to chloride form for drying. The membranes were dried at 90°C for 24hr under vacuum and then weighed. Water uptakes of the AEMs were determined by suspending the membranes of LiCl solutions at room temperature and weighing the membranes after equilibrating for a sufficient period of time. The conductivity of the membranes at different water activities was determined by placing hydrated membranes in their hydroxide forms in a conductivity cell over and suspending the cells over a solution of lithium chloride of known molality within a sealed container. The container was placed in an environmental chamber to control the temperature.

$$WC = \frac{(m_{sm} - m_{dm})}{M_{H2O} * (\frac{IEC * m_{dm}}{1000})} = \frac{\text{moles } H_2O}{\text{moles QA}} \quad [5.7]$$

Where m_{sm} is the mass of the saturated membrane in mg, m_{dm} is the mass of the dry membrane in mg, and M_{H2O} is the molar mass of water.

Hydroxide form stability

In order to probe the stability of the AEMs, each membrane in hydroxide form was assembled into a windowed conductivity cell which allows the membrane access to water vapor. The cells were suspended over LiCl solutions in sealed containers. The water activity of the system was controlled by the LiCl concentration. The containers were held in an environmental chamber at 80°C and the conductivity of the membrane was tracked over time.

Results and Discussion

Currently there is no established methodology for characterizing and monitoring the physical, chemical, and transport properties of AEMs. This makes comparison of results in the literature extremely difficult. Here the uptake, conductivity, and stability of anion exchange

membranes from different morphological classes (conventional, guarded, tethered, etc.) are studied and compared. The initial property characterization entailed determination of the membrane ion exchange capacity, base/water uptake behavior, conductivity over a range of hydroxide concentrations and at different water activities. The degradation monitoring entailed evaluating changes in membrane conductivity over time exposed to high temperatures at low and high water activities.

The relevant membrane properties for PPO based AEMs in their pure hydroxide form are displayed in Table 5.1. The experimentally determined IEC for most of the AEMs is below the expected value calculated from the membrane stoichiometry indicating that incomplete conversion of the bromide groups to quaternary ammoniums occurred. The exception was the PPO-DOA-TMA which had a significantly higher IEC than expected. This likely indicates a higher TMA to DOA ratio than the 1:1 which was targeted. Based on the IEC the actual ratio is likely close to 2:1.

The swelling ratio of the membranes is a measure of the dimensional stability between the dry and hydrated states. When the cell is not in operation for extended periods, it is possible that the membrane will dry out, and then rehydrate as the cell is operated. For membranes with a large swelling ratio, there is an increased risk of mechanical failure from the stress this repeated expansion and contraction cycling imposes. The membranes with the shortest methyl groups surrounding the quaternary ammonium, PPO-TMA and PPO-HTMA, had significantly higher swelling ratios, more than doubling in size. In contrast the membranes with long alkyl chains and the crosslinked membranes only expanded 20-40%, which is close to the commercial A201. The PPO-DMHA, PPO-DOA-TMA, and PPO-TMHDA would be expected to hold up better to the stresses from repeatedly drying out and being rehydrated.

Table 5.1: Properties of PPO based anion exchange membranes. [a]Fully hydrated in OH^- form in a CO_2 free environment

Membrane	IEC_{calc} [mmol/g]	IEC_{exp} [mmol/g]	SR^a (%)	λ^a [mol H_2O/molQA]	σ^a [mS/cm]
Tokuyama A201	1.7	2.05 ± 0.13	118	16.0	32.1
PPO-TMA	2.96	2.23 ± 0.15	206	58.8	57.9
PPO-DOA-TMA	1.28	1.90 ± 0.16	122	15.7	20.3
PPO-HTMA	2.83	2.08 ± 0.13	273	271.5	60.1
PPO-DMHA	2.45	2.16 ± 0.23	135	20.7	38.7
PPO-TMHDA	2.96	2.75 ± 0.13	135	19.0	42.6

Intuitively it would be expected that the degree of swelling is related to the amount of water taken up by the membrane. The data for the membrane water contents appear to confirm this relationship. Fully hydrated Nafion® has a water content (number of water molecules per sulfonic acid group) of roughly 22[138]. The PPO-DMHA, PPO-DOA-TMA, and PPO-TMHDA membranes as well as the A201 have values fairly close to this. The PPO-TMA has a water content roughly 3 times higher than the other membranes and the PPO-HTMA has an extraordinarily high water contents over 10 times higher than the other membranes. The water content and swelling ratio for these two membranes suggest that they may not be practical candidates for AEMFCs. The conductivity of the membranes, except for PPO-DOA-TMA, surpassed that of the A201. However, all membranes still fall short of the conductivity of Nafion, which is ~100 mS/cm.

There appears to be a relationship between higher water contents and higher conductivities in these AEMs. The conductivity, water and base uptake of PPO-AEMs in hydroxide solutions over a range of concentration from 0-10 M was studied. The conductivity and water content of membranes equilibrated in these solutions are shown in Figure 5.4. The membrane water content decreases with the increasing solution hydroxide content. This would be expected from well-known relationship between decreasing water activities and increasing electrolyte concentration in PEMs[139]. As observed with the hydroxide form membranes in pure water, the conductivity decreases with the membrane water concentration despite the presence of extra charge carriers from the electrolyte.

Membrane hydration history has long been known to affect the conductivity and water content of PEMs[140]. This was also observed for the PPO based AEMs in this work. Prior to equilibration with the solution for measurements the membranes were pretreated in one of two ways; dry or hydrated. The dry membranes were dried in chloride form at 90°C under vacuum for 24 hr. For the hydrated membranes the dry membranes were soaked in water for 24 hr. Depending on the cation structure the pretreatment method had either a dramatic or insignificant effect on the water uptake and conductivity. For membranes with a more hydrophilic cation (e.g. PPO-TMA and PPO-HTMA), the hydrating pretreatment imbibes the membrane with more water than it would otherwise contain leading to higher conductivities and water contents in more concentrated solutions. For membranes with hydrophobic cations (e.g. PPO-DMHA) there is little difference between the pretreatment methods. These results are shown in Figure 5.5.

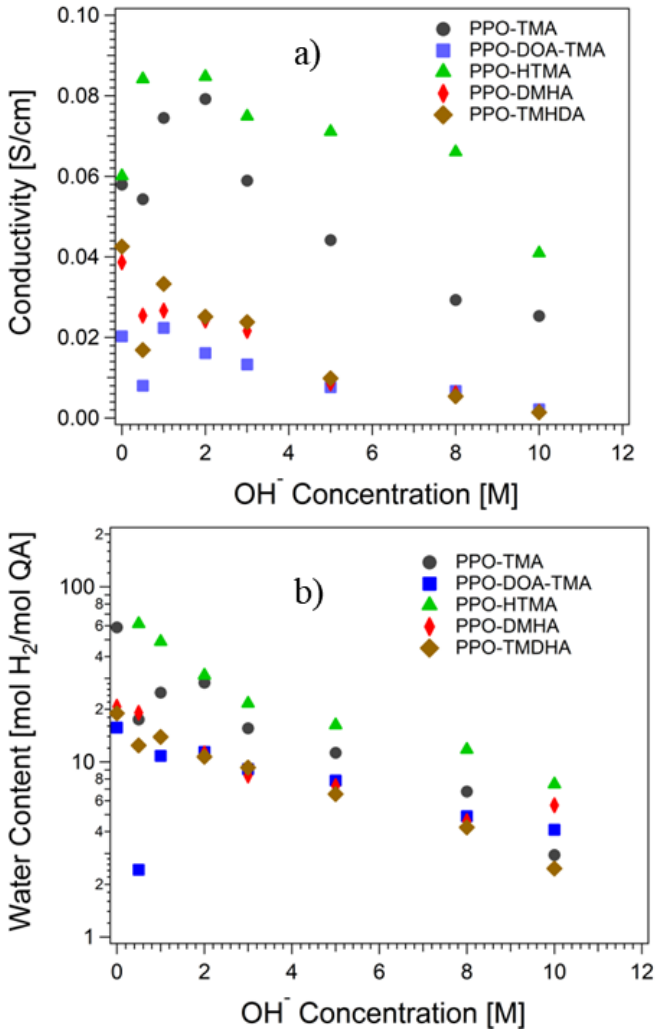

Figure 5.4: a) conductivity and b) water content of PPO based AEMs equilibrated in hydroxide solutions ranging from 0-10 M after drying at 90°C for 24 hr.

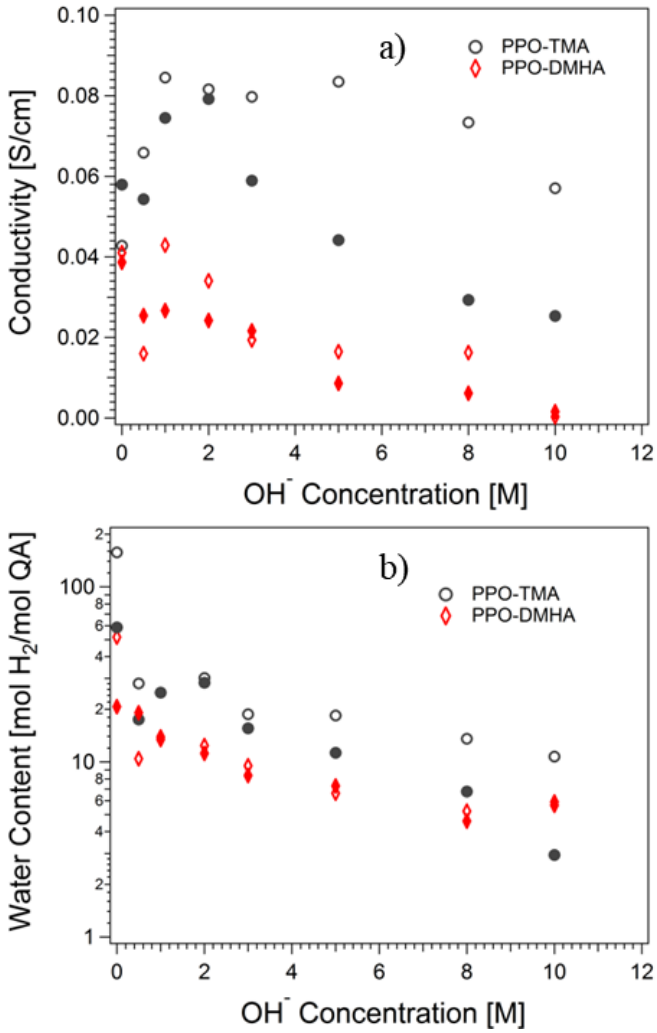

Figure 5.5: a) conductivity b) water content of PPO-AEMs with different cation structure in hydroxide solutions. Open symbols- "hydrated" pretreated membranes; closed symbols- "dry" pretreated membranes

The dependence of membrane water content on the temperature and water activity of the environment was measured for each of the different AEMs in the pure hydroxide form. The results are shown for each membrane in Figure 5.6a-e. It is apparent that the temperature only has a significant effect on the water content at very high water activities. Figure 5.7 compares the water content of different membranes at room temperature and 80°C. At high water activities there is a pronounced difference in water content between membranes with easily hydrated cations and membranes with "guarded cations". The PPO-TMA, PPO-DOA-TMA, PPO-HTMA have much higher water uptakes in environments with water activities between 0.95 and 1. As the water activity decreases, the difference in water content between membrane types disappears.

The stability of the membranes was probed by measuring conductivity changes over time for membranes at 80°C and equilibrated with a high water activity of 0.95, and a relatively low water activity 0.5, the results are shown in Figure 5.8c.

In the high water activity environment the membranes had water contents between 17 & 70 moles of water per mole of quaternary ammonium depending on the specific membrane. Under these conditions, the membranes maintained their conductivity over at least a 40 day period, with the exception of the PPO-DOA-TMA which slowly degraded. The PPO-TMA experienced a significant drop in conductivity after ~40 days.

At the lower water activity, the membranes all had water contents between 2.5 & 4.5 water molecules per quaternary ammonium. As expected, the conductivity of these membranes degraded much more quickly than at high water activity. Given that the water contents in these membranes are all similar it is possible to speculate on the relative stability of each cation. Among the different membranes the PPO-HTMA was the most stable, indicating that separating the cation from the membrane with a long alkyl chain increases stability. The PPO-TMA and PPO-DOA-TMA membranes showed a similar decay rate, which may be expected given that both membranes contain the same cation. These membranes showed the quickest decay indicating the simple cation structure is the most susceptible to degradation. The guarded cations, surrounded by at least one long alkyl chain, i.e. PPO-DMHA and PPO-TMHDA, decade more quickly than the PPO-HTMA but slower than the PPO-TMA indicating the long alkyl chains may help to protect the cation at low water activities.

The results highlight the importance of maintaining cell hydration to extend the life of the anion exchange membrane.

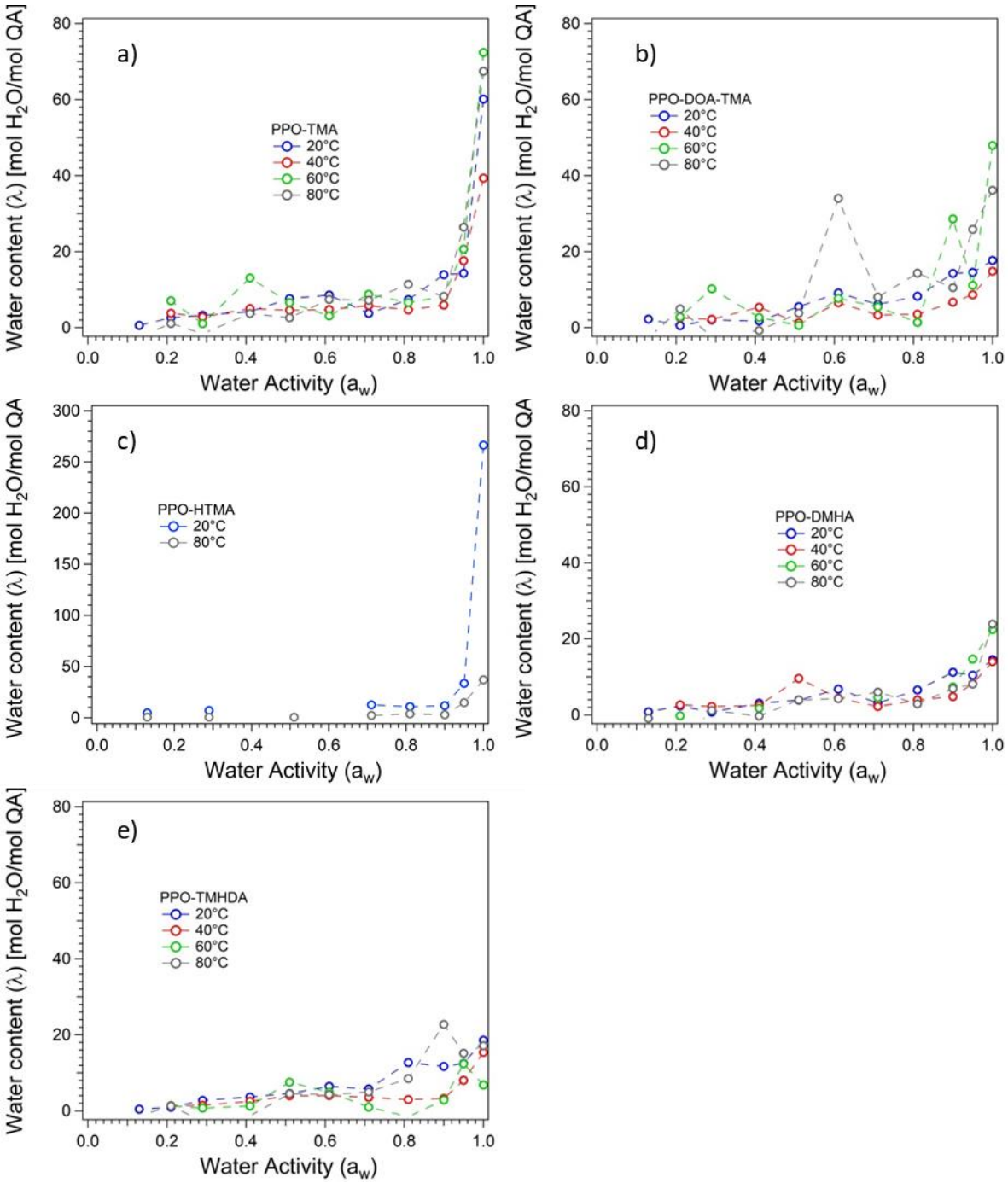

Figure 5.6: Water Uptake for a) PPO-TMA, b) PPO-DOA-TMA, c) PPO-HTMA, d) PPO-DMHA, and e) PPO-TMHA membranes equilibrated with different water vapor activities at several different temperatures.

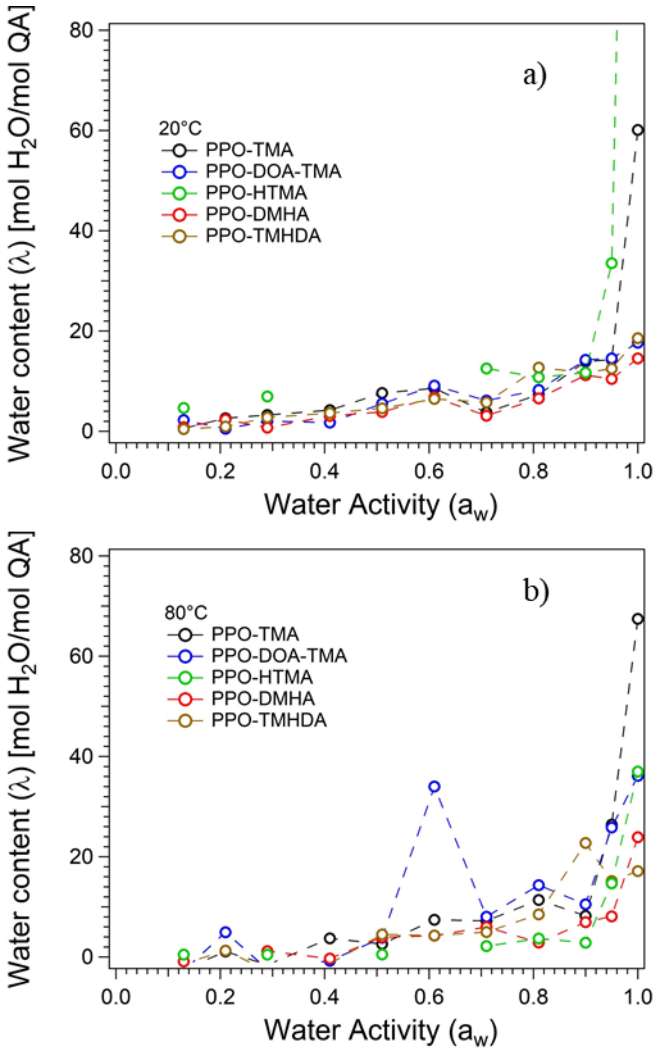

Figure 5.7: Water Uptake for the different membranes equilibrated with different water vapor activities at a) 20°C and b) 80°C.

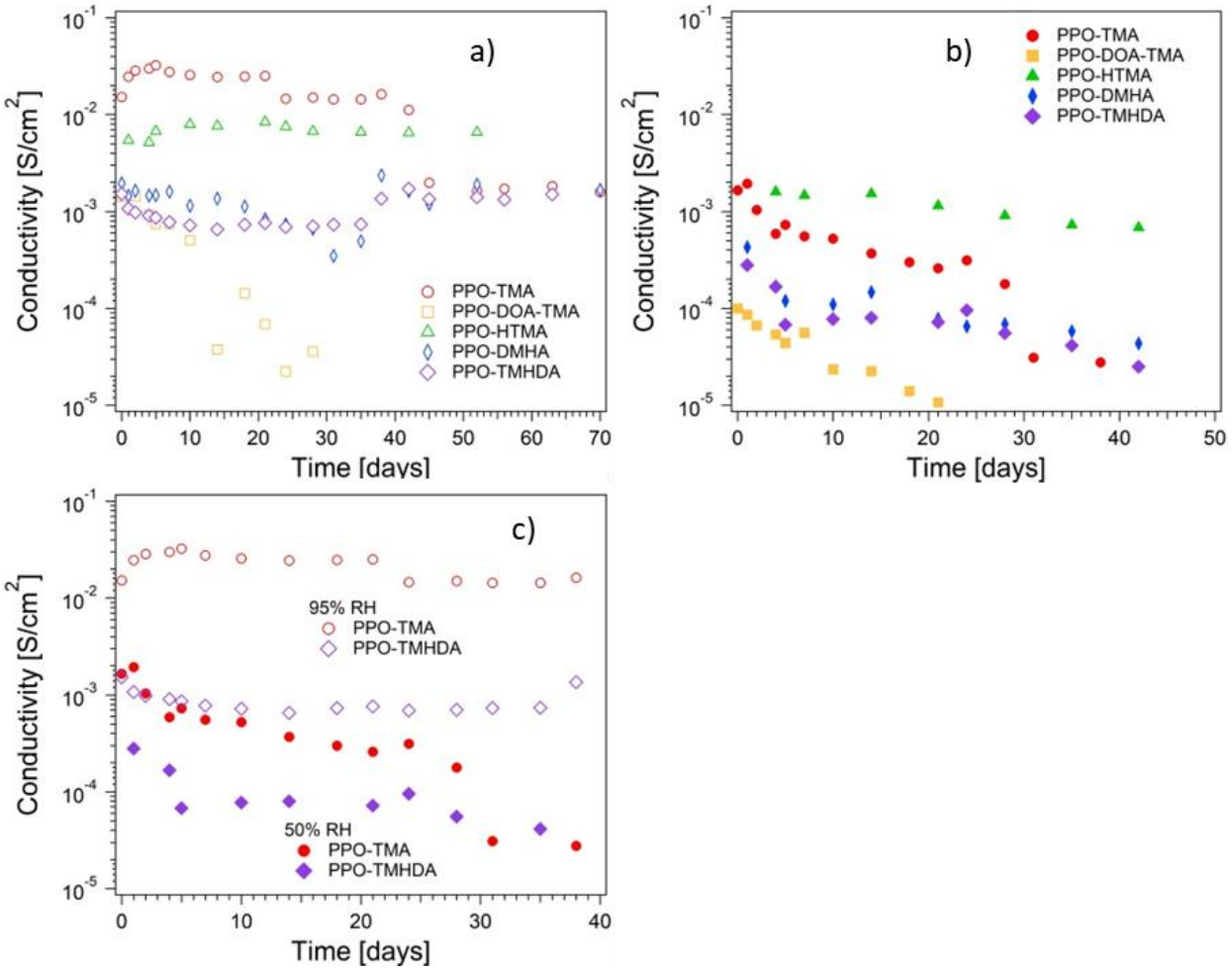

Figure 5.8: Stability of the conductivity of PPO based AEMs equilibrated with a) 1M LiCl (95% RH), b) 8M LiCl (50% RH) at 80°C and c) comparison between the stability of PPO-TMA and PPO-TMHDA membranes in high and low water activity environments.

Conclusion

Anion exchange membranes with different cation structures and the same backbone were prepared. The base and water uptake and conductivity of these membranes equilibrated with hydroxide solutions ranging from 0-10 M were studied. The water uptake, swelling ratio, conductivity, and stability properties of the hydroxide form membranes were studied. The water uptake of the membranes was also studied over a wide range of temperatures and water activities. The cations with smaller alkyl chains attached to the quaternary ammonium were observed to be more easily hydrated. In general, this lead to higher water contents, conductivities, and swelling. The water activity and temperature of the environment were shown to have a significant effect on membrane water contents only at high water activities. The stability of membrane prepared with the simplest cation structure, a nitrogen group bound to the backbone and three methyl groups (TMA) was found to depend on the distance between the backbone and the membrane. For the PPO-TMA membrane, in which the cation was directly attached to the backbone, the stability was the lowest of the membranes studied. Whereas, PPO-HTMA membrane, in which the cation was separated from the backbone by an ether group and a 6 carbon long alkyl chain, was the most stable. The stability of the membranes containing cations directly attached to the backbone with long alkyl chains extending outward (PPO-DMHA, and PPO-TMHDA) was in between the PPO-TMA and PPO-HTMA.

The results indicate that the most promising candidate for a stable AEM is likely a hybrid of the PPO-HTMA membrane, with a hydrophilic cation separated from the backbone by a long alkyl chain, and the PPO-TMHDA membrane, with crosslinking used to prevent excessive swelling and water uptake.

Catalysts Anion Exchange Ionomer Interactions

Introduction

As alluded to previously, one major concern for AEMFC polymer electrolytes is their interaction with catalysts. RDE tests conducted with precious metal catalysts and either anion exchange ionomers or organic cations in solution have demonstrated significantly lower activity than those with proton exchange ionomers[109,110,137]. This may be due to non-uniform electrodes or catalysts poisoning. RDE experiments conducted in the presence of quaternary ammonium salts demonstrated that moieties present in AEMs could be responsible for platinum poisoning; the tetramethylammonium had little impact on platinum ORR catalysis, however, the quaternary ammoniums bound to benzyl groups had a marked negative effect. Among the benzyl-bound ammoniums studied the "conventional" imidazolium performed the worst, followed by the "conventional" trimethylammonium, and "tethered" ammonium performed the best[109].

While this effect has not been studied on non-precious metal catalysts, preliminary results do not indicate any significant reduction in oxygen reduction activity. The main concern for platinum-anion exchange ionomer interactions is the for the hydrogen oxidation reaction as there are few practical options for non-precious metal HOR catalysts. The potential of zero charge on platinum is 0.55 V vs. RHE[141]. Below this potential there is a negative charge on the surface of platinum, which could attract the bulky organic cations and block catalytic sites. In order to study these ionomer-catalyst interactions the various types of anion exchange membranes were made into ionomers and incorporated into catalyst inks with carbon-supported platinum. The inks were then studied in electrochemical half-cell experiments using rotating disk electrode voltammetry.

Experimental

Materials

All solutions were prepared with DI water produced from a Millipore Milli-Q 18 Mohm 2-propanol (99.9% LC-MS CHROMASOLV grade) was obtained from Fluka analytical. Potassium Hydroxide (99.99% Semiconductor grade) was obtained from Sigma-Aldrich. Ultra-High Purity hydrogen, nitrogen, and oxygen were obtained from Airgas.

Ionomer Synthesis

Ionomers of the anion exchange membranes were formed by converting membranes to hydroxide form and dissolving in isopropanol to form a 1 wt% solution. It was not possible to dissolve the PPO-TMHDA membrane due to its crosslinked nature. Instead this material was

ground with the catalyst and suspended in the isopropanol similar to other catalyst ink preparations in the literature[142].

RDE Ink Formulation and Deposition

5 mg of 30% Pt/C (Tanaka) was combined with several drops of water to wet the catalyst. Next, 125 mg of the ionomer solution of study was added to form a 80:20 catalyst to ionomer ratio. The solution was then diluted with 1 g of IPA and ultrasonically mixed for 30 min in an ice bath. The required volume of catalyst ink required to achieve loadings of 20 $\mu g_{Pt}/cm^2$ was determined by depositing 5 µL of the catalyst ink onto a piece of aluminum foil of known mass and weighing with a Mettler Toledo XP2U Microbalance once the ink was dry. The volume of ink was adjusted and the processed repeated until the appropriate volume to reach the desired loading was determined.

The catalyst ink was then deposited onto a 5 mm glassy carbon electrode (Pine Research Instruments) which was then covered to slow the drying process. Prior to ink deposition the electrodes were prepared by polishing with 5 µm alumina slurry solution and then a 0.5 µm slurry solution. The polished electrodes were sonicated in DI water for 1 min and dried with a stream of nitrogen.

RDE Testing

RDE testing was conducted in 0.1 M KOH solutions using a Gaskatel Hydroflex reference electrode, a Pt mesh counter electrode, and jacketed glass RDE cell from Pine Research Instruments. A Pine Research Instruments rotator was used to control rotation speed and a Bio-Logic USA VMP3 multichannel potentiostat and corresponding EC Lab software was used to control the electrochemical experiments. The potential of the reference electrode was determined by measuring the OCV between the reference electrode and a clean Pt disk electrode in hydrogen saturated electrolyte.

A solution was prepared by purging with nitrogen for 30 min to ensure full removal of oxygen. The working electrode was then electrochemically cleaned by cycling between -0.2-1.4 V vs. RHE at 500 mV/s until sequential cyclic voltammograms did not change substantially (typically 50 cycles). ECSA measurements were then conducted by cycling the electrode between 0.0-1 V vs. RHE at 20 mV/s 5 times. Background ORR measurements were collected by cycling the electrode for 3 times at 20 mV/s between 0.1-1.1 V vs. RHE with the electrode static and rotating at 1600 rpm. Background HOR measurements were collected by cycling the electrode 3 times at 10 mV/s between -0.05-1 V vs. RHE with the electrode static and rotating at

2500 rpm. The electrolyte was then purged with hydrogen for 30 min and the hydrogen oxidation activity was determined by cycling the electrode as above at 0, 400, 900, 1600, and 2500 rpm. The electrode was then quickly purged with nitrogen for 5 min and purged with oxygen for 30 min. The oxygen reduction activity determined by cycling the electrode as above at 0, 625, 900, 1225, 1600, 2025, and 2500rpm.

Results and Discussion

The effect of different types of binders on the adsorption/desorption peaks of platinum is shown in Figure 5.9. All binders show a slight shifting of the hydrogen adsorption/desorption peaks towards more negative potentials compared with a binder-free electrode. The catalyst layers with anion exchange ionomers show an extra peak around 0.025-0.05V that is not present in the catalyst layers with Nafion or no ionomer. Similar peaks are evident in HOR RDE curves in the work of Kim and coworkers studying the effect of amine/ammonium presence on HOR activity on platinum catalysts[110]. This indicates these peaks are related to the adsorption of nitrogen-containing groups to the surface of the catalyst.

The HOR activities for platinum catalysts with different AEIs are shown in Figure 5.10. Electrodes with Nafion and AS4 ionomers are shown for comparison. The limiting current of the electrodes with binders is below the binder-free catalyst layer, suggesting non-uniformity in the catalyst layers[143]. This effect is most prominent in the catalyst layer containing PPO-TMHDA. Because this polymer was crosslinked it was not possible to obtain a uniform solution. The catalyst ink was therefore prepared by grinding the polymer with the catalyst and suspending in isopropanol. Given the low limiting current it is apparent that this process leads to a catalyst layer with poor platinum utilization.

Even with the binder free catalyst layer the poor HOR activity of platinum in alkaline compared to acid is evident from the overpotential compared to the Nernstian diffusion overpotential (dashed line) which is the limiting factor HOR in acidic RDE. Among the catalyst layers with binders, the AS4 and Nafion perform similar to the binder free electrode, while the PPO-TMA binder appears to have slightly increased kinetic performance. The PPO-DOA, PPO-HTMA, and PPO-DMHA binders all have reduced kinetic performance. Normalizing the curve to the same limiting current density as the other electrodes shows that the kinetics are not significantly impacted; therefore the poor performance is likely a result of poor catalyst layer uniformity rather than catalyst poisoning.

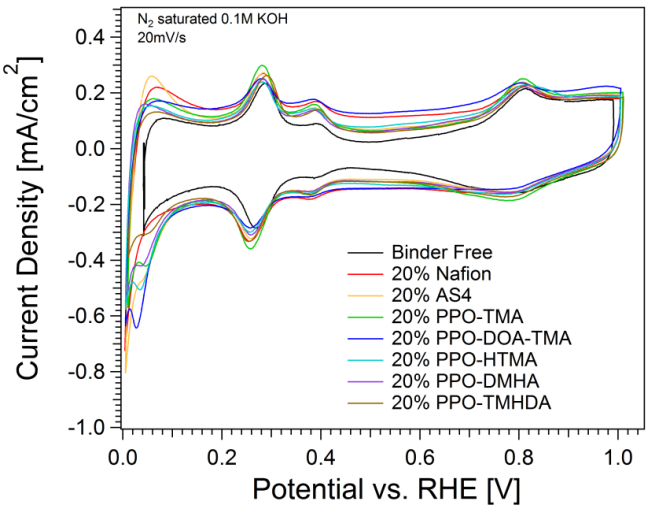

Figure 5.9: Cyclic Voltammograms for Pt/C catalysts with different binders.

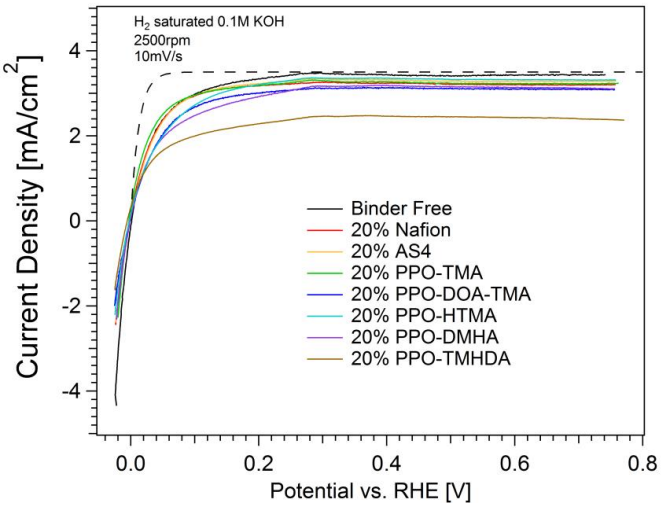

Figure 5.10: RDE plots for the HOR on platinum with different binders

The ORR activity of platinum catalysts with AEIs is shown in Figure 5.11. As with the HOR, the diffusion limited current density is impacted by the inclusion of binders within the catalyst layers, especially for the PPO-TMHDA. A closer examination of the kinetic region shows that the binder free electrode has the best activity, closely matched by the PPO-TMA. The PPO-DOA-TMA has the largest negative effect on ORR activity.

The various catalyst layer metrics are given in Table 5.2.

Conclusions

Altogether, the performance of catalyst layers with different anion exchange binders were not as significantly affected as may have been suggested by RDEs conducted in the presence of organic cations similar to those used in the AEMs. The use of anion exchange ionomer lead to a pronounced effect on the catalyst layer uniformity as evidenced by the low diffusion limited current densities compared to the binder-free electrode. The observed catalyst layer non-uniformity could be due to the well-known tendency of cationic charges to form agglomerations in solutions. Normalizing the HOR and ORR curves to the expected diffusion limited potential revealed little difference in the kinetic region, i.e. above 0.9V for ORR and below 0.1V for HOR, for the various binders used.

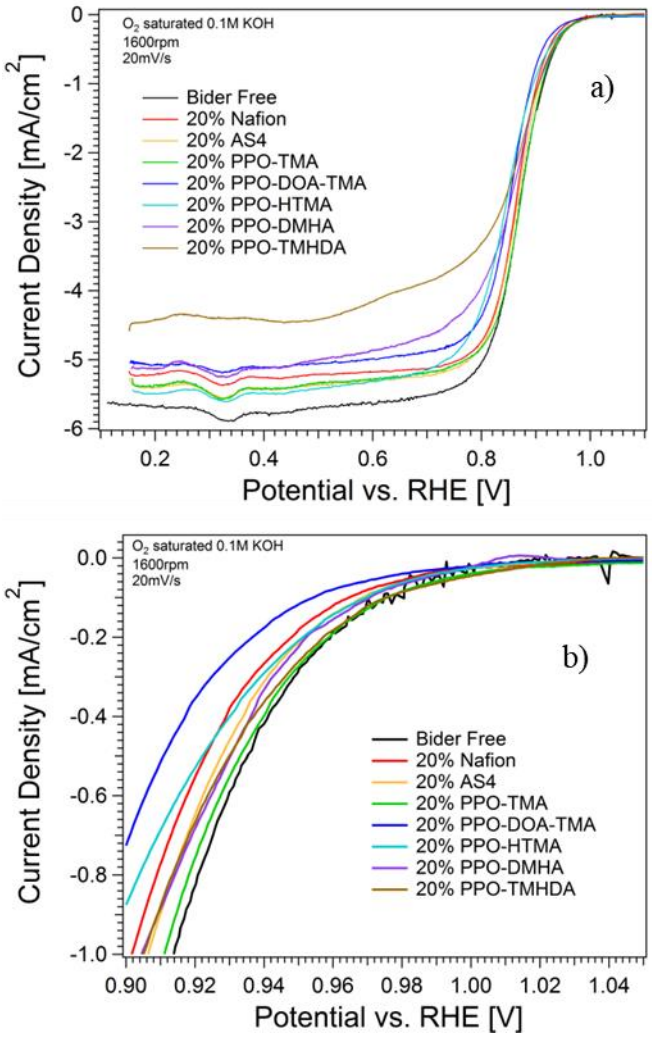

Figure 5.11: RDE plots for the ORR on platinum with a) whole range and b) Kinetic region

Table 5.2: ORR RDE parameters for catalyst layers with different binders in 0.1M KOH

Ionomer	ESCA [m^2/g_{Pt}]	I_m [A/g_{Pt}]	I_s [A/m^2_{Pt}]	JL [mA/cm^2]
None	36.2	92.9	2.57	5.69
Nafion	29.5	65.3	2.21	5.26
AS4	36.9	76.7	2.08	5.42
PPO-TMA	40.6	93.1	2.29	5.35
PPO-DOA-TMA	26.9	43.2	1.60	5.11
PPO-HTMA	31.2	53.9	1.73	5.49
PPO-DMHA	32.8	63.1	1.93	5.12
PPO-TMHDA	36.6	74.0	2.02	4.45

Electro-Osmotic Drag of Water in Tokuyama's A201 Anion Exchange Membrane

Introduction

To date most studies of anion exchange membranes have focused on improving stability and conductivity. Meanwhile, relatively little attention has been paid to other properties which will be important to understand the performance of fuel cells, such as water transport and carbonate effect on water content and uptake. More information on these properties is critical for further development of AEMFC technology.

In the early days of proton exchange membrane fuel cell research it was observed how critical proper water management is to achieving high performance. Failure to remove the produced water from the cathode will quickly lead to blocking of the catalytic site resulting in severe performance loss. However, the conductivity of the proton exchange membranes is dependent on the water content within the membranes, so insufficient cell hydration will lead to ohmic losses. The issue of water management is made more difficult by competing diffusive and electro-osmotic water transport during operation.

The need to study water transport in AEMFCs is even more critical than for PEMFCs for several reasons. Firstly, the chemical stability of anion exchange membranes continues to be of concern and it is well known that the degradation occurs quicker at lower water contents. Secondly, unlike PEMFCs water is both a reactant and a product in AEMFCs.

In PEMFCs, as the protons migrate from the anode to the cathode they drag water molecules. This electroosmotic drag as well as the electrode processes result in the accumulation of water at the cathode. Some of the water will diffuse back toward the PEM towards the anode due to the concentration gradient while the rest is evacuated through the cathode exhaust.

In AEMFCs, water is consumed at the cathode, requiring that there be significant back diffusion from the anode or that the cathode gas feed be humidified. As the hydroxide is transported through the AEM to the anode it drags water molecules along. More water is produced from the anode reaction in AEMFCs than from the cathode reaction in PEMFCs; this leads to a large accumulation of water at the AEMFC anode. Some of the water will diffuse back to the cathode, while the rest will need to be collected and removed from the anode. Because the anodes of polymer membrane fuel cells are typically closed systems, a method to remove water from the anode stream will need to be devised.

Therefore the electrodes will have to be designed to optimize the water transport. The development of a water transport model for AEMFCs similar to those produced for PEMFCs would be instrumental in this regard. To this end there are still several key knowledge gaps which must be studied.

One key parameter of water transport in polymer electrolyte membranes which has received very little attention in AEM research is the electro-osmotic drag of water by the hydroxide ions as they move from the cathode to the anode. In proton exchange membranes the electro-osmotic drag (EOD) has been studied by several groups with different methods. Peng et al give a succinct summary of the various methods and their respective limitations[144].

In AEMs there are very limited reports on EOD measurements. Molerino's group has used an in-situ method to measure the EOD in fully hydrated Tokuyama's A201 at different temperatures[145]. The electro-osmotic drag coefficient $\boldsymbol{\varepsilon}$ was found to be ~0.7 water molecules per anion at room temperature which increased to ~1.25 at 55°C. Based upon the technique used, it would not be possible to use this method for membranes which are not fully hydrated. Therefore, it is unclear how the results would compare to a realistic cell. The value observed at room temperature was close to the value observed by Fedkiw's group using the Fuller-Newman concentration cell method to study the EOD in the same membrane[146]. Using this method $\boldsymbol{\varepsilon}$ was observed to be constant 0.6 over a wide range of relative humidity. It is unclear given the described methodology for both reports whether the AEM was exposed to the atmosphere and thus in a mixed hydroxide/carbonate form. This may be helpful in determining $\boldsymbol{\varepsilon}$ under real world conditions in which the membrane is expected to be constantly exposed to carbon dioxide. However, it is critical to study the membrane in both its pristine hydroxide form and fully converted carbonate/bicarbonate form to understand how each ion will contribute to water transport in AEMs. This knowledge will bring us one step closer to the development of a comprehensive model of water transport in AEMs.

To this end, the EOD has been studied in Tokuyama's A201 membrane in pure hydroxide and carbonate forms. The Fuller-Newman[147] style concentration cell was used for this study as it allows for the determination of $\boldsymbol{\varepsilon}$ over a wide range of membrane water content and removes contributions from diffusion which are present in in-situ methods. To study the pure hydroxide form, membrane pretreatment cell assembly were conducted in a CO_2-free glovebox.

Experimental

A201 anion exchange membranes, provided in hydroxide form by Tokuyama Corporation, Japan, were used for all measurements in this study. Sodium hydroxide (1 M Certified), Potassium hydroxide (ACS grade), Lithium Chloride (ACS grade) and Sodium Chloride (ACS grade) were obtained from Fisher Scientific. 2-propanol (IPA) LC-MS Chromasolv® grade was obtained from Fluka Analytical. 18 MΩ cm DI water was produced using a Milli-Q® water filtration system.

Membrane preparation

Membranes were exchanged from one ion form to another (e.g. OH^- to HCO_3^- form, OH^- to Cl^- form) by soaking the membrane in a 1 M solution of the desired sodium/potassium salt for 24 hr. Subsequently, the exchanged membranes were transferred to DI water for 24 hr with at least 2 exchanges of solution to remove the excess salt. All OH^- form membrane preparation was conducted in a N_2 filled glove box to prevent CO_2 contamination, while the HCO_3^- form and Cl^- form membranes were prepared in the ambient atmosphere.

Electro-osmotic Drag Coefficient

A catalyst ink was prepared by dispersing 58.8% $Pt_{0.5}Ru_{0.5}$/C (ETEK) in a H_2O/IPA mixture to form a 1 wt% solution. The ink was spray painted onto both ends of a strip of Tokuyama A201 anion exchange membrane to achieve a ~1 mg_{PtRu}/cm^2 loading. The membrane was then converted to either hydroxide or bicarbonate form and assembled into the EOD cell as shown in Figure 5.12 with Toray paper gas diffusion layers and a platinum wire leading out of the cell to monitor the potential difference. The desired LiCl solutions were then placed in the wells below the membrane before bolting the cell together. Hydrogen was passed through both sides of the cell at equal rates after humidifying by bubbling through LiCl solutions with the same concentration as the respective sides of the cell.

The cell potential was monitored daily until there was no observed change. The cell was then disassembled and the LiCl solution on the variable side was changed. For hydroxide form membrane, changing the LiCl solution was conducted in the glovebox.

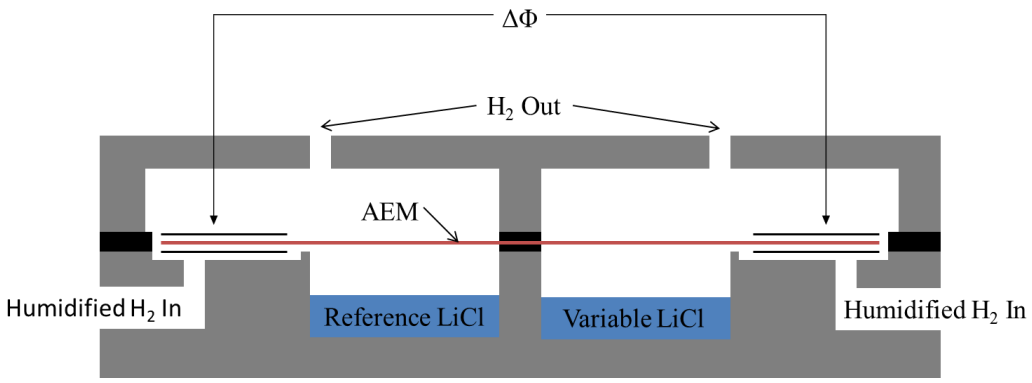

Figure 5.12: Electro-osmotic drag cell schematic.

Results and Discussion

The cell design and concept for electro-osmotic drag coefficient measurements follow from the work of Fuller and Newman. Rather than force the motion of protons (PEMs) or hydroxide (AEMs) and try to measure the movement of water, this method involves establishing a water activity gradient over the membrane and measuring the change in proton/hydroxide activity by monitoring the potential difference between two reversible hydrogen electrodes. The electrochemical system is described by:

$$\underset{\alpha}{\text{PtRu/C (s), } H_2 \text{ (g)}} \;/\; \underset{\beta}{\text{A201 } (\lambda_\beta)} \;/\; \text{transition region} \;/\; \underset{\gamma}{\text{A201 } (\lambda_\gamma)} \;/\; \underset{\delta}{\text{PtRu/C (s), } H_2 \text{ (g)}}$$

Where the relevant half reaction is:

$$\frac{1}{2}H_2 + OH^- \leftrightarrow H_2O + e^- \qquad [5.8]$$

Therefore the cell potential is:

$$F\Delta\Phi = \mu_{e-}^{\alpha} - \mu_{e-}^{\delta} \qquad [5.9]$$

Where F is Faraday's constant, μ_{e-}^{α} and μ_{e-}^{δ} are the chemical potentials on the left and right sides of the cells, respectively, and ΔΦ is the cell electrostatic potential.

Since each side of the cell is in equilibrium the electrochemical potential of each side of the cell can be described by

$$\frac{1}{2}\mu_{H2} + \mu_{-} = \mu_O + \mu_{e-} \qquad [5.10]$$

With the "-" subscript representing hydroxide and the "O" subscript representing water.

Rearranging [5.10] for μ_{e-} and plugging into [5.9] gives:

$$F\Delta\Phi = \frac{1}{2}RTln(P_{H2}^{\alpha}) - \frac{1}{2}RTln\left(P_{H2}^{\delta}\right) + \int_{y\delta}^{y\alpha} \nabla\mu_{-}dy - \int_{y\beta}^{y\gamma} \nabla\mu_{O}dy \quad [5.11]$$

Or, assuming equivalent partial pressures of hydrogen on both sides of the cell

$$F\Delta\Phi = \int_{y\delta}^{y\alpha} \nabla\mu_{-}dy - \int_{y\beta}^{y\gamma} \nabla\mu_{O}dy \quad [5.12]$$

The establishment of a water activity gradient leads to diffusion within the transition region, which can be described by the Maxwell-Stefan multi-component diffusion equation modified for concentrated electrolytes:

$$c_i\nabla\mu_i = \sum_j K_{ij}(v_j - v_i) \qquad K_{ij} = K_{ji} \quad [5.13]$$

Where c_i, μ_i, and v_i are the concentration, chemical potential, and velocity of species i, K_{ij} is the friction factor between species i and j, and v_j is the velocity of species j. In this system, three components are present; water (subscript "o"), membrane (subscript "m"), and hydroxide (subscript "-").

By defining

$$M_{ij} = M_{ji} = K_{ji} \qquad \& \qquad M_{ii} = \sum -K_{ji} \quad [5.14]$$

And rearranging [5.13] gives:

$$c_i\nabla\mu_i = \sum_j M_{ij}(v_j - v_i) \quad [5.15]$$

Inverting the equations gives the corresponding velocity equations in terms of chemical potentials.

$$L^m = (M^m)^{-1} \quad [5.16]$$

$$v_j - v_m = -\sum_j L_{jk}^m(c_k\nabla\mu_k) \quad j \neq m \quad [5.17]$$

Where M^m is the submatrix obtained by defining the membrane as the reference and deleting that row and column from the matrix.

The electro-osmotic drag coefficient (ε) is described the number of water molecules transferred for each hydroxide molecule:

$$\varepsilon = \frac{N_O}{N_-} = \frac{c_O v_O}{c_- v_-} \quad [5.18]$$

From [5.17]

$$N_O = c_O v_O = -L_{OO}c_O^2\nabla\mu_O - L_{-O}c_O c_-\nabla\mu_- \quad [5.19]$$

$$N_- = c_- v_- = -L_{-O}c_O c_-\nabla\mu_O - L_{--}c_{\pm}^2\nabla\mu_- \quad [5.20]$$

From the definition of conductivity:

$$L_{--} = \frac{\kappa}{F^2 c_{\pm}^2} \quad [5.21]$$

For a uniform solution:

$$\nabla\mu_k = z_k\Delta\Phi \quad [5.22]$$

[5.18] then, becomes:

$$\varepsilon = \frac{N_O}{N_-} = \frac{(-L_{OO}c_O^2 z_O - L_{-O}c_O c_- z_-)\Delta\Phi}{(-L_{-O}c_O c_- z_O - L_{--}c_-^2 z_-)\Delta\Phi} = \frac{L_{-O}c_O c_-}{L_{--}c_-^2} = \frac{L_{-O}c_O c_-}{c_-^2} * \left(\frac{\kappa}{F^2 c_-^2}\right)^{-1} \quad [5.23]$$

Or, rearranging

$$L_{-O} = \frac{\varepsilon\kappa}{F^2 c_- c_O} \quad [5.24]$$

In the cell described above, the flux of anions (N-) is zero, therefore:

$$N_- = 0 = -L_{-O}c_O c_- \mu_O - L_{--}c_-^2 \mu_- \Rightarrow -\frac{\varepsilon\kappa}{F^2 c_- c_O} c_O c_- \mu_O = \frac{\kappa}{F^2 c_-^2} c_-^2 \mu_- \quad [5.25]$$

and

$$\mu_- = -\varepsilon\mu_O \quad [5.26]$$

Now [5.12] becomes:

$$F\Delta\Phi = \int_{y\delta}^{y\alpha} \nabla\mu_- dy - \int_{y\beta}^{y\gamma} \nabla\mu_O dy = \int_{y\gamma}^{y\beta} (1+\varepsilon)\nabla\mu_o dy \quad [5.27]$$

Upon differentiating:

$$F\Delta\Phi = 2.3RT(1+\varepsilon) log \frac{P_O^\gamma}{P_O^\beta} \quad [5.28]$$

Solving for the electro-osmotic drag coefficient gives:

$$\varepsilon = \frac{F}{2.3RT} \frac{\Delta\Phi}{log P_O^\gamma / P_O^\beta} - 1 \quad [5.29]$$

Plotting the dimensionless cell potential in terms of F/2.3RT versus the log of the change in water activity and subtracting one will give the electro-osmotic drag coefficient in anion exchange membranes.

The values observed in our test conducted with the hydroxide form membrane differ significantly from these prior reports. Figure 5.13 shows a plot of the dimensionless measured cell potential vs. the logarithm of the difference in water activity between the different sides of the cell for the A201 membrane in pure hydroxide form. The water uptake of A201 over a wide range of relative humidity and temperatures has been discussed in our previous work[148]. The 2 runs conducted gave generally good agreement. Two distinct regions are observed for higher ($8<\lambda$) and low ($8>\lambda$) water contents.

In the high water content region, the hydroxide drags along over 8 water molecules as it moves across the membrane, while at low water contents the membrane the value is closer to ~2.5. Given the well-known issues regarding AEM stability, it may be expected that subjecting the membrane to the low water activities used in this test resulted in degradation, which would affect the measurement at lower water activities. However the measured conductivity of the membrane (in chloride form) before and after testing showed little change, indicating membrane degradation is not a great concern.

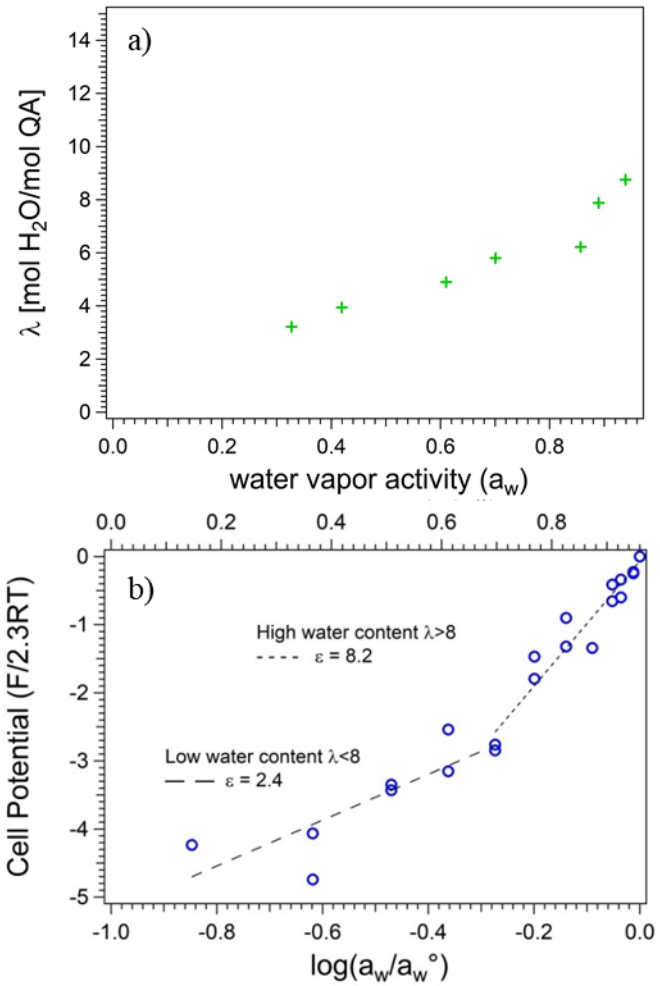

Figure 5.13: Dimensionless cell potential, a), and membrane water content, b), as a function of the water vapor activity for A201 membrane in hydroxide form.

For polymer electrolyte systems it is well known that increasing water contents are associated with swelling of the hydrophilic ion conduction pathways in the membrane. It is not surprising that the increase in water content leads to the water being "freer" in the well hydrated system resulting in higher electro-osmotic drag. In previous work, measuring the carbonate ion self-diffusion coefficient in A201 membranes we have observed a similar change difference between high and low water content membranes[148].

These results clearly demonstrate why AEMFCs suffer from significant anode flooding. If a standard 5 cm^2 cell operating at 80°C is fed with 200 ml/min of fully humidified hydrogen then, given the water vapor saturation pressure, ~1 mg/s of water is delivered to the electrode. If the cell is operating at 1 A/cm^2 another ~1 mg/s of water would be generated from the electrode reaction, and 8 mg/s would be delivered from electro-osmotic transport. The electro-osmotic transport of water in hydroxide membranes is therefore responsible for delivering significantly more water to the electrode than the gas stream and the electrode reaction combined. This also indicates that significantly more water is transported away from the cathode than can be replaced with the oxidant gas feed when operating at high current densities. Therefore AEMs should be made as this as possible to increase the back-diffusion from the saturated anode.

The data for the EOD measurements using the bicarbonate form membrane are shown in Figure 5.14. Here, again, there are two distinct regions. At high water contents $\boldsymbol{\varepsilon}$ is calculated as 0.3 water molecules per carbonate ion which is significantly lower than the value obtained for the hydroxide form membrane. At low water contents $\boldsymbol{\varepsilon}$ increases to 1.8. It is possible that as water content in the membrane is lowered the increase in pH results in the partial conversion of carbonate back to hydroxide, thereby increasing the $\boldsymbol{\varepsilon}$.

Figure 5.15 compares the measured EOD results for the hydroxide and bicarbonate form A201 membrane in this study as well as the data reported by Wang et al[146]. The results of the latter are fairly consistent with the bicarbonate form membrane except at the lowest water activities. For the present study, the cells were allowed to equilibrate for longer periods of time before measuring the cell potential (3 days as opposed to 1 for Wang et al.). It is known that membrane equilibration with water vapor is a slow process[149], and this may account for the discrepancy between the studies.

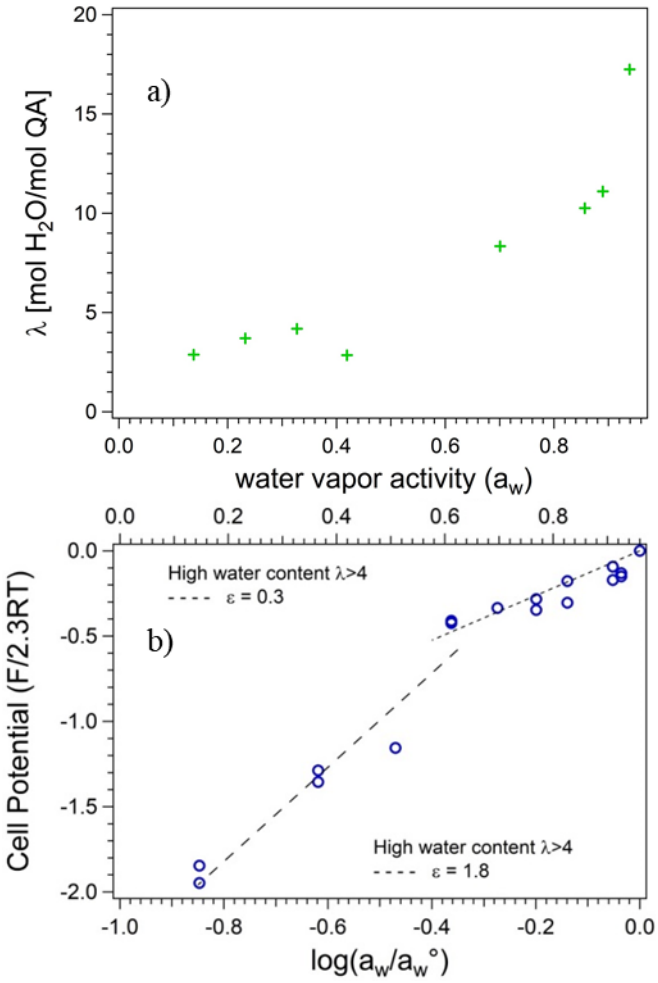

Figure 5.14: Dimensionless cell potential, a), and membrane water content, b), as a function of the water vapor activity for A201 membrane in bicarbonate form.

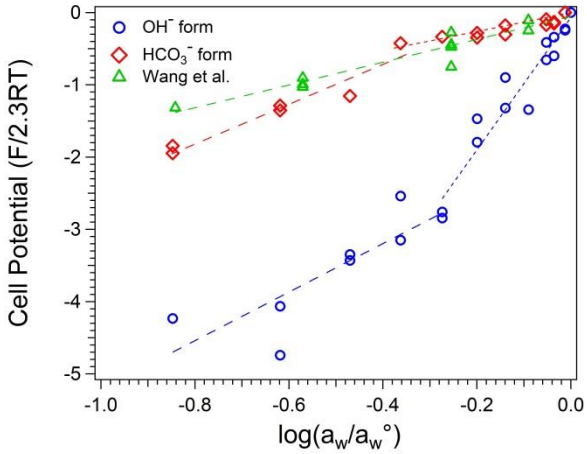

Figure 5.15: Dimensionless cell potential and water content as a function of the water vapor activity for A201 membrane in bicarbonate form

The electro-osmotic drag coefficient is significantly higher for the pure hydroxide form membrane than for the carbonate form membrane. The presence of carbonate in AEMs is widely known to reduce the conductivity, and therefore increase the resistance losses in AEMFCs. However, the hydroxide ion is significantly more reactive with regard to the cations in the AEM than the bicarbonate/carbonate ions are. Therefore operating the AEMFC in carbonate form would be expected to increase stability[119]. Interestingly, Unlu et al observed that the inclusion of carbon dioxide in the oxygen feed actually significantly improved cell performance[150]. In light of the results given here it is probable that the AEMFC operated in carbonate form would suffer less from anode flooding. Further work will be required to validate this hypothesis.

Conclusions

The electro-osmotic drag of water by anion in AEMs is an important parameter to understanding water transport in AEMFCs and managing fuel cell operation. However, there have been few studies on this parameter in the literature, and those available are potentially flawed in their experimental methodology. In PEMFC research an important step was the development of a model of water transport in an operating fuel cell made capable by understanding the ion conductivity, water diffusivity, and electro-osmotic transport in the membrane in electrodes. Similar attempts have made for AEMFCs[151,152]. In these reports the electro-osmotic drag is determined by a fit to the experimental data of Li et al[153]. However, Li et al. only studied the electro-osmotic drag in AEMs at high water contents and using an in situ method, in which contributions from diffusive effects cannot be prevented. Furthermore, the membrane was only studied it is unclear in which ion state, hydroxide, (bi)carbonate, or mixed, the membrane was. Therefore, the utility of these results in modeling water transport in AEMFCs is suspect. In this work the electro-osmotic transport of water in AEMs is described for both the pure hydroxide and bicarbonate forms over a wide range of water contents, which will aid further attempts to model water transport in AEMFCs.

Chapter 6: Anion Exchange Membranes for Zinc-Air Batteries

Introduction

Metal Air batteries have been gaining increased attention in recent years due to the substantially higher energy density. Primary (non-rechargeable) zinc-air batteries (ZABs) have been commercially available for decades, mainly as button cells. These batteries typically use a caustic electrolyte and a porous polymer separator and operate at low current densities <10 mA/cm2. A later section of this work will focus on the development of electrodes for zinc air batteries (ZAB) and the related zin peroxide battery (ZPB). This section focuses on the development of membrane separators.

The use of anion exchange membranes as the separators in zinc batteries has several advantages. First, the membranes will have higher conductivities than porous polymer separators, reducing the resistance losses as higher currents are achieved. Second, the membranes can act as a hydroxide reservoir, due to higher solution uptakes.

Anion exchange membranes were researched for use as separators in alkaline rechargeable zinc-air batteries. Current separators used in the market are typically comprised of microporous polymer composites, such as Celgard®. These separators prevent shorts caused by dendrite growth from the zinc to air electrode. By replacing the separator with an anion exchange membrane it was believed that the cell resistance could be reduced through increased electrolyte conductivity while still providing a barrier to dendrite growth. An early report of AEMs for ZAB separators claimed to negate zinc crossover through Donnan exclusion, however this is unlikely since the soluble zinc species in alkaline electrolytes is the zincate anion. AEMs for ZABs should demonstrate high conductivity in concentrated alkaline solution, long term stability at room temperature, resistance to dendrite formation, and mechanical stability.

Typically 6 M KOH is used as the electrolyte in alkaline zinc air batteries because it optimizes the kinetics of the zinc and air electrodes and near the peak conductivity. Zinc peroxide batteries are typically tested in lower hydroxide concentration solutions.

In all cases in this chapter the membranes were synthesized by collaborating researchers.

Traditional AEMS for ZABs

Introduction

Initial studies into separators for zinc air batteries focused on traditional anion exchange membranes developed for AEMFCs. Two collaborating groups provided AEMs based on

different backbone structures, polystyrene and polypropylene. The effect of crosslinking, cation structure, and polymer structure on conductivity, uptake, and stability.

Experimental

Materials

All solutions were prepared with DI water produced from a Millipore Milli-Q 18 Mohm. Certified 1N HCl was obtained from Fisher Scientific for titrations. Sodium chloride and potassium hydroxide (ACS grade) were obtained from Fisher Scientific. The anion exchange membranes were obtained from collaborating researchers.

Uptake and Conductivity of AEMs in Hydroxide Solutions

The swelling ratio, base and water uptake, and ionic conductivity of membranes saturated of potassium hydroxide solutions ranging from 0-10 M and at different relative humidifies were measured in order to build a detailed picture of the behavior of the AEM in a basic medium.

The swelling ratio is a measure in the dimensional changes associated with saturation in solution; it is an indication of the dimensional stability of the membrane under operating conditions. A low swelling ratio is desired for ease of producing the membrane electrode assembly (MEA) and to ensure its mechanical stability. Water content in AEMFCs must be carefully managed. High water uptake may aid in ionic conductivity but can also negatively affect mechanical properties of the MEA, while a low uptake will result in higher reactivity of the hydroxide ion and faster degradation.

Each membrane was placed in potassium hydroxide solutions for 24 hr to fully equilibrate. The conductivity, dimensions, and mass of the saturated membranes were measured. The membranes were then ion exchanged in sodium chloride solutions, thoroughly rinsed and dried. The hydroxide content of the sodium chloride solutions was determined using a Mettler Toledo DL15 autotitrator and hydrochloric acid as a titrant. After drying the mass of the membranes was determined.

The base uptake and water content and swelling ratios (BU, WC, & SR) were determined by:

$$\mathrm{BU} = \frac{\text{moles } OH^-}{m_{dm}} \quad [6.1]$$

$$\mathrm{WC} = \frac{(m_{sm} - \text{moles } OH^- * M_{KOH} - m_{dm})}{M_{H2O} * (\frac{IEC * m_{dm}}{1000})} = \frac{\text{moles } H_2O}{\text{moles QA}} \quad [6.2]$$

$$\mathrm{SR} = \frac{\text{Length of Saturated Membrane}}{\text{Length of Dry Membrane}} \quad [6.3]$$

Where moles OH^- was determined from the titration, m_{dm} is the dry mass of the membrane, m_{sm} is the mass of the saturated membrane, M_{KOH} is the molar mass of KOH, M_{H2O} is the molar mass of water.

The conductivity was determined using potentio-electrochemical impedance spectroscopy (PEIS). Briefly, the equilibrated membrane was removed from solution, the excess solution was wiped away, and the membrane was placed in a 4 electrode conductivity cell. The membrane resistance was measured by applying a PEIS sweep from 10^5 to 1 Hz and circle fitting the resultant Nyquist plot to determine the high frequency resistance. The width and thickness of the membrane were then measured and the conductivity determined with the equation:

$$\sigma = \frac{L}{R*T*W} \quad [6.4]$$

Where R is the high frequency resistance determined from the Nyquist plot, W and T are the average width and thickness and L is the distance between the cell's two inner electrodes.

Stability

In order to probe the stability of the AEMs, each membrane was submersed in high molarity (8 M) hydroxide solutions at an elevated temperature (60°C). The conductivity of the membrane was monitored over time in order to determine any loss in the membrane's ability to transport hydroxide.

Results

AEMs based on Polystyrene

Commercial polystyrene was modified through a chloromethylation process to attach a chloride group to the aromatic ring; the process was controlled to achieve 44% of repeat units functionalized. Crosslinked polystyrene AEMs were produced by reacting the chloromethylated polystyrene with tetramethyldiamino alkanes of varying lengths. The amines replaced the chloride groups at each end forming the quaternary ammoniums and resulting in a chemical link between polymer chains. A representative visual diagram of the PS AEMs is shown in Figure 6.1. The degree of crosslinking in the AEMs was sufficiently high to produce insoluble membranes. In some cases a portion of the chlorides were replaced with tertiary monoamines to reduce the degree of crosslinking without reducing the number of ionic groups.

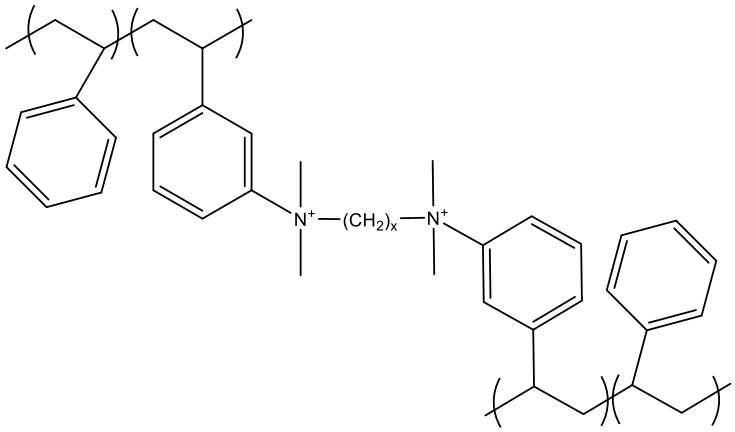

Figure 6.1: Structure of crosslinked PS-AEMS where x=1 for PS-DC1, x=3 for PS-DC3, and x=6 for PS-DC6

The solvent used for the synthesis and casting of the polystyrene based AEMs was determined to have a dramatic impact on the performance of the anion exchange membranes. For this study, toluene and dimethylformamide (DMF) were used to produce otherwise equivalent membranes. The conductivities, water uptake, and decay time for crosslinked PS-AEMs with different crosslinker lengths are given in Table 6.1.

The toluene cast membranes were typically brittle compared to those cast from DMF. The conductivities and water uptake of toluene cast membranes were a factor of 10 and 4, respectively, lower than equivalent membranes cast from DMF. The toluene cast membranes were also significantly less stable in 8 M KOH than DMF cast membranes. Solvent effects have also been observed in proton exchange membranes. In this case the dramatic change in properties may be due to the specifics of the solvent parameters. DMF was chosen for the rest of the work with PS-AEMs

The molecular weight of polymers had a significant effect on the material properties such as glass transition temperature, crystallinity, and tensile strength. PS membranes were synthesized with a high and low molecular weight; the properties of the AEMs produced with each are shown in Table 6.2

The low molecular weight AEMs had conductivities and water uptakes nearly double that of the higher molecular weight samples. There was not a consistent effect of molecular weight on the stability of the AEMs. The longer polymer chains would be expected to have increased Van der Waals forces, limiting the motion. The higher solution uptakes and conductivities are then likely the result of increased chain mobility and membrane plasticity.

Table 6.1: Effect of synthesis and casting solvent on conductivity, water uptake, and amount of time the membrane survived in 8 M KOH at 60°C for the polystyrene AEMs

Membrane	Solvent	Time [Days]	WU (%)	σ [mS/cm]
PS-DC3	DMF	2	67.0	7.5
	Toluene	--	15.2	0.2
PS-DC6	DMF	49	186.0	77.2
	Toluene	6	20.5	7.9

Table 6.2: Effect of molecular weight on conductivity, water uptake, and amount of time the membrane survived in 8 M KOH at 60°C for the polystyrene AEMs

Membrane	Mn	Time [Days]	WU (%)	σ [mS/cm]
PS-DC3	23k	2	67.0	7.5
	70k	3	49.0	4.8
PS-DC6	23k	49	186.0	77.2
	70k	--	98.0	37.9

The effect of the crosslinker length was investigated. It was expected that the longer chains would allow for greater chain separation and therefore higher water uptakes. The properties of membranes produced with 1, 3, and 6 carbon linkages are shown in Table 6.3.

The conductivity, stability, and water uptake all increased dramatically with chain length. The AEMs synthesized with 1 carbon ion crosslinkers were too brittle to measure the conductivity. This trend is likely explained by increasing solvation of the quaternary ammonium groups with increasing crosslinker length. It is which is generally accepted that the conductivity and stability of AEMs decreases dramatically at low water activities where the quaternary ammonium groups are not fully solvated. Steric hindrance caused by the close proximity of the polymer chains in short crosslinker AEMs likely prevents the full hydration of the quaternary ammonium groups.

For some PS-AEMs a portion of the chlorinated groups were replaced with mono-amines which did not result in crosslinking. Several alkyl chain lengths were used to determine the effect on conductivity and stability. The monoamines used were trimethylamine (TMA), dimethylbutylamine (DMBA), and dimethyloctylamine (DMOA) corresponding with chain lengths of 1, 4, and 8, respectively (refer to R in Figure 6.2). The properties for these AEMs are displayed in Table 6.4.

Table 6.3: Effect of crosslinking agent length on conductivity, water uptake, and amount of time the membrane survived in 8 M KOH at 60°C for the polystyrene AEMs

Membrane	Time [Days]	WU (%)	σ [mS/cm]
PS-DC1	--	9.4	--
PS-DC3	2	67.0	7.5
PS-DC6	49	186.0	77.2

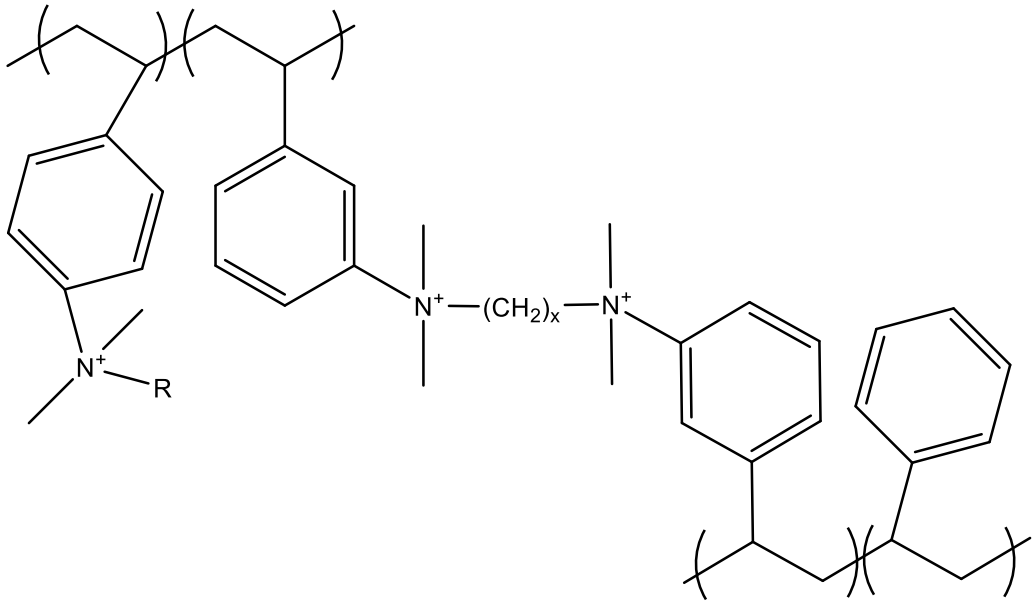

Figure 6.2: Structure of crosslinked PS-AEMS with monoamines where R=1 for TMA, R=4 for DMBA, and R=8 for DMOA

Table 6.4: Effect of monoamine addition on conductivity, water uptake, and amount of time the membrane survived in 8 M KOH at 60°C for the polystyrene AEMs

Membrane	Mn	Time [Days]	WU (%)	σ [mS/cm]
PS-DC3	20k	--	--	3.7
PS-DC3-TMA	20k	--	--	30.6
PS-DC3-DMBA	20k	--	--	20.1
PS-DC3-DMOA	20k	--	--	21.2
PS-DC6	23k	49	186.0	77.2
	70k	1	98.0	37.9
PS-DC6-TMA	23k	2	596.0	133.3
	70k	49	731.0	152.3

As seen with the crosslinked-only membranes the stability of AEMs with 6-chain-crosslinkers was much greater than for 3-chain-crosslinkers. The water uptakes of the membranes with monoamines were significantly higher. This result was anticipated since the addition of the monoamine results in a lower number of crosslinking sites, thereby allowing for greater membrane swelling and higher uptakes. The conductivity of the mono-amine membranes was also significantly higher, by at least a factor of 2, than the AEMs with only crosslinking. The conductivity of the membranes long alkyl chain amines (DMBA and DMOA) were only 2/3 that of the membrane with the trimethylamine. The effect of the inclusion of the TMA in DC6 crosslinked membranes on stability was unclear.

AEMs based on Poly(phenylene oxide)

PPO AEMs were produced through the quaternization of brominated PPO, which was prepared by collaborating researchers or commercially. The degree of bromination was controlled to attain a degree of functionalization of either 40% or 60% of repeat units. An idealized synthesis scheme is represented by Figure 6.3.

Table 6.5 shows the properties of several PPO based AEMs studied. As expected the increased degree of functionalization increased the water uptake and conductivity for each type of amine. The long-alkyl chain amines became water soluble at high degrees of functionality in dilute KOH solutions; possibly due to the disruption of the crystallinity from the long alkyl chain. Interestingly, the stability of the membranes with higher degrees of functionalities appeared to be significantly lower.

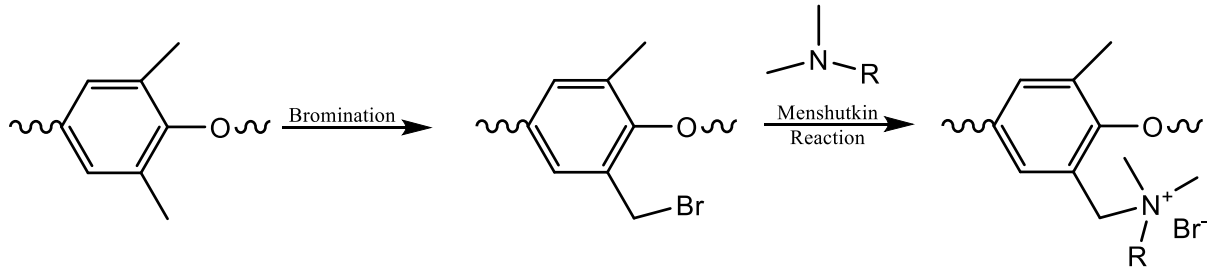

Figure 6.3: Synthesis scheme for PPO based AEMs R=CH^3 for TMA, $(CH^2)^5CH^3$ for DMHA, and $(CH^2)^9CH^3$ for DMDA

Table 6.5: Effect of cation structure on conductivity, water uptake, and amount of time the membrane survived in 8 M KOH at 60°C for the poly(phenylene oxide) AEMs

Membrane	DF [%]	Time [Days]	WU [%]	σ [mS/cm]
PPO-TMA	40	39	13.7	4.89
	60	23	28	15.76
PPO-DMHA	40	51	8.2	0.16
	60	2	18.6	4.67
PPO-DMDA	40	58	15.9	0.16
	60	20	N/A	4.07

Conductivity of AEMs in KOH Solutions

As can be seen in Figure 6.4a the conductivity of PPO based AEMs in alkaline solution shows similar trends to that of PEMs in acidic media; i.e. the membrane conductivity increases at low electrolyte concentrations but diminishes in solutions >1 M. The crosslinked PS based AEMs however showed a different trend where the peak conductivity is shifted to ~3 M. The significantly higher conductivities of the PS based AEMs are likely a result of the significantly higher water uptake and membrane hydrophilicity as evident from Table 6.6.

Stability in concentrated KOH Solutions

Figure 6.5a shows the membrane conductivity stability during the accelerated testing at 60°C. All tested AEMs had a similar decay timeframe with a loss of at least 90% of conductivity within 30 days using the accelerated testing schedule. Figure 6.5b compares the degradation of AEMs at 60°C and room temperature and shows that the conductivity of the membranes does not decrease significantly over this same time frame. The results indicate that the AEMs should demonstrate satisfactory stability for use in room temperature ZABs.

Conclusions

Anion exchange membranes with polystyrene (PS) and poly(phenylene oxide) (PPO) backbones were evaluated for used in zinc air batteries. For PS membranes the effect of crosslinking agent structure, casting solvent, molecular weight, and inclusion of a separate ammonium group on membrane conductivity, stability, base and water uptake was studied. For PPO membranes the effect of cation structure on these parameters was studied. For the PPO membranes in hydroxide behaved similar to PEMs in acidic media. It was found that the crosslinked nature of the PS membranes allowed them to imbibe more solution, showing higher conductivities in more concentrated hydroxide solutions, which is preferable for use in zinc-air batteries. However, the degradation during the accelerated testing indicated both the PS and PPO membranes may not be feasible for long term use.

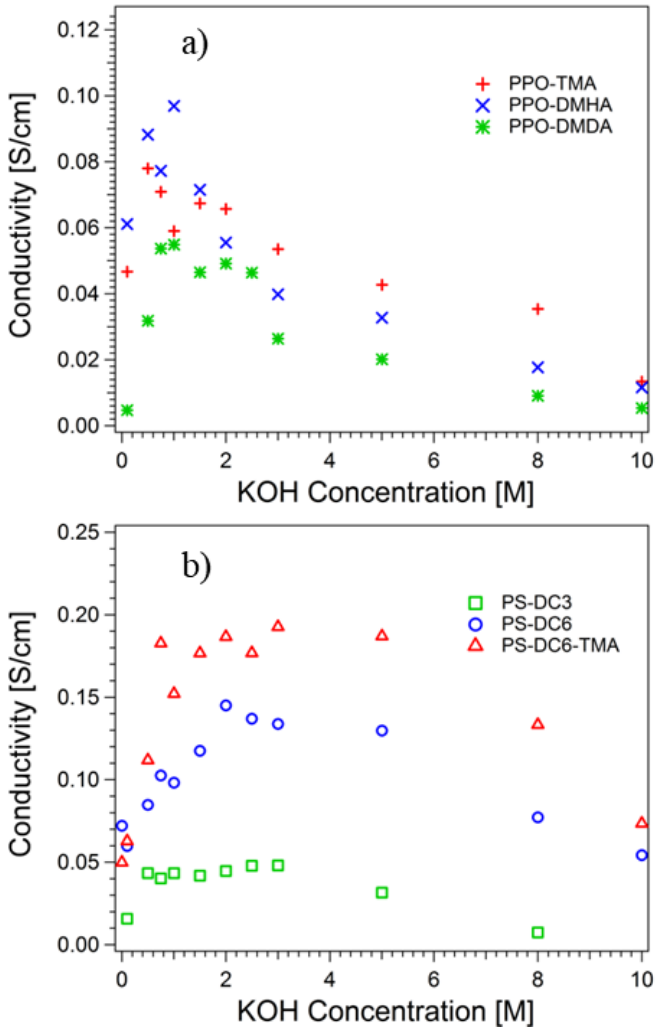

Figure 6.4: Conductivity of (a) PPO and (b) PS based AEMs in KOH solutions

Table 6.6: conductivity and water uptake of Polystyrene and poly(phenylene oxide) based AEMs for ZABs

Membrane	Conductivity [mS/cm]	Water Uptake [%]
PS-DC3	7.5	67
PS-DC6	77.2	186
PS-DC6-TMA	133.2	596
PPO-TMA	15.8	28
PPO-DMHA	4.7	19
PPO-DMDA	4.1	N/A

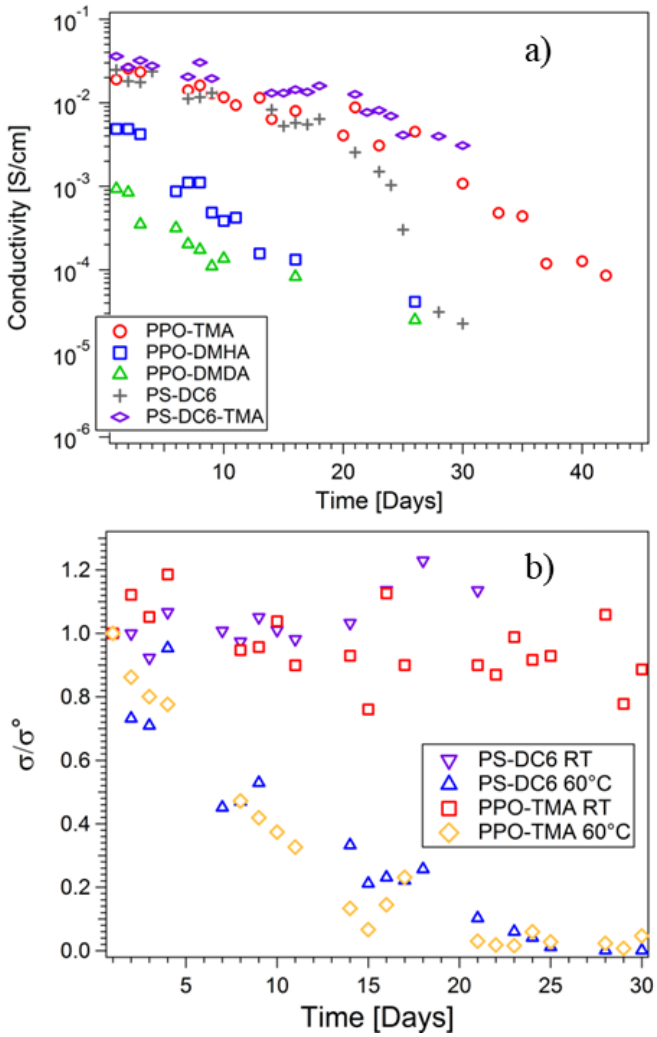

Figure 6.5: conductivity stability in AEMs for ZABs a) stability and 60°C and b) comparison of degradation at 60°C and room temp

CLAMs for Zinc Batteries

Introduction

Studying and comparing the PS and PPO based AEMs showed that the crosslinked structure and the high hydrophilicity of the PS based membranes allowed them greater solution uptakes and conductivities in more concentrated hydroxide solutions. As was observed earlier the hydration history of the hydrophilic PPO based membranes had a dramatic effect on solution uptake and conductivity. This indicates that the most important parameters for membranes for ZABs may be the ability to imbibe large amounts of solution while maintaining mechanical stability. In this regard the importance of the organic cations is to increase membrane hydrophilicity rather than to facilitate conduction as with membranes for AEMFCs. Therefore similar results could be expected with the inclusion of other hydrophilic groups which are also more stable than the quaternary ammoniums such as ethers, esters, or ketones.

During the synthesis of PPO based anion exchange membranes for zinc air batteries using an imidazole as the quaternizing amine it was found that the polymer solution underwent an irreversible gelling process; the process was too quick to be caused by crosslinking or an amination reaction. The process was repeated with diisopropylethylamine (DIEA) in place of the imidazole. DIEA is a tertiary amine shielded by bulky carbon groups and therefore cannot undergo a quaternization reaction; however, it is a good base. In this case the gelation was also observed which indicates the gelation arises from the polymer becoming insoluble in the presence of a base.

By controlling parameters such as the initial polymer concentration and amount of base added it was possible to delay the gelation until after the solution had been cast. After briefly heating, the product was a thick (~0.5mm) film. The reaction solvent was replaced with hydroxide solution. These hydroxide saturated membranes were termed Conductive Loaded Anion Membranes (CLAMs).

Experimental

The base and water uptake, conductivity, and stability experiments followed the procedure previously outlined.

Results and Discussion

The CLAMs had significantly higher water and hydroxide uptakes in concentrated base than conventional AEMs studied previously Figure 6.6. The conductivity was also found to be

substantially higher and much more stable as shown in Figure 6.7. However, if the membranes ever dried completely, it was not possible to regain the high uptakes even if soaked in NMP.

As a result of the extraordinary uptakes the CLAMs had peak conductivities close to 5M; this is significantly closer to the peak conductivity of potassium hydroxide which is between 6 and 7M. The CLAMs demonstrated better stabilities at elevated temperature than the traditional AEMs, presumably because of the much higher water content in CLAMs than AEMs.

The use of CLAMS in ZABs provided much higher conductivity and a large reservoir of KOH compared to conventional AEMs, which required the use of an electrolyte reservoir such as KOH soaked filter paper in ZABs. Additionally, because CLAMs do not rely on the inclusion of unstable organic cations, the conductivity and uptake are maintained over significantly longer time frames. Thus, CLAMs are a stable, highly conductive separator solution for use in zinc air batteries.

Conclusions

The novel synthesis route used to create the CLAMs resulted in separator materials with significantly higher solution uptakes compared to standard AEMs. The conductivity of the membrane is close to the bulk conductivity of the hydroxide solution and significantly higher than the AEM. The cell resistance losses are therefore expected to be much lower with the CLAM, which will be especially important if high current densities can be achieved in the ZAB. Furthermore, the absence of cationic structures in the CLAM increases stability, with no change in conductivity over a 60 day period in the accelerated stability test compared to a two orders of magnitude reduction in conductivity for the AEM during the same test. These results indicate the CLAM materials are good candidates for use in Zinc-air and zinc-peroxide batteries.

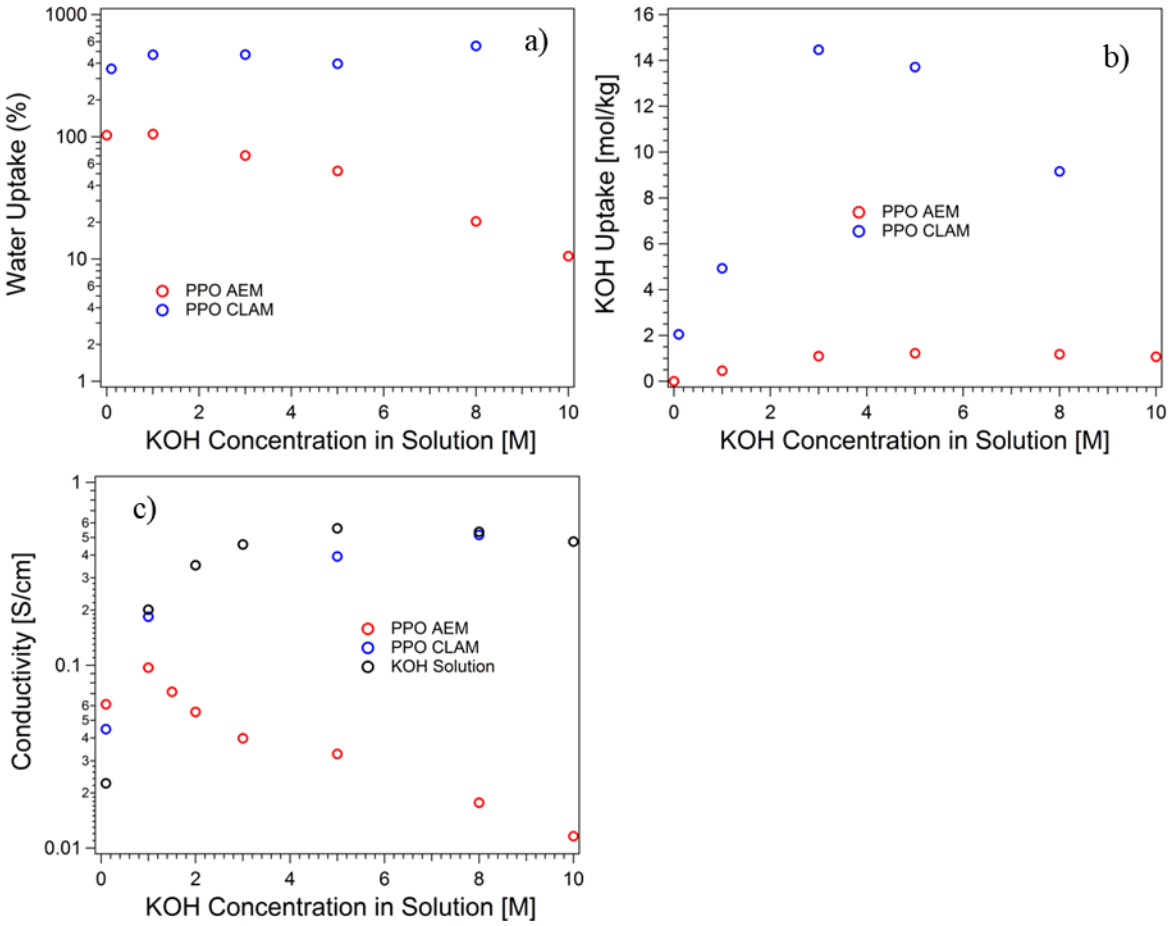

Figure 6.6: a) water uptake, b) KOH uptake, and c) conductivity in traditional PPO based AEM and PPO based CLAM

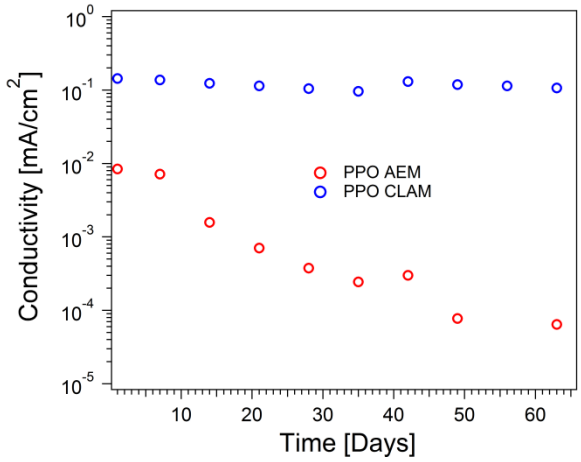

Figure 6.7: Conductivity stability of traditional PPO based AEM and PPO based CLAM in 8 M KOH at 60°C

Hydrogen Peroxide Selectivity in ZPB Membranes

Introduction

As discussed previously, zinc peroxide batteries hold several distinct advantages over zinc air batteries, mainly the reduced disparity between charge and discharge voltages. This is accomplished by using a two electron oxygen reduction to peroxide as opposed to the four electron reduction to peroxide. However, this also adds a new parameter which must be studied for membranes to be used in ZPCs.

Peroxide which crosses the membrane to the zinc side of the membrane is capable of oxidizing the zinc electrode in a self-discharge scheme that reduces the battery capacity. It is therefore vital to study the transport of peroxide through CLAMs. The relevant parameter is the membrane selectivity towards hydrogen peroxide which is a measure of the membrane's hydroxide conductivity normalized by the diffusion coefficient of the hydrogen peroxide in the membrane. In general higher selectivities are desired as they represent higher conductivities for a given amount of crossover.

Experimental

A fuel cell setup was chosen to study the peroxide crossover in AEMs and CLAMs. A diagram of the cell setup is shown in Figure 6.8. First a MEA was produced by spray painting a PtRu/C catalyst layer and a Pt/C catalyst layers to opposite sides of a Tokuyama A201 AEM. The PtRu/C electrode was at a high loading (1 mg/cm2) to act as the reversible hydrogen electrode. This electrode was fed with hydrogen at 200 ml/min. On the other side of the cell a nitrogen purged 1 N hydroxide solution with a known concentration of hydrogen peroxide was continuously pumped. The membrane of interest separated the peroxide reduction electrode and the flow channels. Therefore, the only current which could be drawn was from the reduction of hydrogen peroxide which diffused through the membrane.

The cell was held at a potential within the mass transport limited region and the current response was measured. The diffusion coefficient is related to the current by:

$$I \propto J = D_{H2O2} \frac{\partial C}{\partial x} \qquad [6.5]$$

Where C is the concentration in the bulk electrolyte and x is the thickness of the membrane.

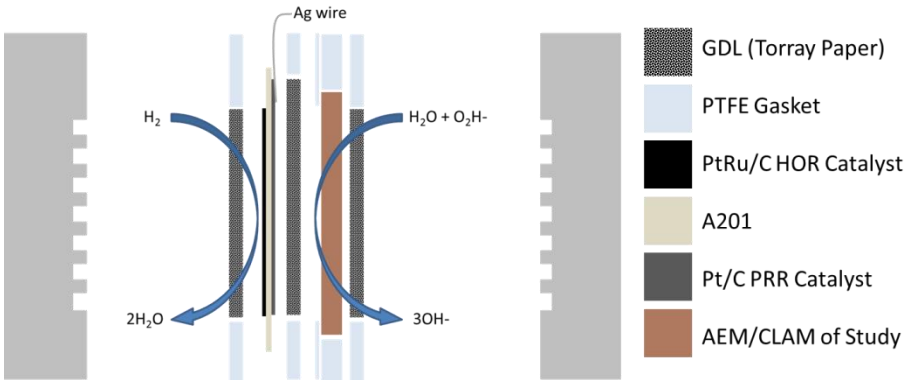

Figure 6.8: Peroxide selectivity cell

However, choosing the membrane with the lowest diffusion coefficient for hydrogen peroxide is not necessarily optimal. Typically, the membrane conductivity and diffusion coefficients are correlated; therefore a membrane with a low diffusion coefficient likely has a low conductivity and will lead to high cell resistances. For this purpose, it is common to study the selectivity of membranes instead. The selectivity is the relation between membrane conductivity and permeability described by:

$$Selectivity = \frac{\sigma}{D_{H2O2}} \quad [6.6]$$

Results and Discussion

A typical polarization curve for the selectivity cell is shown in Figure 6.9a. As would be expected with such low current densities and a high catalyst loading on the hydrogen side of the cell, the contribution to the overpotential by the HOR electrode is negligible. The potential was held within the limiting current density region until a stable current was achieved, as shown in Figure 6.9b. The current is related to the diffusion coefficient and selectivity by Equation 6.5 & 6.6, respectively.

The results for the CLAM membrane and two commercial anion exchange membranes are shown in Table 6.7. The conductivity of the CLAM is ~2.5 times higher than either of the commercial ion exchange membranes. However, the peroxide diffusion coefficient is also higher than the commercial membranes which may be expected from the significantly higher solution uptake in CLAMs. The selectivity of the CLAM membrane is slightly higher than the commercial anion exchange membranes indicating it is a good candidate for use in zinc-peroxide batteries.

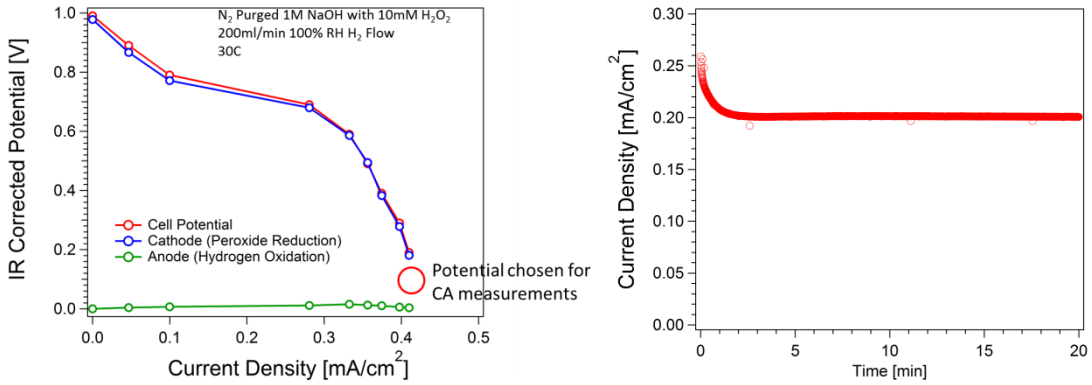

Figure 6.9: a) Selectivity cell polarization curve showing the contributions from the peroxide and hydrogen electrodes. b) Current response to potential hold in the mass transport limited region.

Table 6.7: The measured hydrogen peroxide diffusion coefficients, hydroxide conductivity, and selectivity of selected membranes.

Membrane	Diffusion Coefficient (D_{H2O2}) [cm^2/s]	Conductivity (σ) [S/cm]	Selectivity [$S \cdot s/cm^3$]
Tokuyama A201	5.27×10^{-7}	0.05814	1.10×10^5
Fumatech FAA3-PK-130	3.81×10^{-7}	0.05385	1.41×10^5
CLAM	8.20×10^{-7}	0.143116	1.75×10^5

Conclusions

Continued efforts to combat the effects of climate change and offer consumers longer lasting batteries for electronic devices will require substantial advancements in next generation in energy storage and conversion devices. The work in this thesis detailed the development of novel materials for anion exchange membranes and zinc air batteries as well as advancements in the fundamental understanding of how these materials operate in functional devices.

In chapter 1 a family of platinum group metal-free catalysts was studied for use in anion exchange membrane fuel cells. These materials were synthesized by collaborating researchers. Rotating (ring) disk electrode methods were used to extensively study the catalysts ex-situ. This included measuring the oxygen reduction activity, oxygen reaction order, number of electrons transferred, Tafel slope, and stability. Further experiments were conducted to understand the effect of removing excess metal and to ascertain the possible reaction sites by selectively poisoning the catalyst surface. The most promising catalysts were studied in single cell experiments. This work included studying the fuel cell cathode in isolation to determine the effect of membrane electrode assembly preparation method, and the loading of catalyst and binder on performance. It was found that the cobalt containing catalyst was able to match the performance of the platinum electrode at high current densities at which AEMFCs are expected to operate.

During the course of this work it was observed that some of the catalyst, specifically those containing nickel, demonstrated oxygen evolution activity as well. Chapter 2 focused on the study of these nickel containing platinum group metal-free catalysts for use as bifunctional oxygen catalysts in zinc air batteries. These materials were compared to metal oxide bifunctional catalysts suggested for zinc air batteries in the literature. In addition to the oxygen reduction studies, these catalysts were also tested for oxygen evolution activity and stability in ex-situ testing. The most promising catalyst was incorporated into a ZAB single cell and the performance was compared to the metal oxide catalysts. It was found that the novel catalyst performed best during both charge and discharge. However, there was still a dramatic discrepancy between the charge and discharge potentials.

While these bifunctional catalysts lead to a slight reduction in the disparity of the charge and discharge voltages, the zinc-air battery remained inefficient. Continuing the work of a previous graduate student on a recently discovered reversible two-electron oxygen catalyst for

use in a zinc-peroxide battery was the focus of chapter 3. In this work an effort was made to study the catalyst on a fundamental level to understand the active site. At the outset of this project the catalyst had only been studied on polycrystalline gold electrodes. It was therefore necessary to scale down the catalyst to the nano-scale in order to fabricate a high-surface area electrode for cell testing. The development of a reversible oxygen electrode was further hindered by the necessity of simultaneous liquid and gas flows with meso-porous electrode structures favoring the former and microporous electrodes similar to those used in fuel cells favoring the latter. Despite this difficulty, a 2 phase flow electrode was developed and successfully tested in a functional zinc-peroxide battery. In symmetric cell testing this architecture was shown to be completely stable over a 500 hour testing period. When used in the zinc-peroxide battery, the cell was demonstrated to be significantly more efficient than the previously studied bifunctional four electron oxygen catalysts.

During testing on the platinum group metal-free catalysts in AEMFCs, it was observed that the anode contributed significantly more to the overall cell polarization than the cathode. This was an unexpected result and Chapter 5 focused on determining the origin of the high overpotential in AEMFC anodes. Various suggested causes of the high polarization such as poor catalysis, insufficient hydrogen flow, and catalyst poisoning were ruled out, leaving flooding as the most significant cause of poor anode performance. Attempts were made to increase water removal from the anode catalyst layer by changing the gas diffusion layer material to no avail. Changing the catalyst layer structure, by using a higher boiling point solvent for the ink application process, lead to a dramatic increase in anode performance. However, the gains at the anode lead to equal losses at the cathode from drying out the membrane too much. This study highlighted the importance of better understanding water transport in anion exchange membranes.

Chapter 5 focused on the study of anion exchange membranes for AEMFCs. This study involved the synthesis of anion exchange membranes with different cation structures and the same backbone. This work was conducted to determine the effect of cation structure on water uptake, conductivity, swelling, stability and other relevant parameters. The most promising membrane was prepared with a simple cation separated from the backbone by a long alkyl chain, however this membrane experience high water uptakes and swelling in fully hydrated environments. This could be alleviated by partially crosslinking the membrane in future work.

Following from the revelations in Chapter 4, the electro-osmotic transport of water with the anion in Tokuyama's commercial AEM, A201, was studied. For the first time in the literature, this work was conducted for bicarbonate and hydroxide form membranes. It was found that significantly more water is transported with the hydroxide current than with the proton current in PEMs. This explains why anode flooding is such a difficult issue in testing AEMFCs. It was found that the electro-osmotic transport of water by the bicarbonate ion is much lower than it is with the hydroxide ion.

Chapter 6 focused on the development of a separator material for zinc air and zinc peroxide batteries. Initial work focused on studying standard anion exchange membranes in the concentrated hydroxide solutions. However, these materials generally demonstrated low conductivities, solution uptake, and stability. The development of a novel gel-like membrane material, dubbed CLAMs, proved to be much more promising for these systems. The CLAM materials imbibed large amounts of solution to achieve high conductivities and long term stabilities, while remaining robust enough to prevent dendrite puncturing.

References

1. J. O. Bockris and A. K. M. S. Huq, *Proc. R. Soliety London, Ser. A*, **237**, 277 (1956).

2. N. Watanabe and M. Devanathan, *J. Electrochem. ...*, **111** (1964) http://jes.ecsdl.org/content/111/5/615.short.

3. R. Thacker and J. P. Hoare, *J. Electrochem. Soc.*, **113**, 862–863 (1966).

4. H. S. Wroblowa and G. Razumney, *J. Electroanal. Chem. Interfacial Electrochem.*, **69**, 195–201 (1976) http://www.sciencedirect.com/science/article/pii/S0022072876802501.

5. J. Suntivich et al., *Nat. Chem.*, **3**, 546–550 (2011) http://dx.doi.org/10.1038/nchem.1069.

6. J. Rossmeisl, A. Logadottir, and J. K. Nørskov, *Chem. Phys.*, **319**, 178–184 (2005).

7. H. Dau et al., *ChemCatChem*, **2**, 724–761 (2010).

8. I. E. L. Stephens, A. S. Bondarenko, U. Grønbjerg, J. Rossmeisl, and I. Chorkendorff, *Energy Environ. Sci.*, **5**, 6744 (2012).

9. N. B. Halck, V. Petrykin, P. Krtil, and J. Rossmeisl, *Phys. Chem. Chem. Phys.*, **16**, 13682–13688 (2014) http://www.ncbi.nlm.nih.gov/pubmed/24671166.

10. I. C. Man et al., *ChemCatChem*, **3**, 1159–1165 (2011) http://doi.wiley.com/10.1002/cctc.201000397.

11. J. C. Huang, R. K. Sen, and E. Yeager, *J. Electrochem. Soc.*, **126**, 786–792 (1979) http://jes.ecsdl.org/cgi/doi/10.1149/1.2129139.

12. D. B. Sepa, M. V. Vojnovic, and a. Damjanovic, *Electrochim. Acta*, **26**, 781–793 (1981).

13. a. Holewinski and S. Linic, *J. Electrochem. Soc.*, **159**, H864–H870 (2012).

14. D. Sepa, M. Vojnovic, and A. Damjanovic, *Electrochim. Acta*, **25**, 1491–1496 (1980).

15. J. K. Nørskov et al., *J. Phys. Chem. B*, **108**, 17886–17892 (2004).

16. V. Neburchilov, H. Wang, J. J. Martin, and W. Qu, *J. Power Sources*, **195**, 1271–1291 (2010).

17. D. Sepa, M. Vojnovi, and A. Damjanovict, *Electrochim. Acta*, **15**, 1355–1366 (1970).

18. S. Mukerjee, *J. Appl. Electrochem.*, **20**, 537–548 (1990).

19. G. Couturier, D. W. Kirk, P. J. Hyde, and S. Srinivasan, *Electrochim. Acta*, **32**, 995–1005 (1987).

20. B. C. Beard and P. N. Ross, *J. Electrochem. Soc.*, **137**, 3368 (1990) http://jes.ecsdl.org/content/137/11/3368.short\nhttp://jes.ecsdl.org/cgi/doi/10.1149/1.2086223.

21. R. R. Adzic et al., *Top. Catal.*, **46**, 249–262 (2007).

22. V. R. Stamenkovic, B. S. Mun, K. J. J. Mayrhofer, P. N. Ross, and N. M. Markovic, *J. Am.*

Chem. Soc., **128**, 8813–8819 (2006).

23. H.-K. Lee, J.-P. Shim, M.-J. Shim, S.-W. Kim, and J.-S. Lee, *Mater. Chem. Phys.*, **45**, 238–242 (1996) http://linkinghub.elsevier.com/retrieve/pii/0254058495017380.

24. L. Ferna, D. a Walsh, and A. J. Bard, *J. Am. Chem. Soc.*, **127**, 357–365 (2005).

25. F. H. B. Lima, J. F. R. de Castro, and E. a. Ticianelli, *J. Power Sources*, **161**, 806–812 (2006).

26. Q. Yi and L. Song, *Electroanalysis*, **24**, 1655–1663 (2012) http://doi.wiley.com/10.1002/elan.201200154.

27. R. Jasinski, *Nature*, **201**, 1212–1213 (1964).

28. J. Masta, K. I. Ozoemena, W. Schuhmann, and J. H. Zagal, in *Electrocatalysis in Fuel Cells A Non- and Low- Platinum Approach*,, vol. 9, p. 27–42 (2013) http://www.scopus.com/inward/record.url?eid=2-s2.0-84882946741&partnerID=tZOtx3y1.

29. J. H. Zagal, M. Gulppi, M. Isaacs, G. Cárdenas-Jirón, and M. J.́s Aguirre, *Electrochim. Acta*, **44**, 1349–1357 (1998) http://www.sciencedirect.com/science/article/pii/S0013468698002576.

30. J.-P. Randin, *Electrochim. Acta*, **19**, 83–85 (1974).

31. J. H. Zagal, M. J. Aguirre, L. Basaez, and J. Pavez, in *Proceedings of the Symposium on Oxygen Electrochemistry*,, p. 89–100 (1996).

32. P. Machata et al., *Organometallics*, **33**, 4846–4859 (2014) http://pubs.acs.org/doi/abs/10.1021/om5000584.

33. S. Zecevic, B. Simic-Glavaski, E. Yeager, a. B. P. Lever, and P. C. Minor, *J. Electroanal. Chem.*, **196**, 339–358 (1985).

34. J. Zagal, M. Páez, a. a. Tanaka, J. R. dos Santos, and C. a. Linkous, *J. Electroanal. Chem.*, **339**, 13–30 (1992).

35. G. Wang, N. Ramesh, A. Hsu, D. Chu, and R. Chen, *Mol. Simul.*, **34**, 1051–1056 (2008).

36. R. Chen, H. Li, D. Chu, and G. Wang, *J. Phys. Chem. C*, **113**, 20689–20697 (2009).

37. J. Zagal, P. Bindra, and E. Yeager, *J. Electrochem. Soc.*, **127**, 1506–1517 (1980) <Go to ISI>://WOS:A1980JZ46100017.

38. J. Dodelet, in *Electrocatalysis in Fuel Cells A Non- and Low- Platinum Approach*,, p. 271–338 (2013) http://www.scopus.com/inward/record.url?eid=2-s2.0-84882946741&partnerID=tZOtx3y1.

39. S. Gupta, D. Tryk, I. Bae, W. Aldred, and E. Yeager, *J. Appl. Electrochem.*, **19**, 19–27 (1989).

40. W. Li, J. Wu, D. Higgins, J. Choi, and Z. Chen, *ACS Catal.*, **2**, 2761–2768 (2012)

http://pubs.acs.org/doi/abs/10.1021/cs300579b.

41. U. I. Kramm et al., *Phys. Chem. Chem. Phys.*, **14**, 11673 (2012) http://xlink.rsc.org/?DOI=c2cp41957b.

42. P. Song, Y. Zhang, J. Pan, L. Zhuang, and W. Xu, *Chem. Commun.*, 1–4 (2015) http://dx.doi.org/10.1039/C4CC07677J.

43. A. Zitolo et al., *Nat. Mater.*, **14**, 937–942 (2015) http://www.nature.com/doifinder/10.1038/nmat4367.

44. U. Tylus et al., *J. Phys. Chem. C. Nanomater. Interfaces*, **118**, 8999–9008 (2014) http://dx.doi.org/10.1021/jp500781v.

45. L. Elbaz, G. Wu, and P. Zelany, in *Electrocatalysis in Fuel Cells A Non- and Low- Platinum Approach*,, vol. 9, p. 213–246 (2013) http://www.scopus.com/inward/record.url?eid=2-s2.0-84882946741&partnerID=tZOtx3y1.

46. a. L. Bouwkamp-Wijnoltz et al., *J. Phys. Chem. B*, **106**, 12993–13001 (2002).

47. J. Chlistunoff, *J. Phys. Chem. C*, null–null (2011) http://dx.doi.org/10.1021/jp108350t.

48. S. Gupta, C. Fierro, and E. Yeager, *... Chem. Interfacial Electrochem.*, **306**, 239–250 (1991) http://www.sciencedirect.com/science/article/pii/002207289185233F.

49. R. Zhou and S. Z. Qiao, *Chem. Commun. (Camb).*, **51**, 7516–9 (2015) http://www.ncbi.nlm.nih.gov/pubmed/25838261.

50. A. Serov, U. Tylus, K. Artyushkova, S. Mukerjee, and P. Atanassov, *Appl. Catal. B Environ.*, **150-151**, 179–186 (2014) http://dx.doi.org/10.1016/j.apcatb.2013.12.009.

51. X.-H. Yan and B.-Q. Xu, *J. Mater. Chem. A*, 8617–8622 (2014) http://xlink.rsc.org/?DOI=c3ta15300b.

52. F. Jaouen and J.-P. Dodelet, *J. Phys. Chem. C F. Full J. TitleJournal Phys. Chem. C*, **113**, 15433–15443 (2009).

53. G. a. Goenaga et al., *ECS Electrochem. Lett.*, **3**, F68–F71 (2014) http://eel.ecsdl.org/cgi/doi/10.1149/2.0071411eel.

54. S. Gabriel A. Goenaga, Ashesh Belapure, Congling Zhang, Alex Papandrew and F. and T. A. Z. Jr., **41**, 1193–1205 (2011).

55. S. Chao and M. Geng, *Int. J. Hydrogen Energy*, 2–11 (2016).

56. E. A. González, M. Gulppi, M. A. Páez, and J. H. Zagal, *Diam. Relat. Mater.*, **64**, 119–129 (2016).

57. D. Malko, T. Lopes, E. Symianakis, and A. R. Kucernak, *J. Mater. Chem. A*, **4**, 142–152 (2016).

58. N. M. Marković, R. R. Adžić, B. D. Cahan, and E. B. Yeager, *J. Electroanal. Chem.*, **377**, 249–259 (1994).

59. X. Li, B. N. Popov, T. Kawahara, and H. Yanagi, *J. Power Sources*, **196**, 1717–1722 (2011) http://dx.doi.org/10.1016/j.jpowsour.2010.10.018.

60. D. Zhao et al., *Adv. Mater.*, **26**, 1093–1097 (2014).

61. X.-H. Yan and B.-Q. Xu, *J. Mater. Chem. A*, **2**, 8617–8622 (2014).

62. H. Yanagi and K. Fukuta, *ECS Trans.*, **16**, 257–262 (2008) http://ecst.ecsdl.org/cgi/doi/10.1149/1.2981860.

63. I. Kruusenberg, L. Matisen, Q. Shah, a. M. Kannan, and K. Tammeveski, *Int. J. Hydrogen Energy*, **37**, 4406–4412 (2012) http://dx.doi.org/10.1016/j.ijhydene.2011.11.143.

64. W.-J. Zhang, *J. Power Sources*, **196**, 13–24 (2011) http://www.sciencedirect.com/science/article/pii/S0378775310011699.

65. Y. X. Yin, S. Xin, Y. G. Guo, and L. J. Wan, *Angew. Chemie - Int. Ed.*, **52**, 13186–13200 (2013).

66. M. a. Rahman, X. Wang, and C. Wen, *J. Electrochem. Soc.*, **160**, A1759–A1771 (2013) http://jes.ecsdl.org/cgi/doi/10.1149/2.062310jes.

67. B. D. Mccloskey, J. M. Garcia, and A. C. Luntz, 2–7 (2014).

68. S. Whittingham, *Meet. Abstr.* , **MA2012-02** , 1099 (2012) http://ma.ecsdl.org/content/MA2012-02/11/1099.abstract.

69. G. McLean, *Int. J. Hydrogen Energy*, **27**, 507–526 (2002).

70. G. Toussaint, P. Stevens, L. Akrour, R. Rouget, and F. Fourgeot, *ECS Trans.*, **28**, 25–34 (2010).

71. P. Pei, K. Wang, and Z. Ma, *Appl. Energy*, **128**, 315–324 (2014).

72. F. H. B. Lima, M. L. Calegaro, and E. a. Ticianelli, *Electrochim. Acta*, **52**, 3732–3738 (2007).

73. Y. L. Cao, H. X. Yang, X. P. Ai, and L. F. Xiao, *J. Electroanal. Chem.*, **557**, 127–134 (2003) http://linkinghub.elsevier.com/retrieve/pii/S0022072803003553.

74. Y. Chabre and J. Pannetier, *Prog. Solid State Chem.*, **23**, 1–130 (1995).

75. J. C. Hunter and A. Kozawa, in *Standard Potentials in Aqueous Solutions*, A. J. Bard, R. Parsons, and J. Jordan, Editors, p. 429–452 (1985).

76. F. L. Tye, (1975).

77. K. a Stoerzinger, M. Risch, B. Han, and Y. Shao-horn, (2015).

78. T. Hyodo, M. Hayashi, N. Miura, and N. Yamazoe, *J. Electrochem. Soc.*, **143**, L266 (1996).

79. F. Cheng et al., *Nat. Chem.*, **3**, 79–84 (2011) http://dx.doi.org/10.1038/nchem.931.

80. W. T. Hong et al., *J. Phys. Chem. Lett.*, **4**, 2493–2499 (2013).

81. W. Zhou and J. Sunarso, *J. Phys. Chem. Lett.*, **4**, 2982–2988 (2013).

82. J. Suntivich, K. J. May, H. A. Gasteiger, J. B. Goodenough, and Y. Shoa-Horn, *Science*, **334**, 1383 (2011).

83. W. G. Hardin et al., *J. Phys. Chem. Lett.*, **4**, 1254–1259 (2013).

84. W. Lee, J. W. Han, Y. Chen, Z. Cai, and B. Yildiz, *J. Am. Chem. Soc.*, **135**, 7909–7925 (2013).

85. E. Fabbri, A. Habereder, K. Waltar, R. Kötz, and T. J. Schmidt, *Catal. Sci. Technol.*, **4**, 3800–3821 (2014) http://xlink.rsc.org/?DOI=C4CY00669K.

86. M. E. G. Lyons and M. P. Brandon, *J. Electroanal. Chem.*, **641**, 119–130 (2010) http://linkinghub.elsevier.com/retrieve/pii/S1572665709004500.

87. O. Diaz-Morales, I. Ledezma-Yanez, M. T. M. Koper, and F. Calle-Vallejo, *ACS Catal.*, **5**, 5380–5387 (2015) http://pubs.acs.org/doi/10.1021/acscatal.5b01638.

88. Y.-L. Lee, M. J. Gadre, Y. Shao-Horn, and D. Morgan, *Phys. Chem. Chem. Phys.*, **17**, 21643–21663 (2015) http://xlink.rsc.org/?DOI=C5CP02834E.

89. J. Rossmeisl, K. Dimitrievski, P. Siegbahn, and J. Norskov, *J. Phys. Chem. C*, **111**, 18821–18823 (2007).

90. C. A. Reiser et al., *Electrochem. Solid-State Lett.*, **8**, A273 (2005) http://esl.ecsdl.org/cgi/doi/10.1149/1.1896466.

91. J. Kim, J. Lee, and Y. Tak, *J. Power Sources*, **192**, 674–678 (2009) http://www.sciencedirect.com/science/article/pii/S0378775309005473.

92. N. Staud, H. Sokol, and P. N. Ross, *J. Electrochem. Soc.*, **136**, 3570 (1989).

93. P. N. Ross and M. Sattler, *J. Electrochem. Soc.*, **135**, 1465 (1988).

94. P. N. Ross and H. Sokol, *J. Electrochem. Soc.*, **131**, 1742 (1984).

95. N. Staud and P. N. Ross, *J. Electrochem. Soc.*, **133**, 1079 (1986).

96. T. Mugadza and T. Nyokong, *Talanta*, **81**, 1373–1379 (2010) http://dx.doi.org/10.1016/j.talanta.2010.02.037.

97. X. G. Zhang, *Corrosion and Electrochemsitry of Zinc*, 1st Editio., Springer Science + Business Media, New York, (1996).

98. R. W. Powers, *J. Electrochem. Soc.*, **118**, 685 (1971).

99. R. W. Powers and M. W. Breiter, *J. Electrochem. Soc.*, **116**, 719 (1969).

100. Y. Ding, Y. J. Kim, and J. Erlebacher, *Adv. Mater.*, **16**, 1897–1900 (2004).

101. W. Sheng, H. A. Gasteiger, and Y. Shao-horn, *J. Electrochem. Soc.*, **157**, 1529–1536 (2010).

102. W. Sheng et al., *Energy Environ. Sci.*, **7**, 1719 (2014) http://xlink.rsc.org/?DOI=c3ee43899f.

103. P. J. Rheinlander, J. Herranz, J. Durst, and H. a. Gasteiger, *J. Electrochem. Soc.*, **161**, F1448–F1457 (2014) http://jes.ecsdl.org/cgi/doi/10.1149/2.0501414jes.

104. J. Durst et al., *Energy Environ. Sci.*, **7**, 2255–2260 (2014) <Go to ISI>://WOS:000337977600016\nhttp://pubs.rsc.org/en/content/articlepdf/2014/ee/c4ee00440j.

105. M. Bates, thesis, Northeastern University (2015).

106. N. Ramaswamy et al., *Nano Energy*, **41**, 765–771 (2017) http://dx.doi.org/10.1016/j.nanoen.2017.07.053.

107. S. St. John, R. W. Atkinson, R. R. Unocic, T. a. Zawodzinski, Jr., and A. B. Papandrew, *J. Phys. Chem. C*, **119**, 13481–13487 (2015) http://pubs.acs.org/doi/abs/10.1021/acs.jpcc.5b03284.

108. S. St. John et al., *ACS Catal.*, **5**, 7015–7023 (2015) http://pubs.acs.org/doi/10.1021/acscatal.5b01432.

109. A. L. Ong, D. K. Whelligan, M. L. Fox, and J. R. Varcoe, *Phys. Chem. Chem. Phys.*, **15**, 18992–9000 (2013) http://www.ncbi.nlm.nih.gov/pubmed/24100347.

110. S.-D. Yim et al., *J. Electrochem. Soc.*, **162**, F499–F506 (2015) http://jes.ecsdl.org/cgi/doi/10.1149/2.0151506jes.

111. R. Fernández, P. Ferreira-Aparicio, and L. Daza, *J. Power Sources*, **151**, 18–24 (2005).

112. T. H. Yang, Y. G. Yoon, G. G. Park, W. Y. Lee, and C. S. Kim, *J. Power Sources*, **127**, 230–233 (2004).

113. D. C. Huang et al., *Int. J. Electrochem. Sci.*, **6**, 2551–2565 (2011).

114. G. Merle, M. Wessling, and K. Nijmeijer, *J. Memb. Sci.*, **377**, 1–35 (2011) <Go to ISI>://000292580000001\nhttp://www.sciencedirect.com/science/article/pii/S037673881100308 5.

115. C. G. Arges, L. Wang, J. Parrondo, and V. Ramani, *J. Electrochem. Soc.*, **160**, F1258–F1274 (2013) http://jes.ecsdl.org/cgi/doi/10.1149/2.049311jes.

116. N. Li, Y. Leng, M. a Hickner, and C.-Y. Wang, *J. Am. Chem. Soc.*, **135**, 10124–33 (2013) http://www.ncbi.nlm.nih.gov/pubmed/23721192.

117. J. Ran et al., *J. Memb. Sci.*, **415-416**, 242–249 (2012)

http://linkinghub.elsevier.com/retrieve/pii/S0376738812003705.

118. X. Lin et al., *J. Power Sources*, **217**, 373–380 (2012) http://linkinghub.elsevier.com/retrieve/pii/S0378775312009317.

119. J. R. Varcoe et al., *Energy Environ. Sci.*, **7**, 3135–3191 (2014) http://xlink.rsc.org/?DOI=C4EE01303D.

120. C. G. Arges and V. Ramani, *J. Electrochem. Soc.*, **160**, F1006–F1021 (2013) http://jes.ecsdl.org/cgi/doi/10.1149/2.056309jes.

121. X. Li, Y. Yu, Q. Liu, and Y. Meng, *J. Memb. Sci.*, **436**, 202–212 (2013) http://dx.doi.org/10.1016/j.memsci.2013.02.041.

122. J. Pan, C. Chen, L. Zhuang, and J. Lu, *Acc Chem Res*, **45**, 473–481 (2012) http://www.ncbi.nlm.nih.gov/pubmed/22075175.

123. J. Pan et al., *Energy Environ. Sci.*, **7**, 354 (2014) http://xlink.rsc.org/?DOI=c3ee43275k.

124. J. Pan, Y. Li, L. Zhuang, and J. Lu, *Chem. Commun.*, **46**, 8597 (2010) http://xlink.rsc.org/?DOI=c0cc03618h.

125. J. Pan et al., *Adv. Funct. Mater.*, **20**, 312–319 (2010) http://doi.wiley.com/10.1002/adfm.200901314.

126. O. I. Deavin et al., *Energy Environ. Sci.*, **5**, 8584 (2012) http://xlink.rsc.org/?DOI=c2ee22466f.

127. B. Lin et al., *Chem. Mater.*, **25**, 1858–1867 (2013) http://dx.doi.org/10.1021/cm400468u\nhttp://pubs.acs.org/doi/pdfplus/10.1021/cm400468u.

128. O. M. M. Page et al., *RSC Adv.*, **3**, 579 (2013) http://xlink.rsc.org/?DOI=c2ra22331g.

129. B. Qiu, B. Lin, L. Qiu, and F. Yan, *J. Mater. Chem.*, **22**, 1040–1045 (2012) http://xlink.rsc.org/?DOI=C1JM14331J.

130. R. L. Weber et al., *J. Polym. Sci. Part B Polym. Phys.*, **49**, 1287–1296 (2011).

131. G. Couture, A. Alaaeddine, F. Boschet, and B. Ameduri, *Prog. Polym. Sci.*, **36**, 1521–1557 (2011) http://dx.doi.org/10.1016/j.progpolymsci.2011.04.004.

132. W. Lu et al., *Int. J. Hydrogen Energy*, **38**, 9285–9296 (2013) http://www.sciencedirect.com/science/article/pii/S0360319913012664.

133. T. Sata, Y. Yamane, and K. Matsusaki, *J. Polym. Sci. Part A Polym. Chem.*, **36**, 49–58 (1998) http://onlinelibrary.wiley.com/doi/10.1002/(SICI)1099-0518(19980115)36:1<49::AID-POLA8>3.0.CO;2-X/pdf.

134. L. Ye et al., *Solid State Ionics*, **240**, 1–9 (2013).

135. X. Wang et al., *Int. J. Hydrogen Energy*, **36**, 10022–10026 (2011)

http://dx.doi.org/10.1016/j.ijhydene.2011.05.054.

136. A. D. Mohanty and C. Bae, *J. Mater. Chem. A*, **2**, 17314–17320 (2014) http://xlink.rsc.org/?DOI=C4TA03300K.

137. Y. S. Kim, in, p. 1–20, 2012 U.S. DOE Hydrogen and Fuel Cells Program and Vehicle Technologies Program Annual Merit Review and Peer Evaluation Meeting May 14-18, 2012, Washington, D.C (2012).

138. T. A. Zawodzinski et al., **140** (1993).

139. Z. Tang et al.,.

140. T. A. Zawodzinski et al., *J.*, **140**, 1981–1985 (1993).

141. E. Gileadi, S. D. Argade, and J. O. M. Bockris, *J. Phys. Chem.*, **70**, 2044–2046 (1966).

142. T. J. Omasta et al., *J. Power Sources*, **375**, 205–213 (2018) https://doi.org/10.1016/j.jpowsour.2017.05.006.

143. Y. Garsany, O. A. Baturina, K. E. Swider-Lyons, and S. S. Kocha, *Anal. Chem.*, **82**, 6321–6328 (2010).

144. Z. Peng, A. Morin, P. Huguet, P. Schott, and J. Pauchet, *J. Phys. Chem. B*, **115**, 12835–12844 (2011).

145. L. C. Jacobson, X. Ren, and V. Molinero, *J. Phys. Chem. C*, **118**, 2093–2103 (2014).

146. X. Wang, J. P. Mcclure, and P. S. Fedkiw, *Electrochim. Acta*, **79**, 126–132 (2012) http://dx.doi.org/10.1016/j.electacta.2012.06.098.

147. T. F. Fuller and J. Newman, *J. Electrochem. Soc.*, **139**, 1332–1337 (1992).

148. J. Peng, A. L. Roy, S. G. Greenbaum, and T. A. Zawodzinski, *J. Power Sources*, **380**, 64–75 (2018) https://doi.org/10.1016/j.jpowsour.2018.01.071.

149. T. A. Zawodzinski, M. Neeman, L. O. Sillerud, and S. Gottesfeld, *J. Phys. Chem.*, **95**, 6040–6044 (1991).

150. M. Unlu, J. Zhou, and P. A. Kohl, *Electrochem. Solid-State Lett.*, **12**, B27 (2009) http://esl.ecsdl.org/cgi/doi/10.1149/1.3058999.

151. S. Huo, H. Deng, Y. Chang, and K. Jiao, *Int. J. Hydrogen Energy*, **37**, 18389–18402 (2012) http://dx.doi.org/10.1016/j.ijhydene.2012.09.074.

152. H. Deng et al., *Renew. Energy*, **91**, 166–177 (2016) http://dx.doi.org/10.1016/j.renene.2016.01.054.

153. Y. S. Li, T. S. Zhao, and W. W. Yang, *Int. J. Hydrogen Energy*, **35**, 5656–5665 (2010) http://dx.doi.org/10.1016/j.ijhydene.2010.03.026.

Vita

Asa Roy grew up in a small Vermont town. He enrolled in Clemson University in Clemson, SC where, in 2012, he received a Bachelor of Science degree in Materials Science with a concentration on soft materials, i.e. polymers. While an undergraduate student he participated in several research projects under Dr. Luiz Jacobsohn and Dr. Igor Luzinov. He also participated in a National Science Foundation Research Experience for Undergraduates at the University of Akron under Dr. Robert Weiss. Later in 2012 Asa joined the Bredesen Center for Interdisciplinary Research and Education at the University of Tennessee, Knoxville as a graduate student. He worked in the research of Dr. Thomas Zawodzinski Jr.